Department of Precision and Microsystems Engineering & Materials Science and Engineering

Planar Flow Casting and Microstructure of Aluminium Silicon Alloy

Roald Lingmont

Report no : 2023.085
Coach : Dr.ir. R.A.J. van Ostayen & Dr.ir. S.E. Offerman
Professor : Dr.ir. R.A.J. van Ostayen & Dr.ir. S.E. Offerman
Specialisation : Mechatronic System Design & Microstructures
Type of report : Master Thesis
Date : 16 Oktober 2023

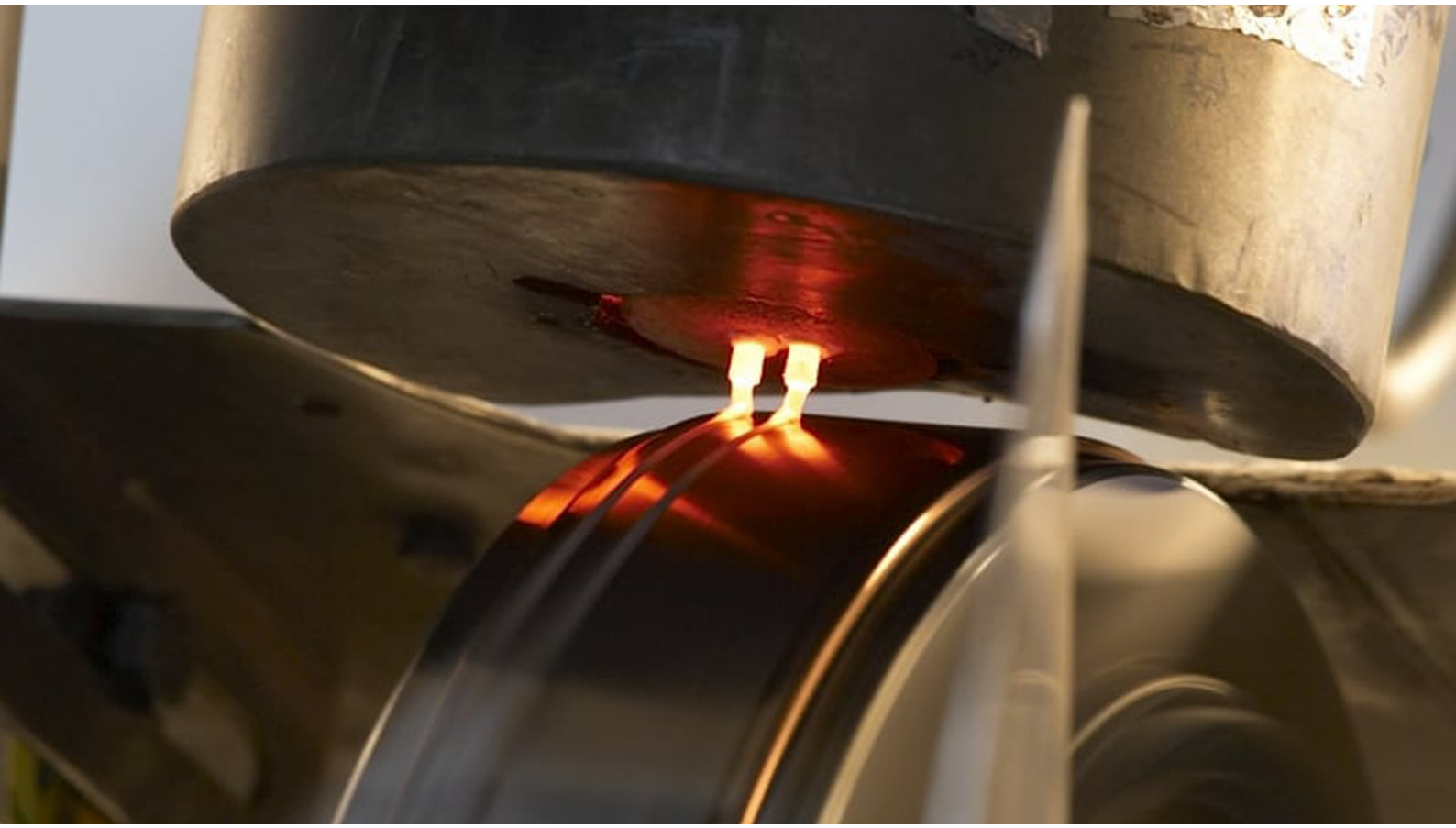

Planar Flow Casting and Microstructure of Aluminium Silicon Alloy

Thesis report

by

Roald Lingmont

to obtain the degree of Master of Science
at the Delft University of Technology
to be defended publicly on October 16, 2023 at 13:00

Thesis committee:

Chair:	Dr.ir. R.A.J. van Ostayen
Supervisors:	Dr.ir. R.A.J. van Ostayen
	Dr.ir. S.E. Offerman
External examiner:	Dr. S. Kumar
	Ir. J.P. Kappelhof
	Ir. A. van der Vries
Place:	Faculty of Mechanical, Maritime and Materials Engineering, Delft
Project Duration:	September, 2021 - October, 2023
Student number:	4473248

An electronic version of this thesis is available at `http://repository.tudelft.nl/`.

Faculty of Mechanical, Maritime and Materials Engineering · Delft University of Technology

Abstract

In order to scale the planar flow casting (PFC) process to industrial levels a Python model is created. The model which is based on a combination of empirical and theoretical equations, is used to explore the limits of the process. The model is independently verified with a Comsol simulation, which is extended with solidification and heat transfer physics. The model is then used as a bases for a system and control simulation of the complete planar flow casting system. Extra elements are added, such as thermal expansion, out of roundness of the wheel, crucible and actuator mechanics, and sensor behaviour. The controllability of the system using a PID controller is presented. With this knowledge, the design requirements for the adjustment of the existing PFC machine were defined, qualitatively as well as quantitatively, for the nozzle, pressure system and gap sensor. Following this, the microstructure of the material produced by the free flow casting (FFC) process is analysed. The microstructure is measured using XRD, SEM and EDS techniques. These measurements are then compared with a model based on the Scheil equation and a kinetic phase diagram, developed for the aluminium silicon alloy. The microstructure found consisted of primary silicon particles in which a significant amount of aluminium was dissolved, as predicted by the material model. The silicon particles are dispersed within an aluminium silicon eutectic matrix with rounded needle like features. The silicon particle size is in the order of 5 µm, whilst the feature size in the eutectic is in the order of 100 nm.

Contents

List of Figures iv

List of Tables vi

1 Introduction 1

I Preliminary Analysis 3

II Process modelling 53

2 Planar flow casting model 54
2.1 Operating window method . . . 54
2.2 Model . . . 56
2.3 Operating window results . . . 57
2.4 Discussion . . . 59

3 Comsol Simulation 60
3.1 Methods . . . 61
3.2 Results . . . 64
3.3 Discussion . . . 68

4 System and Control 70
4.1 The system . . . 71
4.2 The plant . . . 71
4.3 Sampling and noise . . . 72
4.4 Actuator and controller . . . 72
4.5 Model . . . 73
4.6 Results . . . 76
4.7 Discussion . . . 77

5 Design Requirements 78
5.1 Sensor . . . 78
5.2 Pressure system . . . 79
5.3 Nozzle . . . 80
5.4 Discussion . . . 80

III Material Science 81

6 Material Analysis 82
6.1 Introduction . . . 82
6.2 Sample preparation . . . 82
6.3 SEM . . . 83
6.4 EDS . . . 85
6.5 XRD . . . 87
6.6 Discussion . . . 88

7 Material modelling 89
7.1 Kinetic phase diagram . . . 90
7.2 Scheil equation . . . 91
7.3 Grain size . . . 94

7.4 Area composition calculation 95
7.5 Discussion 96

IV Closure **97**

8 Conclusion **98**

References **100**

A PFC model Python code **101**

B System and control model Python code **104**

C Material model Python code **111**

List of Figures

1.1 Process overview and resulting ribbon. The schematics and micrograph are adapted from Byrne et al. [1] . . . 2

2.1 Operating range under constant pressure. The green gradient represents the resulting ribbon thickness. The red area causes a blowout on the backside of the gap. The blue area will not fully solidify the ribbon. In the black area the pressure is not sufficient to allow for flow through the nozzle and/or gap. . . . 57
2.2 Operating range for a constant speed. The green gradient represents the resulting ribbon thickness. The red area causes a blowout on the backside of the gap. The blue area will not fully solidify the ribbon. In the black area the pressure is not sufficient to allow for flow through the nozzle and/or gap. . . . 58
2.3 Operating range for a constant gap. The green gradient represents the resulting ribbon thickness. The red area causes a blowout on the backside of the gap. The blue area will not fully solidify the ribbon. In the black area the pressure is not sufficient to allow for flow through the nozzle and/or gap. . . . 59

3.1 Results from a Comsol simulation of the PFC process. Temperature is represented with a color gradient from dark red to yellow. The surrounding air is dark grey. The solidification front is presented as a black line starting at the first contact point with the wheel in the lower left side of the puddle. . . . 60
3.2 Comsol setup, geometry, initial conditions and boundary conditions. The geometry is defined as walls (in black and yellow) and open boundaries (in red and green). . . . 61
3.3 Menisci positions and flow field for 30 kPa and 15 m/s at intervals: 4E-4 s, 9E-4 s, and 0.006 s. Puddle stays on top of the wheel and forms a ribbon of 150 µm. . . . 65
3.4 Menisci positions and flow field for 60 kPa and 15 m/s at intervals: 4E-4 s, 8E-4 s, and 8E-4 s. At this pressure the fluid leaves the simulation at the left boundary. The speed of the wheel is not sufficient to keep the puddle on top of the wheel. . . . 66
3.5 Menisci positions and flow field for 20 kPa and 25 m/s at three different intervals. At increased speed the ribbons becomes significantly thinner. . . . 67

4.1 Control system block diagram. Each block is a modelled part of the system. The arrows represent the signal or output from each block. The output is then used by the next block or presented in the control system response. . . . 71
4.2 Controlled system response. From top to bottom: In the first plot the ribbon thickness (dark blue), compared with the setpoint for the ribbon thickness (light blue). In the second plot the pressure (blue) and the simulated measured pressure (red dot). In the third plot the gap (blue) and the simulated measured gap (red dot). In the last plot the control signal (blue) and actuator input (orange) . . . 76
4.3 Uncontrolled system response. From top to bottom: In the first plot the ribbon thickness (dark blue), compared with the setpoint for the ribbon thickness (light blue). In the second plot the pressure (blue) and the simulated measured pressure (red dot). In the third plot the gap (blue) and the simulated measured gap (red dot). In the last plot the control signal (blue) and actuator input (orange) . . . 77

6.1 Sample overview. Image A is an optical micrograph of the cross section of the meltspun AlSi40 ribbon. B and C are SEM magnifications in the red area giving an overview of the phases present in the ribbon and the structure of the eutectic. D are examples of distance measurements between features found in the eutectic. . . . 83

6.2 SEM micrographs of meltspun AlSi40. Images A, B, C, D show an increasing magnification of the eutectic zone. Images E and F are magnifications of the boundary between the primary silicon crystal and the eutectic zone. 84
6.3 Multiple EDS point scans in two different areas of the meltspun AlSi40 ribbon. 85
6.4 2D EDS scan of the meltspun AlSi40 ribbon. 86
6.5 XRD measurement of the meltspun AlSi40 ribbon 87

7.1 Original AlSi phase diagram extended with the kinetic phase diagram. Using the red and green dotted lines, the kinetic composition for the AlSi40 alloy can be determined. The dotted lines show the temperature shift of the liquidus and solidus lines, caused by rapid cooling of the metal. The new eutectic point is presented with a blue star. The new composition for AlSi40 can be calculated using the lever rule presented as the green circle and red plus. . . 91
7.2 In this figure the results from the EDS line scan are compared with the results from the kinetic phase diagram and the Scheil equation. The red line represents the line scan. The green and blue lines are the calculated values with and without beam convolution. In the SEM image the line scan location and direction is presented in red and the the beam size, on which the beam convolution is based is represented by the green circle. 93
7.3 Average grain size calculations. These are based on two measurements on each grain. Results can be found in table 7.2 94
7.4 Results from the binary conversion of an back scatter SEM image. Image A is the left half of the original SEM image, image B is the result of the converted image. On the boundary a red line is plotted. On the boundary the comparison between the original grain size and the converted grain size can be made. 95

List of Tables

2.1 Process parameters, and material properties used for the calculation of the process limits . 54

3.1 Material properties of AlSi40 for the Comsol simulation 61
3.2 Comsol results 64

4.1 Thermodynamic properties 72
4.2 Control system parameters 73

5.1 Sensor requirements 79

6.1 SEM equipment and setup 84
6.2 EDS results for measurement AlSi(4), figure 6.3 of the meltspun AlSi40 ribbon. 85
6.3 EDS results for measurement AlSi(3), figure 6.3 of the meltspun AlSi40 ribbon. 86
6.4 XRD equipment and setup 87

7.1 Parameter used in the material model 90
7.2 Feature size 94
7.3 Area ratio silicon 96

1

Introduction

Rapidly solidified metals have microstructures that give rise to properties not found in other materials. With structural features ranging from 10 μm to 50 nm or even amorphous. These materials have been of academic interest for decades, due to the possible solution and improvements these properties offer in various areas such as the high-tech and automobile industries. Methods to mass produce these materials include free flow casting (FFC) and planar flow casting (PFC). Where academia is often limited to small quantities, industry needs scale in order to sustain production. At RSP technology in Delfzijl, a production facility for rapidly solidifying metal alloys by FFC is present. A test machine for the transition from FFC to PFC has been build. However, scaling the PFC process proved difficult due to the lack of research in large scale PFC processing. Furthermore the existing test machine is limited in its ability to apply commonly used control methods, that are used in literature. Therefore in this work the knowledge gained from the literature study will be applied to create a computer model of the planar flow casting process in chapter 2. This model will be used as a starting point for a comprehensive Comsol simulation of the process in chapter 3. Furthermore a control system will be designed for the implementation at the RSP facility in chapter 4. The control system will be pressure based, to prevent unnecessarily complex modifications to the current testing machine. In chapter 5 the models from the previous chapters will be the bases for the requirements of the sensor, pressure system and nozzle to be implemented at RSP.

In the second part of the work, the current material produced at RSP will be analysed. This is done in order to make it possible to compare the current material, produced by FFC, with the material produced in the future with the PFC process. In chapter 6, the results of the SEM, EDS, and XRD measurements are presented and discussed. These results are compared in chapter 7 with the material model created by combining the kinetic phase diagram and the Scheil equation. Finally the average grain size is calculated and the phase composition is checked using the area ratio of the phases.

In figure 1.1(a) an overview of the PFC process is given: Liquid metal flows from the crucible under external pressure, through the nozzle into the contact zone or gap. The rotating wheel cools the metal until solidified, resulting in the ribbon product. Contact zone area (b): In the gap a puddle is formed. The puddle is bounded by the up- and downstream menisci and the solidified ribbon. Depending on the nozzle breadth **B**, the overpressure Δp, and the wheel speed **U**, the ribbon solidifies with a certain velocity **V** and thickness τ. The ribbon (c): A ribbon with a thickness typically below 150 µm is formed with two distinguishable sides, one in contact with the wheel, and one in contact with the air. Microstructure (d): In a micrograph of the cross section of the ribbon, the microstructure is visible. In the microstructure features can range in size from 10 µm to amorphous.

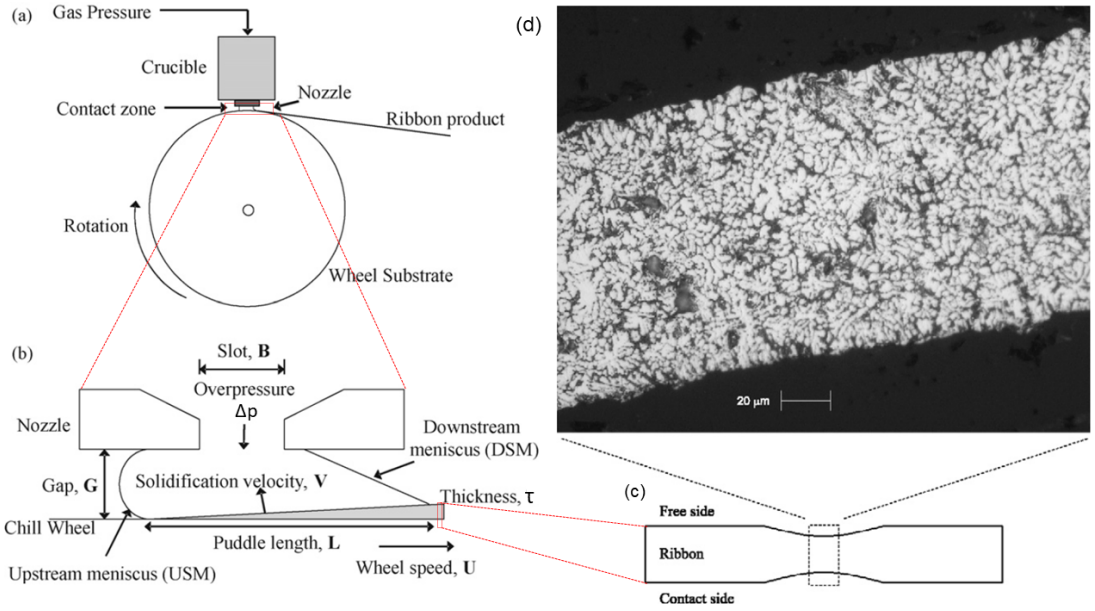

Figure 1.1: Process overview and resulting ribbon. The schematics and micrograph are adapted from Byrne et al. [1]

Part I

Preliminary Analysis

Rapidly Solidifying Aluminium Silicon Alloys

Roald Lingmont

Delft University of Technology

Faculty 3mE
Materials Science and Engineering
&
Mechanical Engineering

Date: October 1, 2023
Student number: 4473248
Course code: ME56010-20

Supervisors:
Dr. ir. SE Offerman (MSE)
Dr. ir. RAJ van Ostayen (ME)

Abstract

To further increase the cooling rate and extend the proportion of nanocrystalline and amorphous phase in the microstructure of the material produced through rapid solidification, a change from Free Flow Casting to Planar Flow Casting is considered. This investigation focuses on the analysis of the PFC process and its impact on the microstructure of an hypereutectic aluminium silicon alloy. A review on (rapid) solidification and the formation nanocrystalline and amorphous microstructure is given. Their properties and origins are examined. Additionally, modification to existing process are proposed and various methods for analyzing and comparing the influence of the process change on the microstructure are explored.

CONTENTS

I Introduction 6
I-A Applications . . . 6
I-B Research question . . . 7

II Microstructure 8
II-A Solidification . . . 9
II-B Amorphous Metals . . . 13
II-C Amorphous Properties . . . 17
II-D Nanocrystalline Metals . . . 21
II-E Nanocrystalline Properties . . . 21

III Aluminium Silicon Alloy 25
III-A Hypereutectic . . . 26
III-B AlSi40 . . . 28

IV Research methods 29
IV-A Simulations . . . 29
IV-B XRD . . . 29
IV-C SEM . . . 30
IV-D DSC . . . 31

V Process 32
V-A Fluid Mechanics . . . 32
V-B Thermodynamics . . . 38
V-C Simulations . . . 40

VI Discussion 43

VII Recommendation 43

VIII Research proposal 43

IX Search path 44

References 47

LIST OF FIGURES

1 (a) Schematic representation of the planar flow casting machine. (b) Enlarged puddle region. (c) Schematic ribbon. (d) SEM image of the intersection of a ribbon. revealing its microstructure. Reprinted and edited from Byrne et al. [1]. . . . 6
2 Gibbs free energy dependence on temperature for the solid (G^S) and liquid (G^L) phase. Where the melting temperature (T_m) is the intersection between the lines. From Easterling et al. [2]. . . . 9
3 Figures from From Fischer et al. [3] and Boettinger et al. [4] . . . 10
4 Example of nucleation rate as a functions of temperature, predicted by various methods. (a) Difference between Becker-Döring and Volmer-Weber (as equation 4). (b) Effect of the interfacial energy on the nucleation rate. From Kelton et al. [5] . . . 11
5 Schematic representation of possible T_0 curves in an binary alloy system, with their respective microstructure from Boettinger et al. [6] . . . 12
6 CCT diagram of an amorphous alloy. From Fredriksson [7] . . . 13
7 Volume and glass transition temperature dependency on cooling rate. Glass b is cooled more rapid than glass a which in turn is cooled more rapid than the crystal form. From Debenedetti et al. [8] . . . 14
8 Free energy dependence on temperature for some high GFA alloys. from Busch et al. [9] . . . 14
9 Radial distribution function of an example atomic structure. From fredriksson et al. [7], Reproduced from Cambridge University Press 1997 . . . 15
10 Electron beam diffraction results, experimental (b) and simulated, (b') to find the atomic structure (b") of an metallic glass. From Hirata et al. [10] . . . 15
11 Temperature and stress dependence of the deformation mode. From Spaepen et al. [11] . . . 17
12 TEM and HREM images of a shear band at different magnification. From Chen et al. [12] . . . 18
13 Thermal expansion of a metallic glass. From Mattern et al. [13] . . . 19
14 Diffusion rate as a function of temperature for a metallic glass. From Suryanarayana et al. [14] . . . 19
15 Temperature dependency of viscosity. From Busch et al. [15] . . . 20
16 Yield strength dependence on grain size. [16] . . . 22
17 Figures from Lu et al. [17] . . . 23
18 Schematic of diffusion paths in nanocrystalline material. i direct, ii hierarchical iii inter boundary. From Wilde et al. [18] . . . 24
19 Phase diagram of binary allow AlSi. (a): overview, (b): detail high weight fraction Al (c) detail high weight fraction Si. From Murray et al. [19] . . . 25
20 Micrographs of AlSi alloy with increasing amounts of Si. (a) $< 12.6wt\%$ (b) $12.6wt\%$ (c) $> 12.6wt\%$ From Warmuzek et al. [20] . . . 26
21 SEM image of Si particles in a eutectic mixture from Abboud et al. [21] . . . 27
22 Two samples produced under similar conditions as present at RSP Delfzijl . . . 28
23 Result from and molecular dynamics simulation of the solidification of pure aluminium with a cooling rate of 1 Ks^{-1} at 507 K. From Papanikolaou et al. [22] . . . 29
24 Results from Wesseling et al. [23] . . . 30
25 Schematic DSC plot of a metalic glass, at 40 $K\ min^{-1}$. In which T_g, T_x, and T_m are the glass transitions, crystalization, and melting temperature respectively. From Suryanarayana et al. [14] . . . 31
26 Three different outflow modes as presented by Anestiev et al. [24] In which h_f (Gap height) is either smaller (a) or larger (b) than δ_M (boundary layer), and when the flow rate is larger than the substrate velocity (c). . . . 33
27 Effect of the gap on the friction loss factor as presented by Sung et al. [25] . . . 33
28 Effect of melt overheat as presented by Praisner et al. [26]. On the vertical axis the thickness divided by the nozzle wheel gap, and on the horizontal axis the melt overheat. . . . 34
29 Schematic operating window as presented by Carpenter and Steen [27]. On the vertical axis the inertial forces, and on the horizontal axis the pressure forces. . . . 35
30 Operating window as presented by Byrne et al. [28] . . . 36
31 Transient predictions and verification by Theisen et al. [29] . . . 36
32 Ribbon thickness predictions and verification by Li et al. [30] . . . 37
33 Heat balance control volume, not to scale. from Carpenter et al. [31] . . . 38
34 Idealized problem model, not to scale. from Carpenter et al. [31] . . . 38
35 Minimum heat transfer coefficients for various alloys. from Carpenter et al. [31] . . . 39
36 Three temperature curves from Tkach et al. [32]. Curve 1 and 2 are for amorphous ribbons. Curve 3 is for a crystalline ribbon . . . 39
37 Three cooling rate from Tkach et al. [32]. Curve 1 and 2 are for amorphous ribbons. Curve 3 is for a crystalline ribbon . . . 40

38 Comparison between simulated results for initial flow development from Liu et al. [33] (left) and experimental results from Wilde et al. [34] (right). Both images are edited versions of the original. 41
39 Temperature profiles and streamlines in the melt puddle from Liu et al. [33] at 4.3 seconds 41
40 Temperature profiles below the puddle from Liu et al. [33] at 4.3 seconds 41
41 Results from Liu et al. [33] 42
42 Topics part of mechanical engineering included in RSP 44
43 Topics part of material science included in RSP 45

LIST OF TABLES

I Results from Abboud et al. [35] 27
II Variables of the planar flow casting process from Su et al. [36] 32
III Number of sources on the various subtopics of the rapid solidification process 46
IV Author or co-author with 3 or more papers used in this review 46

I. Introduction

Rapid Solidification Processing (RSP) is a method for producing specialized materials for high-tech applications. By exceeding cooling rates of $10^5 Ks^{-1}$, the (near) equilibrium phase of metals is not reached and instead a highly refined metastable microstructure is produced. This results in properties not found in metals produce through conventional processes such as die casting. RSP Technology in Delfzijl [37] [38] uses a melt spinning variant called Free Flow Casting (FFC) for their production process. In FFC a stream of molten metal is poured through a nozzle onto a spinning chilled wheel. This creates a puddle on the wheel from which a solidified metal ribbon is pulled. The thickness of the ribbon is closely related to the rotational speed of the wheel [39]. Decreasing the thickness of the ribbon, increases the solidification rate. It is however not possible to just keep increasing the wheel speed, because there is a fine balance in which the process is stable and the puddle stays on top of the wheel. When the wheel rotates exceeds a certain speed, droplets of molten metal are flung away from the wheel. To further decrease the ribbon thickness, the wheel can be brought closer to the nozzle to hold the puddle stable between the nozzle and the wheel. This method is called Planar Flow Casting (PFC) [40]. In order to reach even higher cooling rates, RSP Technology wishes to transition from FFC to PFC. In this work the implementation of PFC at the test facility of RSP Technology is studied, along with its effects on the microstructure of the produced ribbon. An overview of the process and the some of the relevant parameters can be seen in the work of Byrne et al. [1] printed in figure 1.

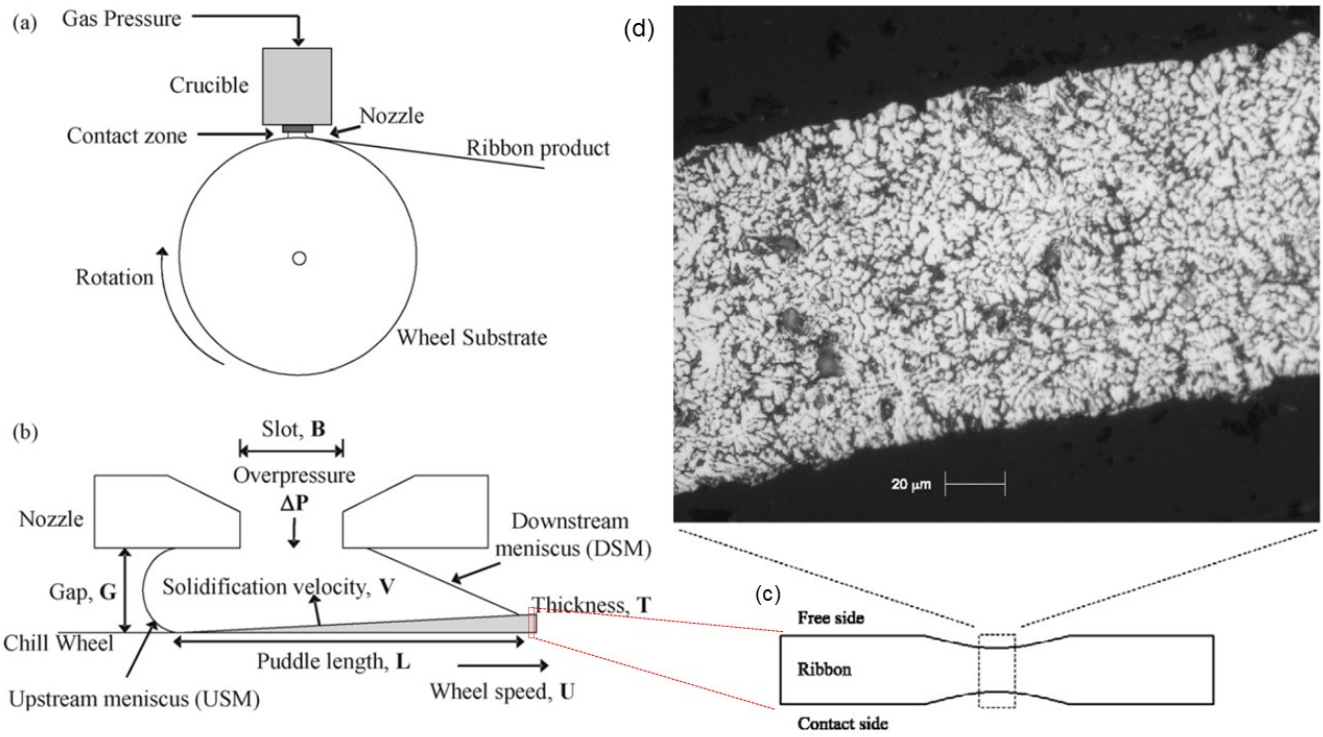

Fig. 1: (a) Schematic representation of the planar flow casting machine. (b) Enlarged puddle region. (c) Schematic ribbon. (d) SEM image of the intersection of a ribbon. revealing its microstructure. Reprinted and edited from Byrne et al. [1].

A. Applications

A good understanding of the PFC process is essential for the creation of novel materials, which can be used to solve the technological challenges of the future. The PFC process is complex, consisting of a combination of fluid dynamics, thermodynamics and materials science. Applications of rapidly solidified metals are plentiful, from permanent magnets without rare earth metals [41], to satellite mirrors. Improvements in the properties of these materials, for example, improve the image quality of a space telescope or increase the efficiency of power electronics [42]. By increasing cooling rates, a finer microstructure is achieved, which allows for a stiff and thermally stable mirror that can be finely polished [43] [44]. Other application areas include semiconductor manufacturing, in which the combination of high stiffness, low weight, and thermal stability are important criteria and engine components, that require high strength and fatigue resistance at elevated temperatures at minimal weight [45].

B. Research question

In order to assess the new production process, it is necessary to determine, whether changing from free flow casting to planar flow casting increases the percentage of nanocrystalline or amorphous phase in the melt spun ribbon. Therefore the existing production machine will need to be upgraded with a gap control and a pressure regulating system. Sensors and software need to be added in order to monitor the key parameters of the PFC process. Using simulation and optimization the parameters will be chosen with which the new sample ribbons will be cast. Finally the atomic structure of the ribbons will be compared with the predicted result and with the ribbon produced with FFC. X-ray diffraction (XRD) and scanning electron microscopy (SEM) will be used to analyse and quantify the microstructures.

II. Microstructure

Rapidly solidified metals are metals which are rapidly cooled from liquid to solid state during which the atoms have very little time to order themselves in the lowest energy state possible. Two distinctions in microstructures can be made depending on solidification rate: amorphous structure and nanocrystalline structure. If solidification is fast enough the metal is essentially frozen in its liquid structure and doesn't have time to crystallize. This structure differs much from the equilibrium structure of metals, there are no precipitates, phase separation doesn't take place, no crystals form and therefore no grain boundaries exist. If solidification happens at a slower pace, nanocrystalline structures are formed. Nanocrystalline metals contain many more grain boundaries than conventional metals. Both amorphous and nanocrystalline materials have properties not commonly found elsewhere, which makes them interesting for research and high-tech applications. Multiple methods are available to produce rapidly solidified metals. These are compiled in the works of Lavernia et al. [46] [47]. However most of these methods are not cost effective for large scale industrial production. The methods that are economically viable are the ones using one or two rolls, on which the metal can cool. Of these methods, two are in use at the RSP plant in Delfzijl. These are: free flow casting, and planar flow casting. During free flow casting a jet of molten metal flows through a nozzle against an actively cooled rotating wheel. The volumetric flow rate and wheel speed are chosen, such that the molten puddle stays on top of the wheel whilst a solidified ribbon is pulled out of the puddle. During planar flow casting a jet of metal is forced through the nozzle and the gap between the nozzle and the wheel. The difference with free flow casting is that the formed puddle is held between the wheel and the nozzle making it more stable. Therefore it is possible to increase the speed of the wheel resulting in a higher cooling rate and thinner ribbon. Other improvements that can be made are the surface finish of the wheel. When for instance a finer microstructure is desired, a surface finish which increases nucleation at the wheel can be chosen. Additional steps are required to get the material ready for large scale applications, which is now limited by the size of the ribbon. After the ribbon is solidified, it is chopped up into smaller flakes in order to prepare it for hot isostatic pressing. During pressing the flakes fuse together in order to form a solid piece of material, from which parts and products can be machined. This method is used in order to minimize the effect on the microstructure of the flakes. These last two steps are outside the scope of this project.

A. Solidification

Solidification in liquid metals is a process involving heat transfer, fluid flow, diffusion and nucleation. During solidification metal transition from a liquid state to a solid state, that is either crystalline or amorphous (glass like). Within these states, large variations are possible. In crystalline metals, grain size and compositions changes depending on the alloy, cooling rate, and subsequent heat treatment(s). In amorphous metals the varying parameter is the density. Solidification is a consequence of the removal of heat from the liquid. The heat is transferred from the liquid to the cooler surroundings. The exact nature of the heat transfer determines the temperature gradient and cooling rate within the material. The cooling rate determines the time available for nucleation and viscous flow within the liquid and consequently the microstructure of the solidified material. A good understanding of solidification mechanics is a prerequisite for good control over the microstructure during the melt spinning process.

When the cooling rate and alloy composition allow it, crystallization will occur. The driving force for crystallisation is the difference in the Gibbs free energy of the liquid and the solid. This energy is temperature dependent, and is a combination of enthalpy and entropy according to equation 1. The difference in energy with temperature is according to equation 2. However the temperate dependence of this equation is different for each phase according to equation 3 and schematically presented in figure 2. When the melting temperature is reached, the Gibbs free energy of the solid is equal to that of the liquid. Now atoms are able to order themselves in a crystal lattice to decrease the Gibbs free energy as much as possible. There is however an energy barrier before this process can happen. When atoms start to clump together, interfacial energy is formed. This energy, plus the difference in Gibbs free energy has to be lower than that of the liquid, in order to form a stable solid phase. Therefore, an undercooling of the melt, a temperature below the melting temperature, is needed to overcome this energy. When a stable nucleus is formed, atoms from the liquid phase will start to attach to the nucleus. Due to the lower energy of the crystal, heat is generated during crystallization. The speed at which this heat can be transferred, controls the solidification speed. At the interface of the growing crystal the temperature is slightly below the melting temperature. If the liquid is cooled rapidly, the temperature can drop far below the melting temperature of the liquid, creating a large undercooling before nucleation happens. This greatly increases the rate of solidification.

$$G = H - TS \tag{1}$$

$$\Delta G = \Delta H - T\Delta S \tag{2}$$

$$\Delta G = H_{Solid} - H_{Liquid} + TS_{Solid} - TS_{Liquid} \tag{3}$$

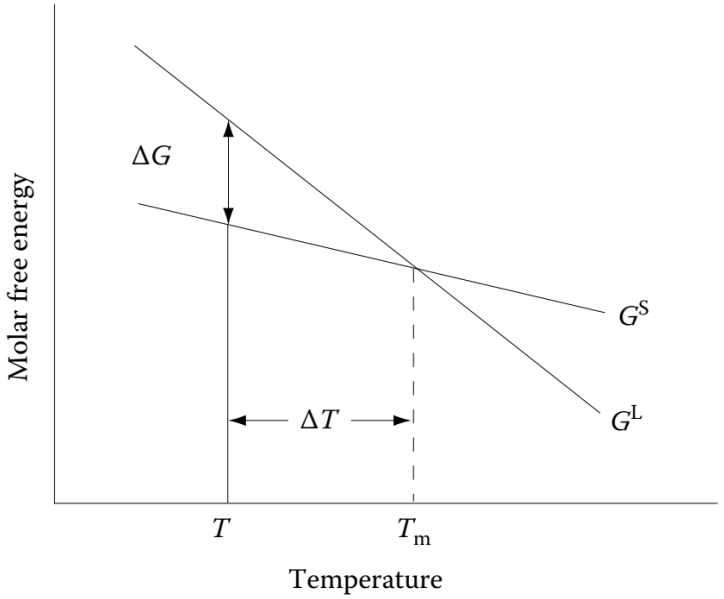

Fig. 2: Gibbs free energy dependence on temperature for the solid (G^S) and liquid (G^L) phase. Where the melting temperature (T_m) is the intersection between the lines. From Easterling et al. [2].

Nucleation in a liquid is a stochastic process. Atoms are constantly moving and bumping into each other. Due to this random movement, sometimes a few atoms form a cluster called an embryo [7]. In an undercooled liquid some amount of clusters are always randomly present with varying radii. If these clusters have a radius greater than a critical radius they are stable and can nucleate. If they are too small, the cluster will be broken up by other atoms bumping into it with high energy. The critical radius is determined by the Gibbs Thomson effect. This effect describes the interfacial energy of a curved surface. The interfacial energy decreases with radius. This is because the free energy of the volume decreases faster than the free energy of the interface grows [4]. This can be seen in figure 3a where ΔG_i is the interfacial free energy ΔG_v is the volumetric free energy of the cluster. If the interfacial energy can be overcome by undercooling, the embryo becomes a stable nucleus. From this nucleus a crystal starts to grow. This process is called homogeneous nucleation, it happens throughout the liquid. In contrast there is heterogeneous nucleation. More often solidification occurs due to container walls or contaminations, schematically represented in figure 3b, these lower the interface energy of the system. The interface energy is dependent on the structure of the surface, and decreases with a factor called the shape factor [4]. Therefore nucleation will start at a smaller undercooling than homogeneous solidification. By choosing a surface with liquid specific features (roughness and wetting angle), and bringing as many atoms as possible in contact with the surface, nucleation rate can be maximized. Furthermore, introducing specific contamination called inoculants to the melt, nucleation rate can be increased by increasing the nucleation sites [5]. By designing specific inoculants, control of nucleation temperature and crystal size is possible. A catalyst with a specific size and shape will lower the nucleation temperature to a desired number, then nucleus growth is limited by the size of the inoculant due to the interfacial energy [4].

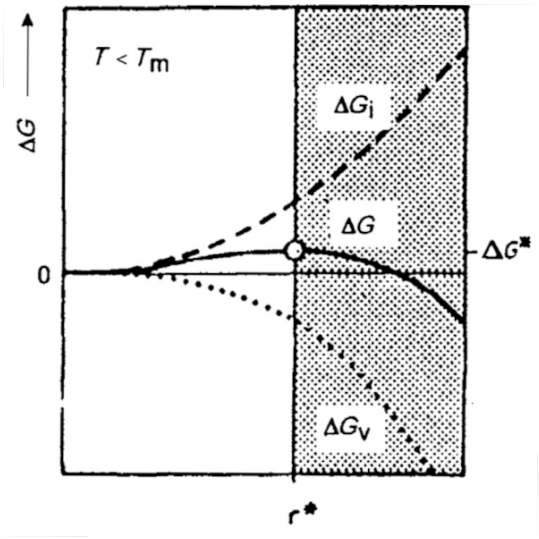

(a) Interfacial and Volumetric free energy dependence on cluster radius (r), r* is the critical radius. From Fischer et al. [3]

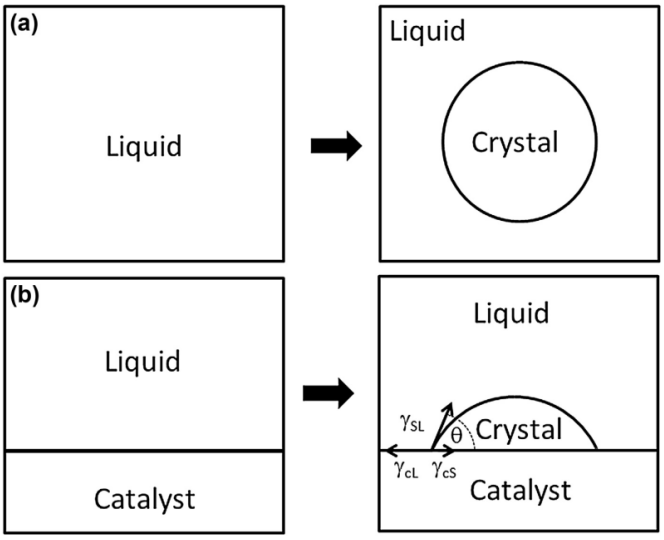

(b) Homogeneous nucleation (a) and Heterogeneous nucleation (b) from Boettinger et al. [4]

Fig. 3: Figures from From Fischer et al. [3] and Boettinger et al. [4]

The rate of nucleation is a function of the amount of critical clusters present in the melt, multiplied with the frequency at witch atom attach to this cluster. The amount of critical cluster present is determined by the undercooling of the melt, latent heat of crystallization, melting temperature, and the interfacial energy. With the interfacial energy decreased by a factor for heterogeneous nucleation. The attachment rate is dependent on the atomic vibration frequency. Predicting the nucleation rate with theory is a difficult problem. Classical nucleation theory attempts to predict steady state homogeneous nucleation rate. This situation is not commonly found in real-world applications, but does give insight into the varying factors playing a role in nucleation. A simplified equation from classical nucleation theory is presented in equation 4. In this equation $W(n^*)$ is the nucleation barrier, which determines the formation of large enough clusters. A^* is a prefactor which includes the growth rate of the clusters. I is the nucleation rate, k_B The Boltzmann constant, and T the temperature. A correct prediction of this factor is difficult and there can be orders of magnitude difference between predicted and observed values, mainly caused by assumptions around interfacial energy [5]. This greatly limits the applicability of the theory. In figure 4 an example of nucleation rate with respect to temperature is plotted, furthermore the effect of the interfacial energy on the nucleation rate can be seen. From these figures it can be seen that the nucleation significantly rises with undercooling. This increase happens from 0.2 T_m to 0.4 T_m. This defines the nucleation temperature [4]. If the temperature drops further, a nucleation rate maximum will be reached, until eventually nucleation will decreases again, due to slow atom movement.

Another effect of a large undercooling is the ability to nucleate metastable phases. A metastable phase has a lower nucleation barrier for heterogeneous nucleation but a higher Gibbs free energy for the bulk. Only when solidification is fast enough can this metastable phase form, otherwise there is time for the more stable phase to nucleate.

$$I = A^* \exp\left(-\frac{W(n^*)}{k_B T}\right) \tag{4}$$

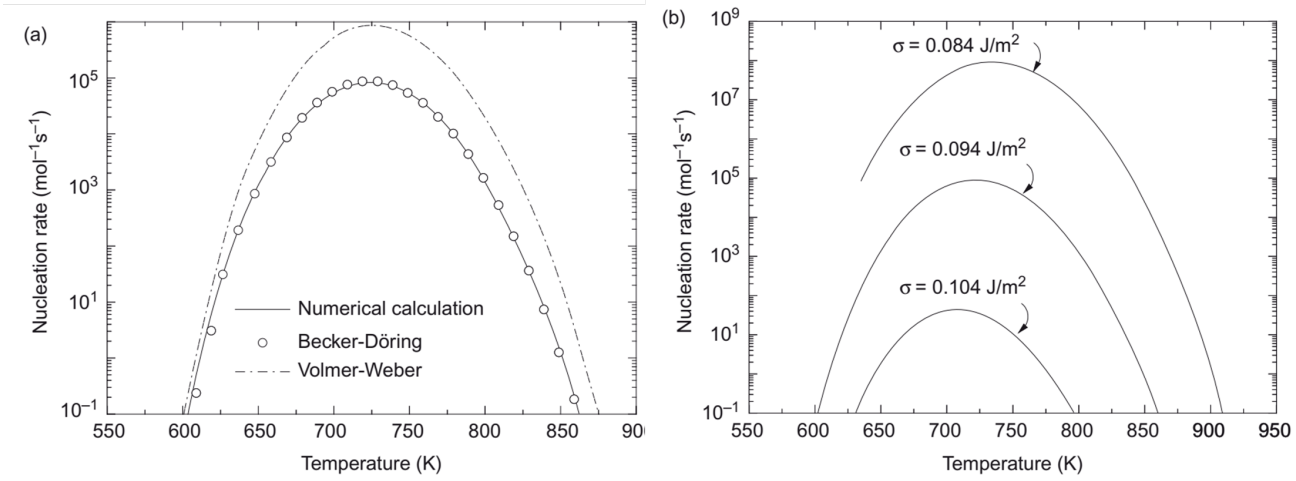

Fig. 4: Example of nucleation rate as a functions of temperature, predicted by various methods. (a) Difference between Becker-Döring and Volmer-Weber (as equation 4). (b) Effect of the interfacial energy on the nucleation rate. From Kelton et al. [5]

The crystal growth rate is the speed with which the solid-liquid interface moves. This is the rate a which atoms jump the interface and move from the liquid to the solid. If the metal is not alloyed, only the amount of supercooling at the interface is of influence of the speed. However for alloys, diffusion plays an important role. Depending on the metal, crystals can grow continuous or layer by layer. Most metals grow in a continuous fashion [4]. During continuous growth the interface is rough and there are many lattice sites, multiple layers deep for the atom to jump to. If roughness is very low the crystal grows layer by layer at a slower rate. As with nucleation, the rate of this process increases with undercooling until it reaches a maximum. There the decrease in atom movement due to the low temperature gets the upper hand and the crystal growth rate decreases again. Maximum crystallization rate is limited by the collision rate of the atom, which is strongly linked with the speed of sound in the metal. The general equation for the crystal growth rate dependence on temperature is presented in equation 5. This equations consists of a solidification driving force and a factor describing the interface mobility. In this equation $V_C(T^*)$ is the forward flux of atom from the liquid to the solid phase, if the driving force would be infinite.

The driving force dependent on temperature is expressed as $[1 - \exp\left(\frac{\Delta G}{RT^*}\right)]$. T^* is the temperature at the interface. If cooling is slow and the system is near equilibrium, the growth speed can be linearized, with a linear coefficient μ, according to equation 6. Values for μ lie in the range of $10 - 200\ cms^{-1}K^{-1}$ for different metals [4]. For crystals that grow layer by layer the speed of crystal growth is dependent on the nucleation rate on each layer. Therefore as with nucleation there is a temperature at which the growth rate increases rapidly. Alloyed system are more complex. In these systems diffusion has an effect on the growth rate. Apart from interfacial energy between the solid and the liquid, also a driving energy by mixing of the atoms exist. At low cooling rates diffusion has time to mix the atoms in their preferred alloy configuration and segregate out different phases, but when cooling rates is increased this time is not available. This can drive up the concentration of solute atoms around the interface, which get stuck in the lattice. These solute atom can be disorder (amorphous) or form their own phase with a different composition. In extreme cases there is no segregation and the crystal structure consists of one phase only [4].

$$V(T) = V_C(T^*)[1 - \exp\left(\frac{\Delta G}{RT^*}\right)] \tag{5}$$

$$V(T) = \mu \Delta T_k \tag{6}$$

When an alloy solidifies, it normally crystallizes first at the most stable composition. This temperature and composition is this liquid-solidus line in the phase diagram. When an alloy rapidly solidifies, the composition is closer to that of the liquid. The T_0 temperature is highest temperature at which this can happens. The composition created at this temperature can be plotted on the phase diagram. This is called the T_0 curve and it describes the limit of the extended solubility created with rapid solidification. The phases that form at these cooling rates are metastable. Outside of this range no crystal phase can form, but instead the metal will freeze to an amorphous structure. Depending on the alloy, the T_0 curves can be either crossing, plunging or continuous. A plunging curve indicates low solubility extension and high glass forming ability. Depending on the crystal structures present on the edges of the phase diagram, the T_0 curves can either cross or be continuous [6]. Different crystal structure will result in crossing T_0 curves. An schematic examples is given in figure 5

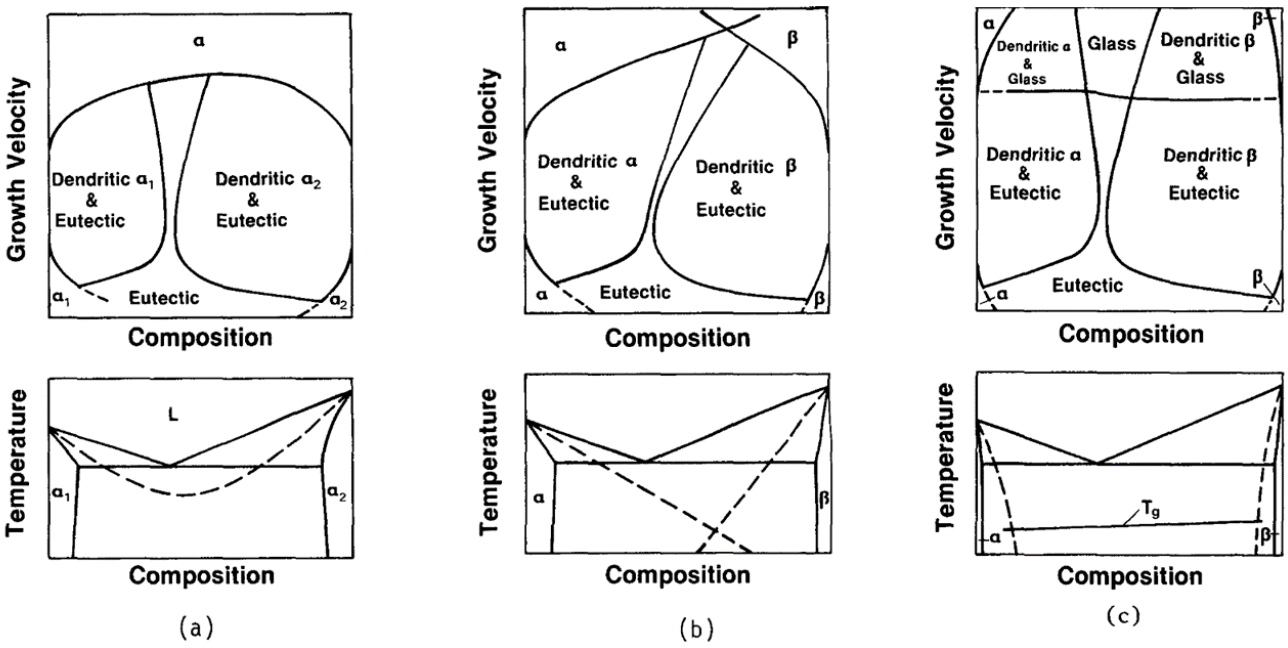

Fig. 5: Schematic representation of possible T_0 curves in an binary alloy system, with their respective microstructure from Boettinger et al. [6]

B. Amorphous Metals

The difference between a “normal” metal, and an amorphous metal, also called a metallic glass, is the structure of the atoms in the solid state. In a metal that is slowly cooled and is close to the equilibrium state the atoms exists in a crystal lattice. This is the structure in which most metals normally exist when solidified. In a metallic glass however there is no crystal structure present. The structure is not random but similar to that of the metal in liquid form [48]. By cooling the liquid metal fast enough, the increase in viscosity will hinder the atoms from moving to their lattice position in time. Essentially freezing the atoms in place. At this point the material will reach a semi stable state. The temperature at which this happens is the glass transition temperature, and is dependent on cooling rate [7]. This is the temperature at which no structural changes take place anymore. The viscosity is now in the order of $10^{12} Pa \cdot s$ [8]. A schematic of this process is displayed in the continuous cooling transformation diagram in figure 6. It shows that, with a temperature curve steep enough, crystallization can be prevented.

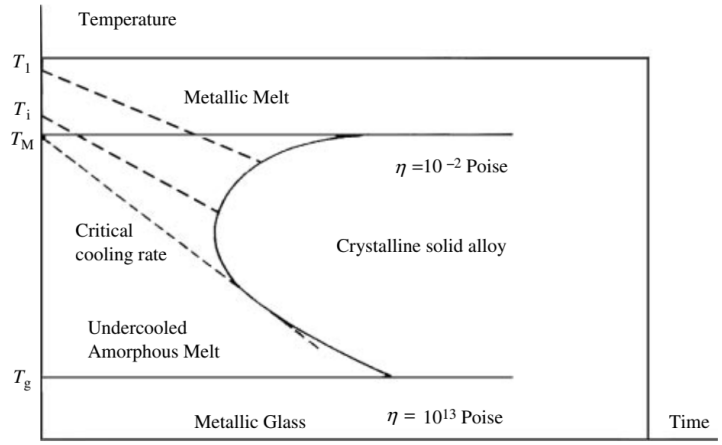

Fig. 6: CCT diagram of an amorphous alloy. From Fredriksson [7]

If the cooling rate is high, the glass transition temperature will be higher. This is because the liquid is frozen earlier, and will therefore have the properties and structure of a higher temperature liquid. Therefore depending on the cooling rate, different glass states can exist, with different densities. If the cooling rate is reduced and more movement is possible the material will become denser. The structure will however not reach the density of the crystalline material. The liquid structure is not as well packed as the crystal structure, as can be seen in figure 7.

The cooling rate necessary to form metal glass, is different for every alloy composition. The lower the cooling rate required, the easier it is to produce the metallic glass. This is called the glass forming ability (GFA) [48]. A metal can only crystallize below its crystallization temperature, and cannot change structure below its glass transition temperature. So to increase the GFA the gap between these temperatures must be chosen as small as possible. One way to do this is to choose an alloy composition with a deep eutectic. In this composition the liquid is as stable as possible and therefore the crystallization temperature relatively low. Deepening the eutectic is possible with specific alloying elements. The atoms in this alloy should differ in size by more than 12 % and have a negative heat of mixing. These properties hinder crystallization and therefore decrease the crystallization temperature. Finally the deepest eutectic are made with 3 or more alloying components [49]. The effects of the alloying components can be seen in the driving force for crystallization.

The driving force for crystallization is the change in Gibbs free energy between the liquid and the solid phase ΔG 3. Adding alloying elements to a liquid increases the the possible states of the system and therefore the entropy. This means that at elevated temperatures the liquid becomes more thermodynamically stable [14].

This can be seen in figure 8 where ΔG is related to super cooling. The relation starts of linear, with a slope dependent on the alloying elements. More alloying elements decrease the slope. When the temperature decreases further, ΔG becomes independent of super cooling. This means that equal entropy between the liquid and crystal structure is reached, and therefore that the liquid is in a highly ordered state. This happens sooner for highly alloyd metals. In figure 8 This effect can be seen for some high GFA alloys. GFA is heavily dependent on crystal grow speed, so key is to minimize growth rate.

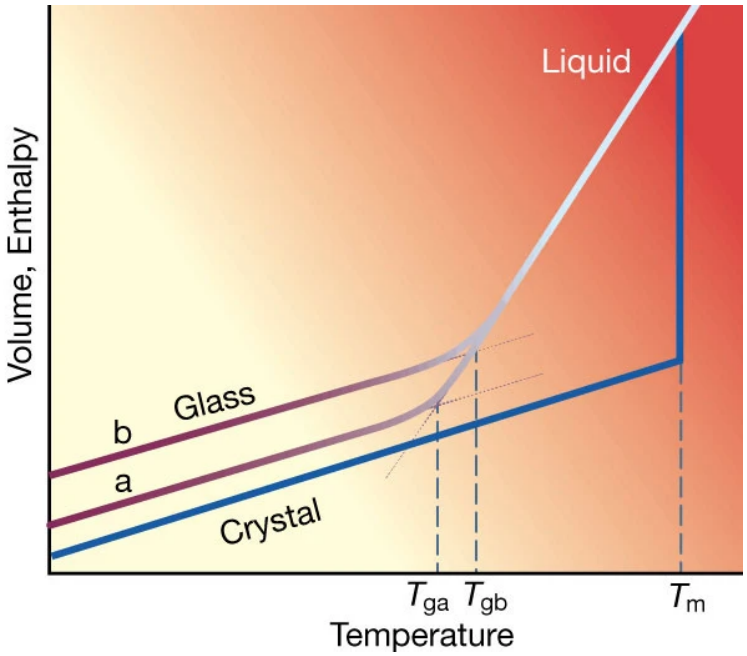

Fig. 7: Volume and glass transition temperature dependency on cooling rate. Glass b is cooled more rapid than glass a which in turn is cooled more rapid than the crystal form. From Debenedetti et al. [8]

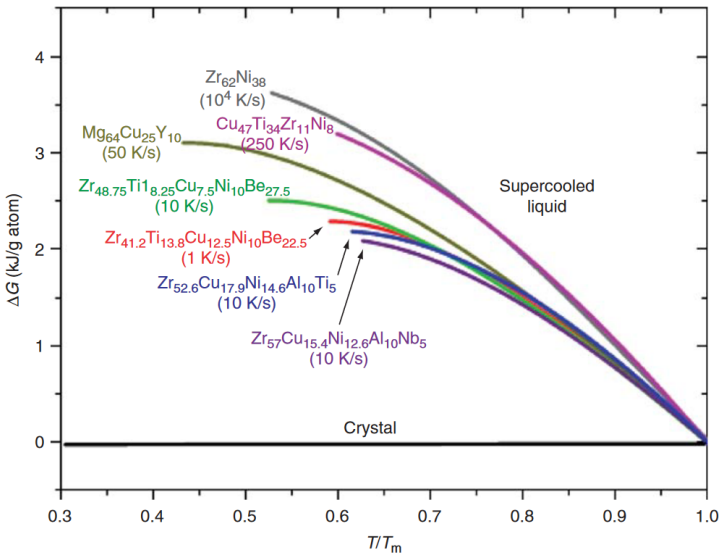

Fig. 8: Free energy dependence on temperature for some high GFA alloys. from Busch et al. [9]

Although the metal atoms are not part of a crystal lattice, they are not randomly distributed either. A certain structure is present in the amorphous state of the metal, which is similar to the structure found in the liquid state [7] [48]. As mentioned earlier there can be so much structure present that the entropy is similar to that of a crystalline metal. The material however does not have grain boundaries or dislocation since this can only be defined in a crystalline metal. The structure of an amorphous metal can be described on a local atomic scale. To describe the structure present in the amorphous state, an averaged correlation function is used. It is assumed that the result of this function locally, is the same throughout the whole volume. Specifically the radial and partial radial distribution functions are used as can be seen in equation 7. These functions count the number of atom present in an infinitesimal slice radially outward from a centre atom. From the resulting plot it can be seen that not every distance is equally likely to have another atom, but that the probability of there being another atom is distributed in a damped wave like function. A schematic representation of such structure with according plot of the radial distribution function can be found in figure 9.

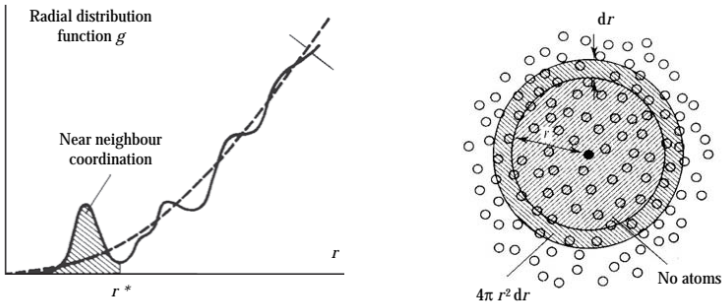

Fig. 9: Radial distribution function of an example atomic structure. From fredriksson et al. [7], Reproduced from Cambridge University Press 1997

$$g = 4 \cdot \pi r^2 \rho dr = \frac{dN}{dr} \tag{7}$$

The pair distribution function can experimentally be obtained via X-ray, neutron, and/or electron diffraction. These techniques are however not sufficient to completely describe the atomic structure present in the metal. To find out where the atoms are around the central atom and what their position is relative to each other, another measurement method is needed. This can be done with a combination of simulation, transmission electron microscopy and nanobeam electron diffraction (NBED) technique. Hirata et al. compared experimental results from NBED, with simulations of the same NBED procedure in a molecular dynamics simulation, to find the 3D atomic structure of a metallic glass [10]. One of the results from Hirata et al. can be seen in figure 10.

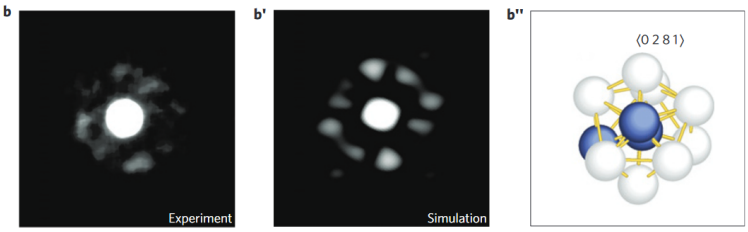

Fig. 10: Electron beam diffraction results, experimental (b) and simulated, (b') to find the atomic structure (b") of an metallic glass. From Hirata et al. [10]

The results could be similar to that of a nanocrystalline material, in which the crystals are only a few atom large. However by calorimetric measurements it can be shown that during annealing, nucleation takes place instead of only grain growth. From these experiments and simulations, models can be made and verified. A successful model is the efficient cluster packing model [50]. In this model solvent atoms form clusters around a central solute atom. The cluster shape and size, or the amount of atoms around the central atom, is based on the ratio of the radii of the different atoms. Based on the ratio different cluster types can form, from tetrahedral, to icosahedral clusters with an amount of non-centre atoms between 3 and 24. On a larger scale these cluster are packed together such that solute atoms share a common solvent atom. A consequence of this clustering is a stabilizing effect on the liquid, and therefore lowering of the melting temperature. The cluster hinder the formation of crystals in the liquid, because they are more stable than randomly ordered atoms. The clusters also increase the viscosity of the liquid, which also has a hindering effect on crystallisation. This is why the relative size of the different atoms, have a large effect on the GFA [48]. The reason for negative heat of mixing also becomes clear here. The amount of clusters that form and their stability are effected by the attractive forces between the solvent and solute atoms. A more negative heat of mixing, means a higher force, therefore more stronger clusters, increasing the GFA.

As mentioned earlier it is possible to create different amorphous structures based on the cooling rate. Slower cooling increases the density of the metal. Structural changes can also be made by annealing or relaxing the metal. During this process no crystallisation takes place, only small structural changes. These changes can be dived into chemical and topological short range order changes. During chemical change, there is atomic transport and the structure is reordered. During topological change there is only a change in the inter atomic distances without major restructuring of the atoms. Despite these being small, the effect on the properties of the material are significant. Density increases, and atomic mobility and diffusivity decrease. Most other material properties change as well [48]. It is possible change from one glassy state to another near the glass transition temperature. A new stable state can be reached, by keeping the material at the desired temperature for long enough. This state can be reached both ways, from low and high T_g states. Apart from relaxing the metal, it is also possible to reverse this effect and make the metal less relaxed. This can be done by mechanically loading the material. The will increase the free volume and decrease its density, basically reversing the relaxation process.

C. Amorphous Properties

Structural difference between crystalline and amorphous metals give rise to a difference in mechanical properties. The amorphous metal lacks grain boundaries, interstitials, crystal defects, and slip planes. This means that amorphous metals have a different deformation mechanism than conventional metals. Three mechanisms can be distinguished, depending on temperature and stress [14]. When the stresses are low and the temperature is below the T_g the metal experiences creep, a slow homogeneous viscous flow. The flow is linearly proportional the to applied stress, such as in a Newtonian fluid. If the temperature is raised above the T_g, flow increases and the metal is easily deformed. At this temperature the metal starts behaving non-Newtonian, with decreasing viscosity at increased stress. When high stresses are applied, deformations takes place in shear bands, these are bands of at the most a few hundred atoms thick, along which deformation takes place. The flow is now concentrated in these bands and therefore not homogeneous anymore. Mechanical failure occurs along these bands, and are therefore the determining factor of the yield and ultimate strength of the metal. If the temperature is low the metal behaves brittle with sudden failure. At higher temperatures sudden failure will be avoided, with high elongation past the yield point. The different modes of deformation can be plotted in a deformation map, see figure 11. In this map stress is plotted against temperature, in order to capture the deformations modes described earlier.

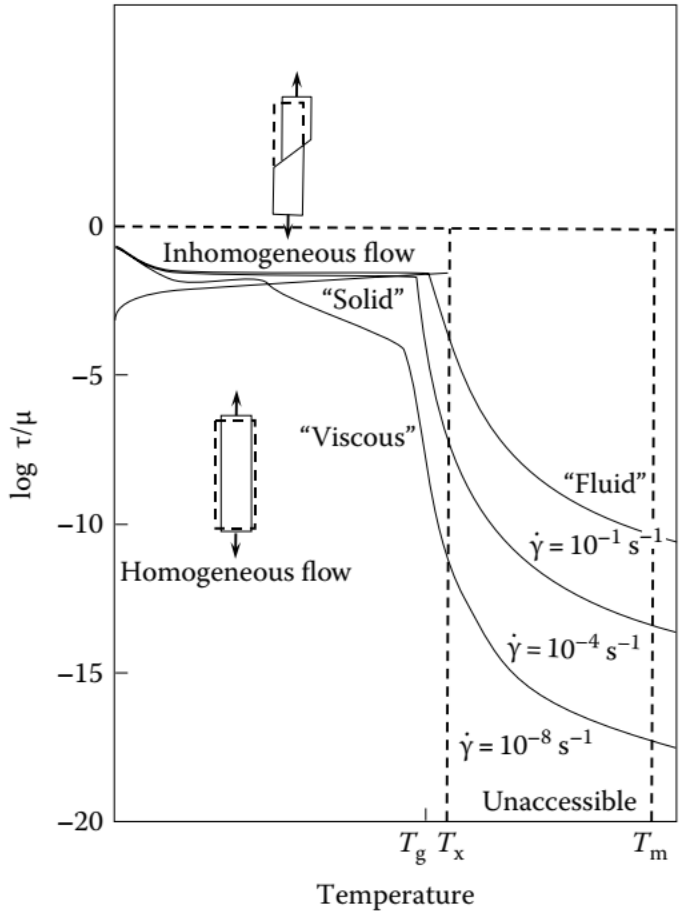

Fig. 11: Temperature and stress dependence of the deformation mode. From Spaepen et al. [11]

Shear banding determine the following properties in amorphous metals: strength, fatigue strength, plasticity, and toughness. Shear bands are the mechanism for deformation and failure. In the shear band free volume is increased, this locally lowers the viscosity, which promotes material flow. The material starts straining in these bands causing local temperature rise. This temperature rise causes a further decrease of viscosity, leading to even more strain and more heat. These self-amplifying effects eventually lead to failure. Chen et al. [12] captured transmission electron microscopy (TEM) and High-resolution electron microscopy (HREM) images of a shear band, as can be seen in figure 12.

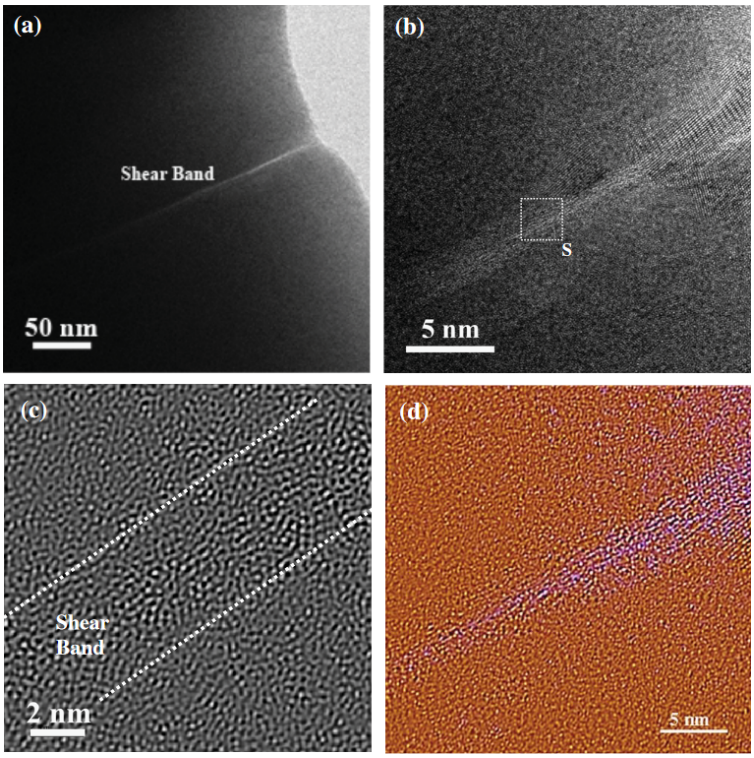

Fig. 12: TEM and HREM images of a shear band at different magnification. From Chen et al. [12]

Shear bands also greatly reduce the fatigue strength of an amorphous metal. They arise easily at stress concentrations, and create fatigue cracks in the material. More shear bands are created along the crack, which further facilitates the crack. The amount of shear bands and their proximity to each other determine the toughness and plasticity of the material, which is usually lacking in glassy materials, compared to crystalline. There is often a trade-off between strength and toughness because of the increased brittleness in stronger materials. However with the right composition of an amorphous metal both properties can exist. When the composition promotes the creation of shear bands, material flow can be distributed over multiple bands, spreading the generated heat more evenly. This decreases the self-amplifying effect that leads to failure. This however does decrease the strength of the material. To counteract this, a change in the local structure can cause a reduction in the propagation of the shear bands. This can be a local increase in density, or introduction of crystalline zones in a amorphous crystalline composite material. Such a composite can have a desirable combination of properties from the amorphous and crystalline material.

Apart from special mechanical properties, amorphous metals also differ in other aspects. The thermal expansion, diffusivity, specific heat, and viscosity are discussed next. The coefficient of thermal expansion (CTE) of metallic glass is often larger than their crystalline counterparts. Thermal expansion is generally linear below the T_g. The exact CTE of the glass is dependent on multiple factors. It is dependent on the cooling rate of the material, and if it is relaxed or annealed afterwards. If the material is not relaxed, structural changes still take place in the material upon temperature change. When the material is heated, relaxation takes place which increases the density of the material, and therefor shortens the sample, decreasing its thermal expansion. This change in thermal expansion is permanent, and can only be reversed with a complete restructuring of the material by heat treatment. Thermal expansion without major restructuring of the atoms also occurs. In this case the spacing between the atoms change, but they don't change places. This process is reversible, and could therefore be described as a stable CTE. In figure 13 a plot of the thermal expansion of a metallic glass can be seen. Non-reversible structure change takes place around the glass transition temperature, measuring this sample again would therefore will have a different result.

Diffusion plays an important role in structural changes within the amorphous metal. Relaxation by chemical reordering and crystallization are processes driven by diffusion. Therefore it gives insight into the stability of the structure of the material. Diffusivity and relaxation are both temperature dependent processes and also depended on each other. Higher temperature means faster diffusion but also faster relaxation, which in turn decreases diffusion due to the decrease in free volume. Only when the relaxation is complete will the diffusivity reach a stable value. At low temperatures this practically never happens due to the very slow structural changes.

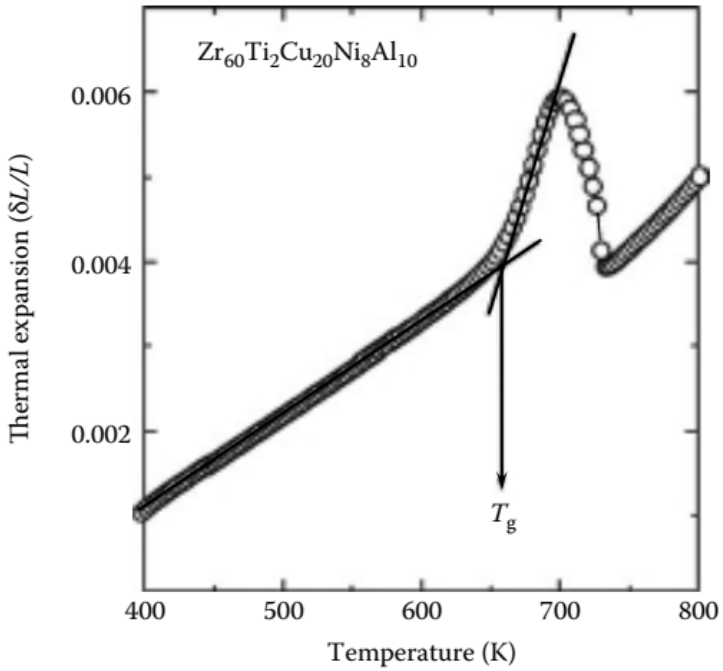

Fig. 13: Thermal expansion of a metallic glass. From Mattern et al. [13]

At temperatures below the T_g the process of diffusion is similar to a crystalline material. Where individual atoms move to free locations in the structure (excluding grain boundary diffusion). However at super cooled liquid temperature the method of diffusion is different. At this temperature range, diffusion happens with more atoms at the same time. Atoms around the hopping atom change structure to accommodate the moving atom. Therefore this mechanism is called cooperative, instead of hopping below the T_g, which is called non-cooperative. Cooperative hopping happens at a far greater rate than non-cooperative hopping. In the diffusion rate graph in figure 14, a kink can be seen around the T_g, where diffusivity suddenly changes to a higher rate when the T_g is reached [14].

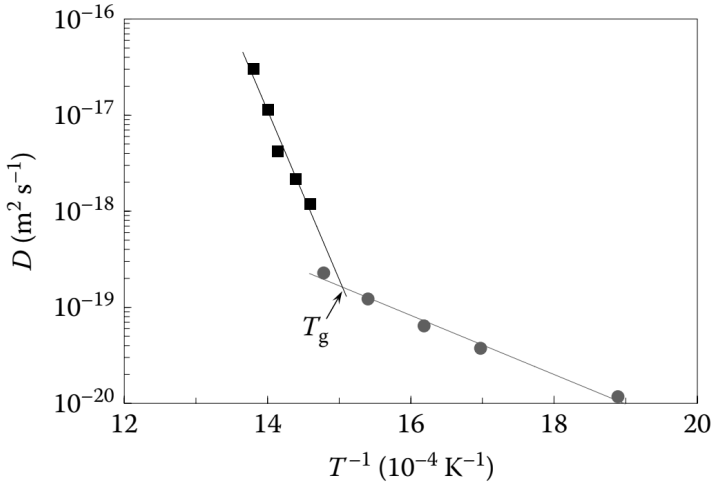

Fig. 14: Diffusion rate as a function of temperature for a metallic glass. From Suryanarayana et al. [14]

The specific heat of an amorphous metal is informing of the amount relaxation of the material. Non-relaxed samples have a temporary decreasing specific heat when heating to the T_g, due to the relaxation happening in the material. This is a one time effect, when repeating this experiment with the same sample, specific heat will slowly increase with temperature until the T_g is reached. The specific heat will rapidly decline when the supercooled liquid starts to crystallize.

Furthermore, the specific heat of amorphous metals is especially interesting for the design of the melt spinning machine and the simulation of the cooling process. Since no crystallisation takes place, less heat has to be absorbed by the wheel, meaning lower cooling requirements. However if crystallization does take place the wheel will heat more than expected causing more crystallization resulting in an unstable process. The greater the difference between the amorphous and crystal the more difficult it is to form the glass.

Viscosity is an important parameters for the GFA of an alloy. The way viscosity changes with temperature is a good indication for the stability of the liquid and glass. The higher this stability, the less likely it is for crystallization to occur and the easier it is to form a glass. Liquids can be divided into strong and fragile liquids. In strong liquids the temperature dependence of the viscosity is high. Viscosity decreases with decreasing temperature according to Arrhenius equation 8, which relates reactions rates with temperature. In strong liquids the viscosity is high near the melting point. These liquids also have a high GFA. Fragile liquids in contrast have a stable viscosity, until the T_g is approached, only then the viscosity drops rapidly creating a glass. Their viscosity at the melting point is also lower. These liquids are far more difficult to turn into glass. In order to account for the metallic glasses that don't conform to Arrhenius law, Angell [15] modification of the Vogel-Fulcher-Tammann (VFT) equation 9 can be used. In this equation a fragility factor (D^*) compensates for the non-Arrhenius behaviour in fragile liquids. If $D^* = \infty$ a liquid does follow the Arrhenius, for $D^* = 100$ the liquid is still strong, and for $D^* = 2$ a liquid is considered fragile [9]. η is the viscosity, η_0 is the high temperature limit of the viscosity, T is temperature, and T_0 is the temperature at which the barrier to viscous flow becomes infinite. In figure 15 a plot of the temperature dependency of viscosity according to Angells equation can be seen. In this figure various liquids with different fragility are plotted.

$$\tau = \tau_0 \exp\left(\frac{E}{k_B - T}\right) \tag{8}$$

$$\eta = \eta_0 \exp\left(\frac{D^* T_0}{T - T_0}\right) \tag{9}$$

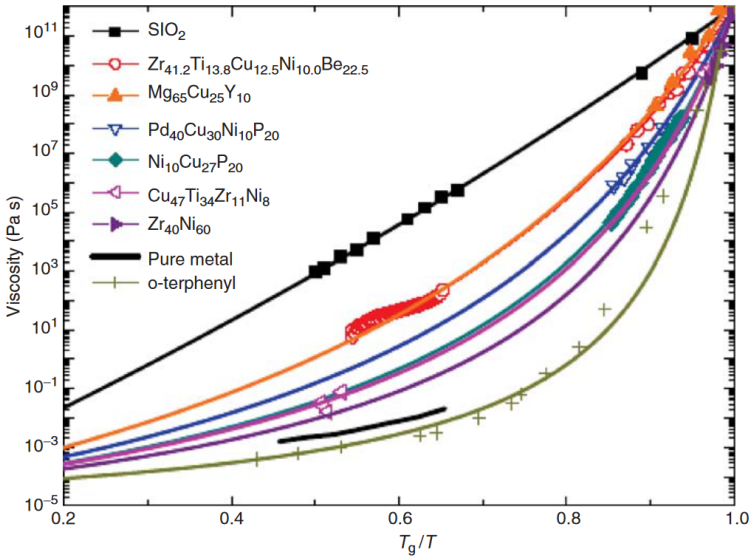

Fig. 15: Temperature dependency of viscosity. From Busch et al. [15]

D. Nanocrystalline Metals

Nanocrystalline metals are composed of grains in the nanometer range. These material have unique properties because more than 50% of the atoms in the material can exist in a defect structure instead of the bulk material [51]. Therefore the poperties of the grain boundary are of great influence on the overall properties of the material. These grains can range in size from a few nanometers to hundreds of nanometers, but are smaller then one micrometer [18].

There are two different ways to create nanocrystalline materials by melt spinning, direct and indirect. In the direct method an alloy is chosen with a high nucleation rate and slow crystal growth. This combination ensures the creation of as many crystals as possible. The high cooling rate and nucleation rate prevents the grains from growing too large. The indirect way of creating nanocrystalline metal is to start with an amorphous metal. A thermal treatment will cause highly controlled nucleation in the amorphous structure [17]. The grain size can be controlled by the temperature and time at which the metal is annealed. Another benefit is the homogeneity of the created structure, compared to that of directly melt spun material, which often has a gradient in the grain size distribution. This way also composites of amorphous and nanocrystalline materials can be made [17].

Just like amorphous metals, nanocrystalline metals have a high degree of disorder, and a corresponding free energy. The free energy is proportional to the inverse of the grain size, meaning that smaller grains have a higher free energy. The amount of free energy is comparable to that of the amorphous metal, however it doesn't exhibit the same metastability in regards to crystallization [52]. Nanocrystalline materials are unstable, the crystallized grains will keep growing under normal circumstances. Aided by high diffusivity due to the many grain boundaries, grain sizes can double within a matter of weeks at room temperature [53]. The driving force behind this growth is the interfacial free energy of the grains. This energy normally scales with the inverse of the grain size, however at small scales this starts to deviate. Free energy increases less fast with decreased grain size due to a decrease in specific grain boundary enthalpy at this scale [52].

But when grain growth is prevented, nanocrystalline metals can exist in a metastable state. Preventing grain growth can be done by alloying. These alloys should have a large enthalpy of grain boundary segregation, reducing the Gibbs free energy in the boundary to zero. In these alloys an equilibrium is reached between solute atoms in the lattice and atoms on the boundary. If it is energetically preferred to be on the boundary, atoms will transfer from lattice to the boundary, to minimize free energy. Another way to minimize the free energy is to reduce the boundary sites by grain growth. At a certain point the amount of free grain boundary site is reduced to zero, and atoms have to dissolve back into the lattice. For this to take place enthalpy has to be provided, and interfacial energy is increased. When these are in balance grain growth will stop and the metal is stable/metastable. Stability can persist at elevated temperatures. So to stabilize nanocrystalline materials, elements with large enthalpy of segregation can be added [52].

E. Nanocrystalline Properties

The smaller the grains become, the more the grain boundary structure plays a role in the properties of the material. A larger percentage of atoms are part of a defect structure instead of a bulk crystal structure. This can range from 3% for grains with a size of 100 nm to 50% for grains with a size of 5 nm [17]. Large stresses and strains are present in the material. The strain created by the grain boundary is present in the whole grain because of its small size. The density of the material decreases due to the extra space between the misaligned crystals as compared to the perfect crystal lattice. A nanocrystalline structure is far from the equilibrium composition due to all the energy stored in the grain boundaries. Research on the properties of nanocrystalline materials has been compiled by Gleiter [53], Gusev and Remper [54], and more recently by Wilde et al [18].

The mechanical properties of nanocrystalline metal are the result of the low amount of bulk material and high amount of boundaries, triple points, impurities and defect. These cause high levels of internal stress and energy in the material. The elastic modulus of nanocrystalline metals can be lowered by 50% for gains with a size of 5 nm, compared to that of conventional metals [55]. Due to the increased free volume and grain boundaries in nanocrystalline metals, more atom are further away from each other. The interatomic potential between these atom is lower than that of the atom in the bulk of the crystal. This results in a lower elastic and shear moduli in the grain boundary [54]. Averaging this effect over the whole material gives a decreased elastic modulus.

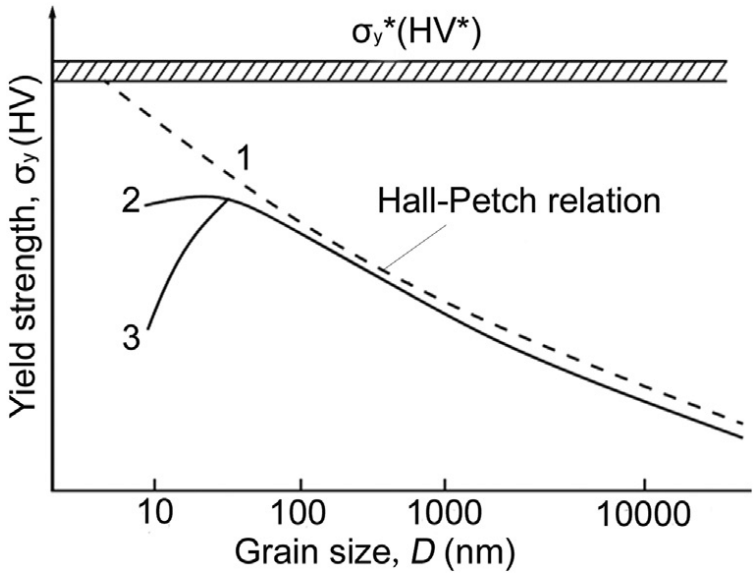

Fig. 16: Yield strength dependence on grain size. [16]

Plastic deformation in nanocrystalline materials does not come from dislocation movement in the crystal. There are very little dislocation present in the grains, and if they are present and mobile they are easily moved out of the grain, to the boundary. Below 9 nm grain size there are no dislocation present [55]. This greatly changes the plasticity of the material. The plastic deformation process, shifts from being dislocation motions dominated to being highly influenced by grain boundary movement [56]. Normally in crystalline metals, decreasing grain size increases the strength. This is known as the Hall-Petch relation.

$$\sigma_y = \sigma_0 + k \cdot d^{\frac{1}{2}} \tag{10}$$

The Hall-Petch equation states the relation between the yield point and the grain size as in equation 10. In this equation σ_y is the yield stress, σ_0 the stress at which dislocation movement starts, k the strengthening constant, and d the grain size. σ_0 and k are both material properties. However at very small grains this relationship breaks down, and can even reverse. The theoretical maximum is not reached and strength and hardness will decrease. The relation between grain size and yield strenght can be seen figure 16. The Hall-Petch relation breaks down because it is based on dislocation movements as primary process. The discrepancy starts when the grain size and dislocation spacing become similar. This can be as soon as 50 nm depending on the alloy [18]. At these sizes, plasticity can be accommodated by emission of dislocations and the creation of deformation twins. Reducing to even smaller grains and the process will mainly be grain boundary sliding. Grain boundary sliding happens where multiple similarly oriented grains have a common grain boundary along the principle stress axis. This provides less resistance to movement compared to dislocation movement, therefore increasing plasticity. Decreasing grain size further will therefore not make the material any stronger, but will increase the opportunity for grain boundary sliding and therefore make it weaker. Leading to a negative Hall-Petch relation.

During grain boundary sliding, not all boundary segments will move with the same speed due to the different orientations along the grains. This is a disruption of the common grain boundary (making is somewhat less weak). Movement of the grain boundaries and orientations changes of the grains during plastic deformation give rise to grain growth. Grains will rotate to align with neighbouring grains, and grain boundaries will disappear leading to one long grain. [57] If the grains are in the 100 nm size range, both mechanisms for deformations can occur and interact. In grains this size a significant number of dislocations can exist, but they are small enough to allow for grain boundary sliding and grain rotation. Plastic deformations in such structure causes grains to have a work hardened outer layer, giving rise to high strength materials with increased ductility. Mechanical properties of these materials are described by the core-and-mantle model [18].

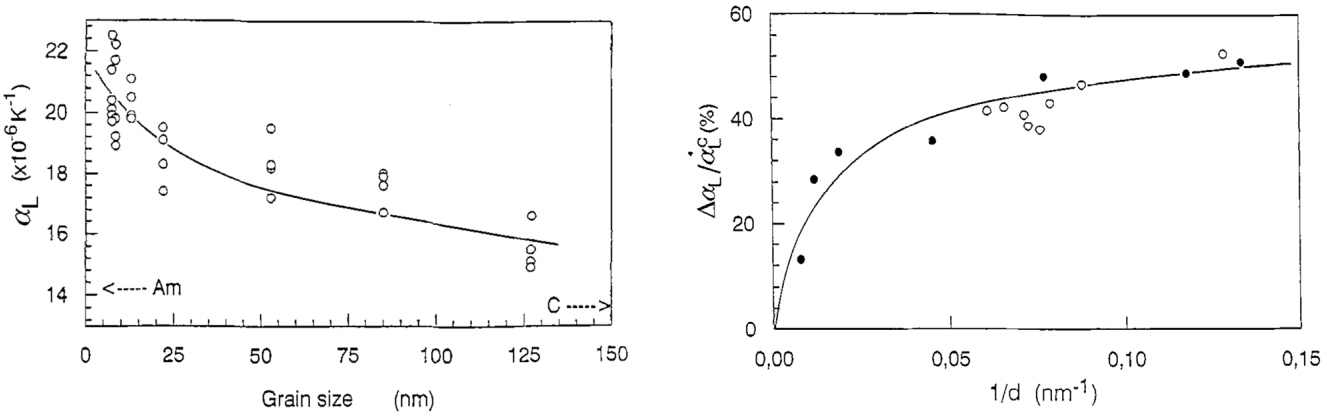

(a) Effect of grain size on the thermal expansion coefficient

(b) Relative thermal expansion coefficient change with grain size

Fig. 17: Figures from Lu et al. [17]

The thermal expansion coefficient of nanocrystalline materials is generally higher than their amorphous or macro crystalline counterparts. Grain boundary regions take up a large percent of the volume of the materials. The boundary regions expands differently than the bulk crystal. The effect of the boundary can be four times larger than that of the crystal [53]. This is because there is more free volume present in this region. The total thermal expansion coefficient is combination of the coefficient of the bulk crystal and of the boundary region, and can be expressed according to equation 11. Therefore the thermal expansion coefficient is dependent on the ratio between grain boundary region and bulk crystal, or grain size. This can be seen in figure 17a. Where α_i and α_c are the respective expansion coefficients and F_i is the volume fraction of interfaces which is dependent on the grain size. From this it is expected to find a linear relation between $\Delta\alpha$ and the grain size. Since the thermal expansion coefficient of both the bulk and the boundary should not change with grain size. However experiments show that this is not the case. Meaning that $\Delta\alpha$ does change with grain size. This can be seen in figure 17b from Lu et al. [17]. In this figure $\frac{\Delta\alpha}{\alpha_c}$ is plotted against $\frac{1}{d}$ where $\Delta\alpha = \alpha_i - \alpha_c$. This plot should yield a straight line, if both coefficients would not change with grain size. It can be the bulk, the boundary or both coefficient that are changing. Both phenomena can be explained, firstly the boundary: when the grain size decreases the structure of the boundary changes, smaller boundaries have less free volume leading to a decreased coefficient of expansion. Secondly the bulk material gets dilated, stretched, leading to an increase in expansion coefficient.

$$\alpha_n = F_i\alpha_i(1 - F_i)\alpha_c \tag{11}$$

The high dependence of the CTE on grain size means that thermal expansion can be tuned by the size the grains. The grain size in turn can be tuned by heat treatment. This would make is possible to match the thermal expansion of two different materials or parts, without changing the composition of the material by giving the right heat treatment.

Diffusion plays a large role in multiple processes concerning the structure change and stability of nanocrystalline materials, such as grain growth and the interatomic interaction potential. In return the diffusivity is highly dependent on the structure of the material. This makes diffusion an important parameter in nanocrystalline materials. Diffusion in nanocrystalline materials is high, due to the high density of grain boundaries, which are the main pathways of diffusion in crystalline materials. Diffusion rates in nanocrystalline copper can be up to 20 orders of magnitude higher than lattice diffusion and up to 4 orders of magnitude higher than grain boundary diffusion in copper [53]. Diffusion in nanocrystalline materials seems to behave similarly to that in conventional metals. However due to the small grains, vacancies and defects are more easily reached in the bulk material. Diffusion can follow an hierarchical pathway, first trough the boundaries between nanocrystalline clusters, after which the atoms move between the nanocrystals themselves, to finally end up in a crystal. This phenomena is mapped using radioactive tracer atoms, and can be seen schematically in figure 18. Grain boundary diffusion is heavily dependent on the structure of the boundary. The structure of the grain boundary dictates the energy barrier for atoms to move through the boundary. This dependence is exponential, so it can change rapidly with structural changes. Depending on the temperature, the mechanism of diffusion changes from being dominated by the grain boundary diffusion at low temperatures to homogeneous diffusion at high temperatures [18]. During high temperature diffusion, micro structural changes take place such as grain boundary migration. This changes the penetration in relation to depth profile, from exponential decreasing to a linear one [18]. If the origin of the nanocrystalline metal is an amorphous metal, then there is a possibility for amorphous structure to be present in the grain boundary, hindering diffusion. In this case diffusivity is much lower than normally expected from a nanocrystalline metal [18].

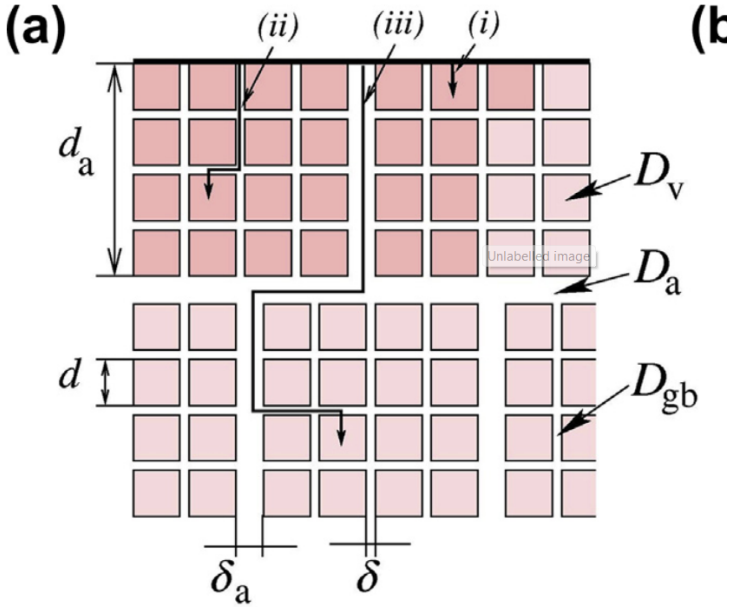

Fig. 18: Schematic of diffusion paths in nanocrystalline material. i direct, ii hierarchical iii inter boundary. From Wilde et al. [18]

III. Aluminium Silicon Alloy

Aluminium silicon (AlSi) alloy is a material commonly used for casting. It is the preferred material for engine components such as the blocks and rods, and aerospace parts. Properties such as good castability, high strength and light weight make is suitable for these applications. These alloys are classified by the Aluminium Association as: $4xx.x$ for AlSi binary alloy and $3xx.x$ for AlSi with magnesium or copper additives. These alloys have a typical silicon content for 5 to 23 $wt\%$ [20]. The eutectic composition for a pure binary AlSi alloy is 12.6 $wt\%$ as can be seen in the phase diagram plotted in figure 19. Depending on the composition, the microstructure can be described as an eutectic mixture of alternating aluminium and silicon structures in an α-aluminium matrix for a hypoeutectic mixture [58], a fully eutectic mixture, or an eutectic mixture with Si precipitates for a hypereutectic mixture [35]. Micrographs for these different mixtures are presented in figure 20.

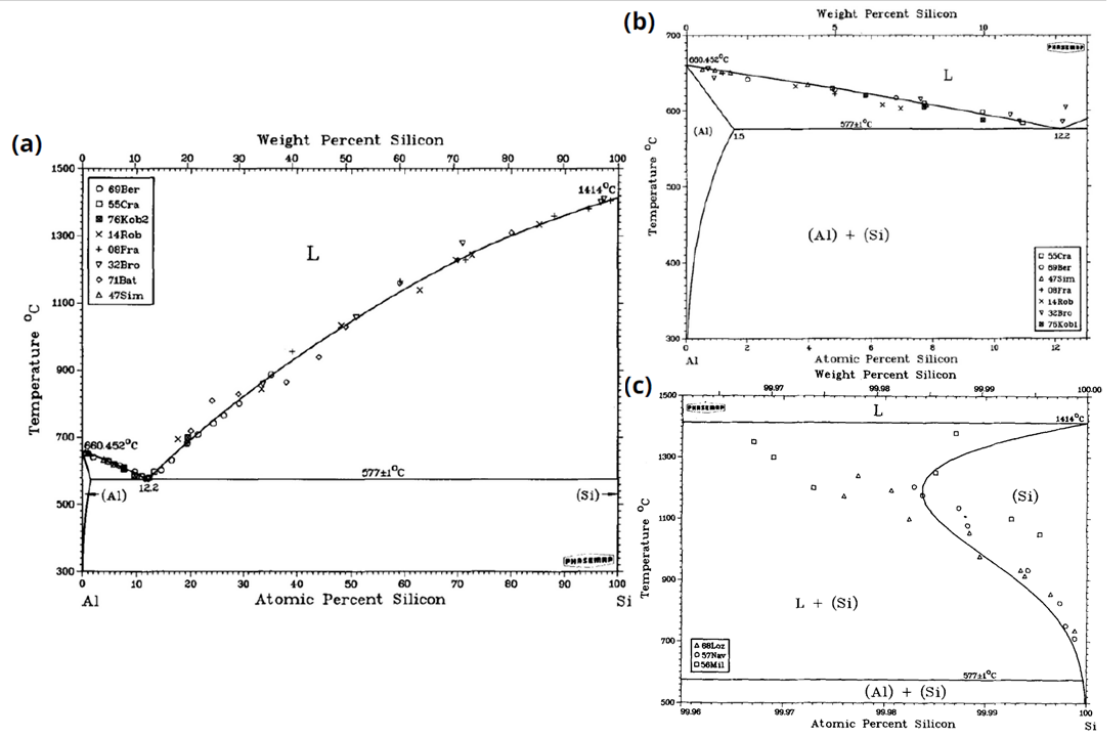

Fig. 19: Phase diagram of binary allow AlSi. (a): overview, (b): detail high weight fraction Al (c) detail high weight fraction Si. From Murray et al. [19]

Silicon improves the strength of the alloy by replacing some of the aluminium atoms in the α-aluminium matrix. This introduces stress and strain in the lattice, hindering the movement of dislocations. Furthermore the silicon crystal structure present in the eutectic, harden the relatively soft α-aluminium matrix [20]. With an increasing silicon content, Si precipitates form which increase the specific stiffness and and decrease the coefficient of thermal expansion [43]. However under slow solidification rates and high silicon content, silicon precipitates can become increasingly large (in the range of 100 μm), compromising the properties of the alloy. This is the case for hypereutectic AlSi alloys which can have a silicon content up to 60 $wt\%$ [21].

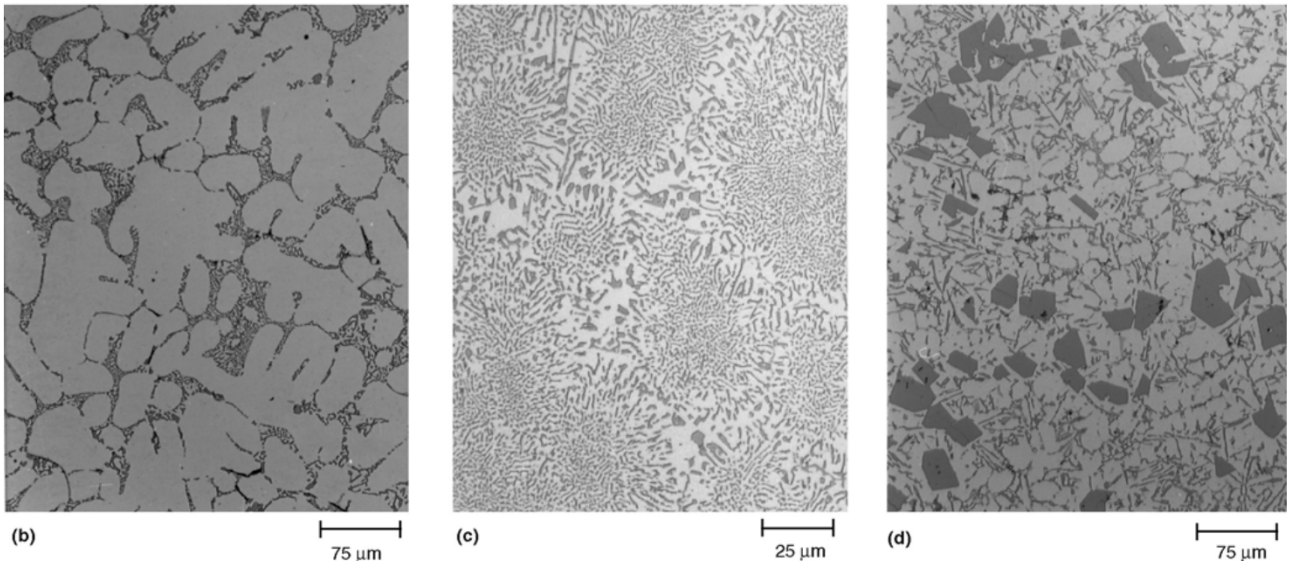

Fig. 20: Micrographs of AlSi alloy with increasing amounts of Si. (a) $< 12.6wt\%$ (b) $12.6wt\%$ (c) $> 12.6wt\%$ From Warmuzek et al. [20]

A. *Hypereutectic*

In an hypereutectic AlSi alloy, Si particles solidify first. Around the particles a zone depleted of Si will solidify as α-aluminium. after which the eutectic mixture of alternating Si and Al will solidify. An example of this can be seen in the work of Abboud et al. [21] in figure 21. This size of the Si particles is dependent on the solidification rate, increasing the rate will decrease the particle size. The eutectic mixture will be able to solidify earlier hindering the growth of the Si particle. Another effect of the increase in solidification rate is an increase of the solubility of Si in the α-aluminium matrix, and that the eutectic point moves to a higher $wt\%$ Si. Furthermore, the microstructure of the eutectic phase changes. Under normal cooling condition the eutectic grows rod, or plate like structures. When solidification is increased the Si starts to form flakes. Increasing even further and the Si becomes fibrous or dendritic in nature [59] [21]. The change in morphology can be explained by the growth mechanism of the Si crystals. The exact nature of this mechanism is unclear, with contradicting explanations present in literature. One of the growth mechanisms of the Si phase is the twin plane re-entrant edge (TPRE) mechanism. At lower growth rates this is the preferred growth method and produces highly twinned anisotropic structures. Twinning aides solidification by providing sides for attachment on an closed packed crystal face [60]. For Si grain refinement, sodium or other impurities can be added to promote twin growth in Si [61]. Si can go from flaky to fibrous without changing cooling rate. As a consequence these fibres are highly twinned. The same fibrous structure can be created without sodium modification but with high cooling rates. These fibres are isotropic and are not twinned [59]. Twinning in fibrous Si can therefore be an indication of growth facilitated by impurities rather than high cooling rates. However Abboud et al. [35] observe twinned fibre like Si structure without the use of modifying impurities reported, but do explain the fibrous structure as a result of the TPRE-mechanism.

Multiple efforts to quantify the relation between cooling rate and microstructure have been made. One of those methods is to measure the distance between the arms present on aluminium dendrites. This is called the secondary dendrite arm spacing (SDAS). When combined with thermodynamic modeling, insight can be gained on the cooling rate experienced by the material [62]. Equation 12 fits the dendritic arm spacing D with cooling rate ν using constant β and exponent n depending on the alloy. β has a value between 40 and 90 and the exponent lies between 0.55 and 0.25 [63] [64]. The dendritic arm spacing has a big influence on the mechanical properties of the alloy. With smaller arm spacing leading to increased strength. The SDAS has a strong linear correlation with the Hall-Petch relationship [65].

$$D = \beta \nu^{-n} \tag{12}$$

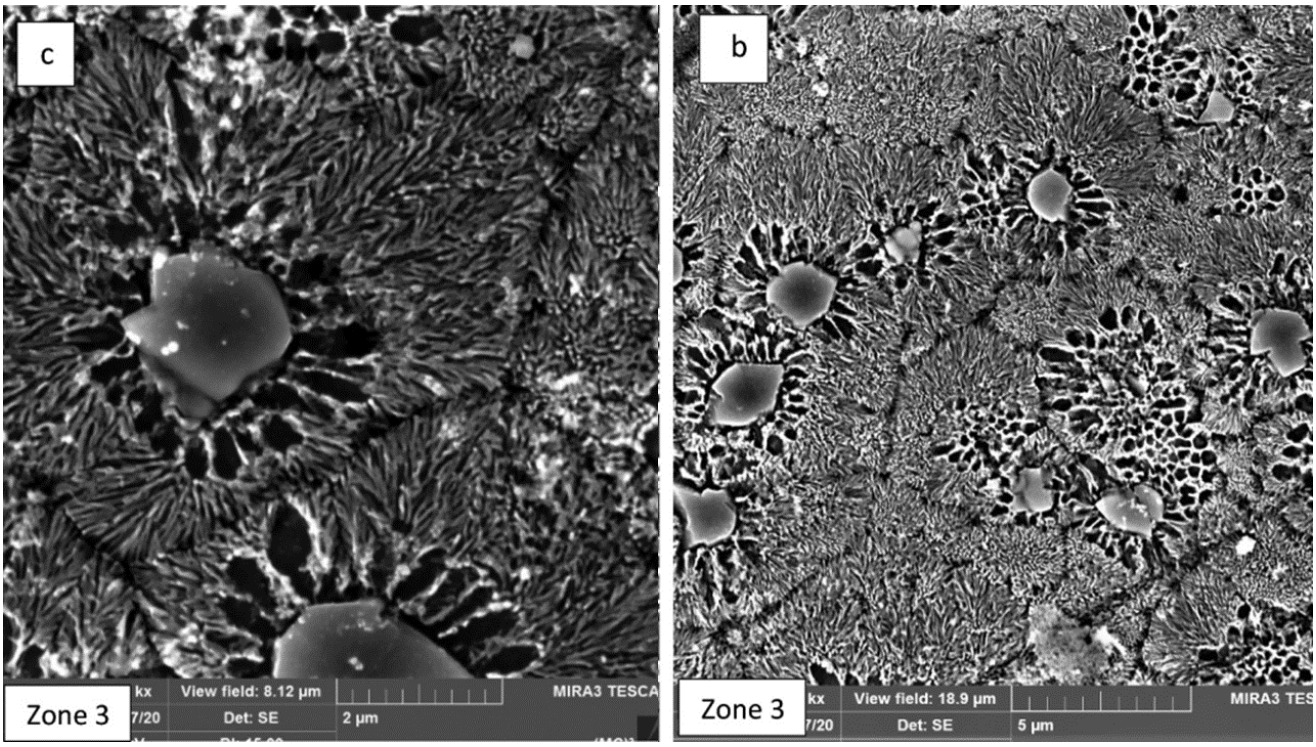

Fig. 21: SEM image of Si particles in a eutectic mixture from Abboud et al. [21]

A common way to examine cooling rate and microstructure, is to use laser remelting on the surface of bulk material. This way, cooling rate of up to $10^7\ Ks^{-1}$ can be achieved achieved [35]. Cooling rates can be adjusted by laser power and the speed with which it moves over the surface. The surface is then analysed by optical and electronic microscopy, diffraction studies and mechanical tests, in order to link material properties to microstructures and solidification rates. Si morphology at different cooling rates can then be categorised. In table I results of such categorisation is printed.

Sample no.	Laser power W	Scanning speed, mm /s	Melted depth, mm	Si morphology	Average cooling rate, °C/s [24]	λ, nm
A#1	2,500	5	3	Flakes, feathery and fibrous	6×10^3	50–100
A#2	1,800	10	0.5	Broad, flaky	3×10^4	30–50
A#3	1,800	25	0.3	Chain like and fibrous	1×10^5	30
A#4	2,500	100	0.16	Elongated flake, Fibrous, and agglomerated rounded particles	1×10^6	20
B#1	2,500	5	3	Mixed fibrous and flakes	1×10^5	30
B#2	2,500	50	0.45	Y, chain like and thread like fibrous	1×10^6	20
B#3	2,500	100	0.25	Chain like and thread like fibrous	3×10^6	10

TABLE I: Results from Abboud et al. [35]

B. AlSi40

A typical alloy cast by RSP in Delfzijl is the AlSi40 alloy, which contains 40 $wt\%$ Si. To get an idea of the microstructure likely present in this material, multiple studies of rapidly cooled AlSi alloys with varying silicon content and cooling speed are compared. For AlSi20 the effect of increasing the cooling rate from 10^3 Ks^{-1} to 10^6 Ks^{-1} resulted in a decrease of interlamellar spacing from 10^4 to 10^1 nm, and the SDAS from 3 to 0.5 μm. The structure of the Si changed from needle like, to rounded off shapes. Microhardness was increased 3 times by the decreases interlamellar spacing. The solubility of Si in Al was increased from 0.5% to 5% [35]. For AlSi50 and AlSi60, a similar study has been carried out. At high cooling rates fine silicon crystals are present in a matrix of dendritic eutectic structure. Increased cooling rates, decreased the size of the silicon grains, and dendritic arm spacing. Hardness was increased as well with decreasing laminar spacing. Si particle growth is stopped by the nucleation of the highly enriched Al phase. Particles stay smaller the sooner this phase can nucleate [21]. In a study on an AlSi13 alloy modified with copper [63], solidification rates from standard casting to melt spinning were investigated. The cooling rate is increased tenfold each iteration, with a maximum of $1.5 \cdot 10^5$ Ks^{-1} during melt spinning. This resulted in an ever increasing refinement of the microstructure, and silicon phase changing from needle like to spherical. At maximum cooling rate, the Al phase grows so fast that the second phase is distributed around the Al grains. The second phase didn't have enough time to form a large phase and was therefore nanocrystalline. Al content in this boundary phase is to high to become amorphous. SDAS had decreased 10 fold over the cooling rate range. During mechanical testing is was found that hardness of the alloy had increased 2.5 times. The expected microstructure of the AlSi40 alloy will be a combination of the data found in literature. The cooling rate is not exactly known but will be in the order of 10^5 to 10^6 Ks^{-1} typical for the melt spinning process. The microstructure will most likely consists of a dendritic phase and Si precipitates, with a high amount of grain refinement. Size of the Si precipitates is expected to be smaller than the 2-5 μm range found for the 50 $wt\%$ Si alloy. Laminar spacing is expected to stay the same. Two results that lie very close to the AlSi40 made at RSP Delfzijl, are the AlSi35 sample by Abboud et al. [21], cooled at $9.5 \cdot 10^5$ Ks^{-1}, and the AlSi40 sample from Mueller et al. [43] produced by selective laser melting. Both microstructures are presented in figure 22.

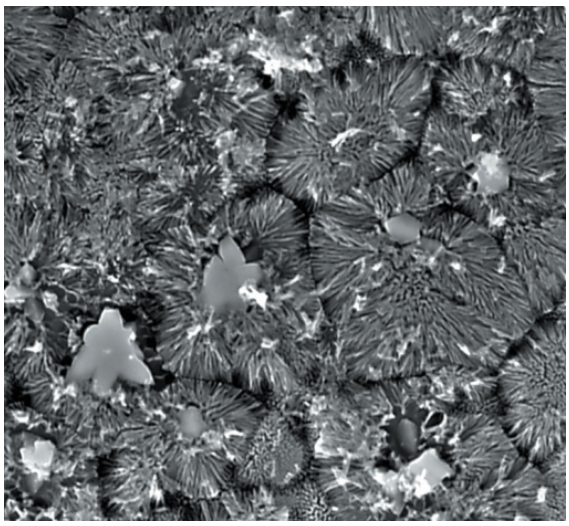

(a) SEM image of a AlSi35 sample cooled at $9.5 \cdot 10^5 K/s$. From Abboud et al. [21]

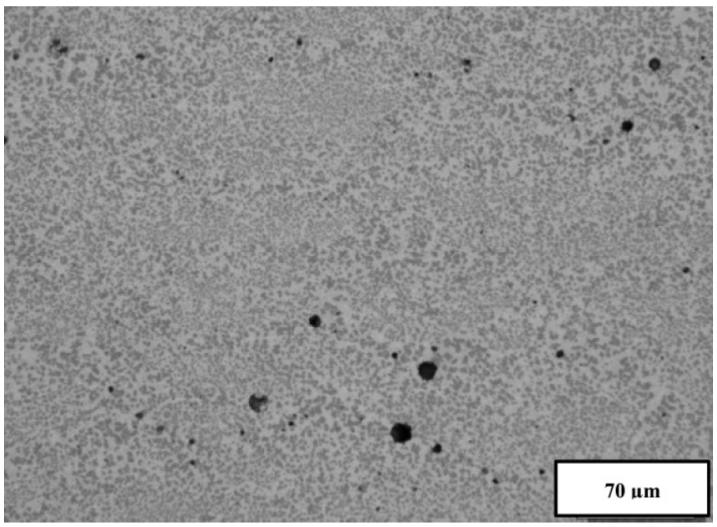

(b) Optical microscopy image of an AlSi40 sample produces using selective laser melting. From Mueller et al [43]

Fig. 22: Two samples produced under similar conditions as present at RSP Delfzijl

IV. Research methods

To investigate the microstructure of rapidly solidified metals, multiple methods are available. Due to the scale at which these structures exists, optical microscopy is no longer sufficient. Electron microscopy, diffraction, and thermoanalytical techniques are able to provide information at these scales. In combination with simulation a detailed analysis of the microstructure can be made.

A. Simulations

Their are multiple ways to investigate and or predict the atomic structure of metals. For near equilibrium systems, commercial software such as Thermo-Calc [66] is able to predict phase composition, given a specified alloy and cooling rate. Thermo-Calc uses databases with experimental results and phase diagrams to make these calculations. For systems that are far from equilibrium such results are not available. To predict atomic structures for rapidly solidified metals such as nano crystalline or amorphous, molecular dynamics simulations can be made [67] [68] [69] [70]. These types of simulations, calculate atomic positions in time using fundamental equations. Interatomic potentials are used to calculate position, velocity, and acceleration each timestep. The interatomic potential is a simplified model of all the forces interacting with the atom [71], which are the result of quantum mechanical principles. An accurate model of the interatomic potential is therefore crucial for an accurate prediction of the resulting microstructure. In figure 23 the result of a molecular dynamics simulation is presented.

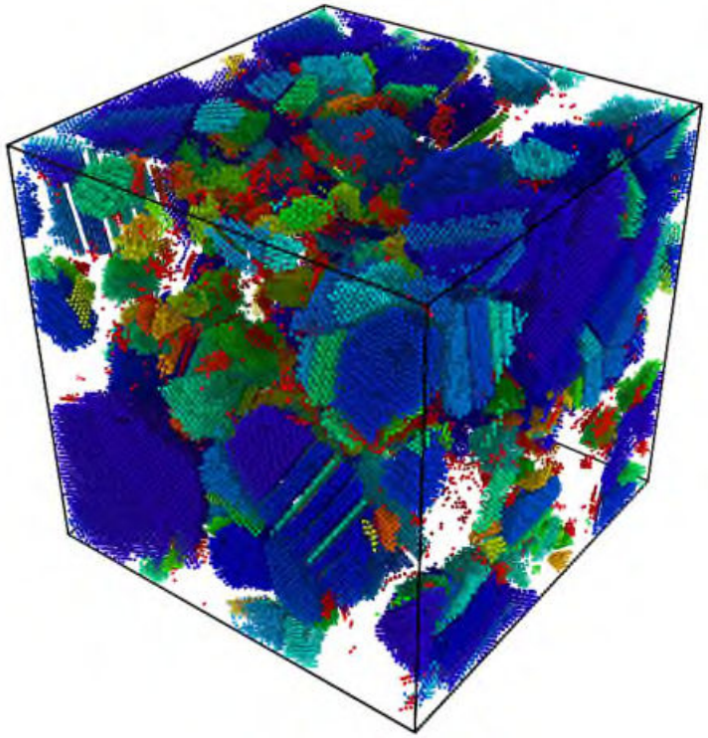

Fig. 23: Result from and molecular dynamics simulation of the solidification of pure aluminium with a cooling rate of 1 Ks^{-1} at 507 K. From Papanikolaou et al. [22]

B. XRD

In order to verify the results from the simulations, an X-ray diffraction (XRD) measurement can be made. Such a measurement uses X-ray radiation to extract information out of the material concerning its crystallinity or other repeating structures. This information is gathered via the Braggs diffraction process in which X-rays reflect of the atoms. If there is crystallinity the X-rays can extinguish or amplify each other, depending on the wavelength and crystal lattice spacing. With a non random structure outgoing rays will have an intensity dependent on the angle and wavelength of the incoming rays. If the structure is completely random there will be no effect with a change in angle or wavelength. An amorphous microstructure will show a diffuse and spread out diffraction pattern, compared to a pattern with sharp peaks for a crystalline microstructure [14].

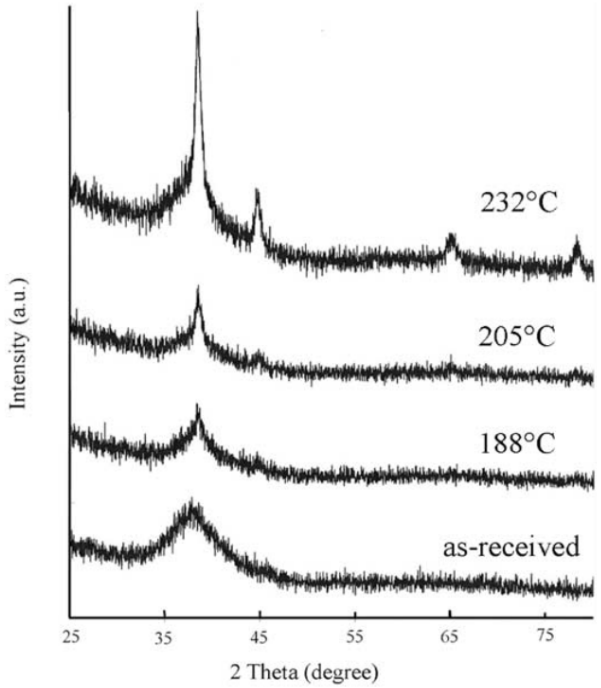

(a) XRD result from an initially amorphous $Al_{87}Ni_7Gd_6$ ribbon annealed for 30 min at 188, 205, and 232 $°C$

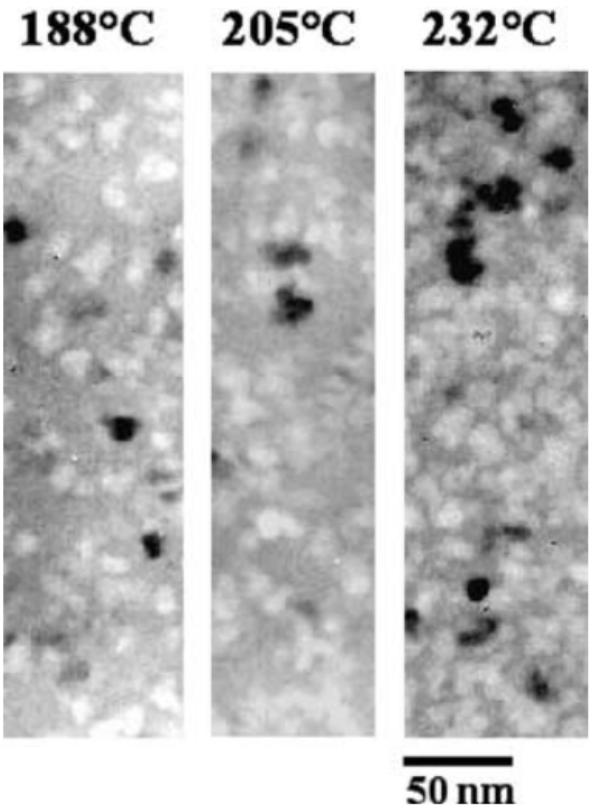

(b) XRD result from an initially amorphous $Al_{87}Ni_7Gd_6$ ribbon annealed for 30 min at 188, 205, and 232 $°C$

Fig. 24: Results from Wesseling et al. [23]

C. SEM

Further analysis can be done using scanning electron microscopy (SEM), and (high resolution) transmission electron microscopy (HRTEM). SEM can be used for measuring and quantifying grain size and distribution throughout a sample, with resolution up to a few nm. With HRTEM it is possible to see individual atoms and distinguish between nanocrystalline and amorphous structures. Wesseling et al. [23] compares amorphous ribbons, annealed at different temperatures using XRD and TEM imaging, to find out the volume fraction of nanocrystalline phase at these different annealing temperature. The results in figure 24 show how the TEM images; figure 24b. correspond to the XRD measurements; figure 24a.

D. DSC

Finally, differential scanning calorimetry (DSC) or differential thermal analysis (DTA) can be used to measure the glass transition temperature, melting temperature and crystallization temperature [55]. With these measurements information about particle size and crystallization fraction can be deduced. Smaller particles have increased interfacial energy, and amorphous samples will crystallize, both effects can be seen in a DSC measurement. For example a DSC plot in figure 25 of a metallic glass can be seen.

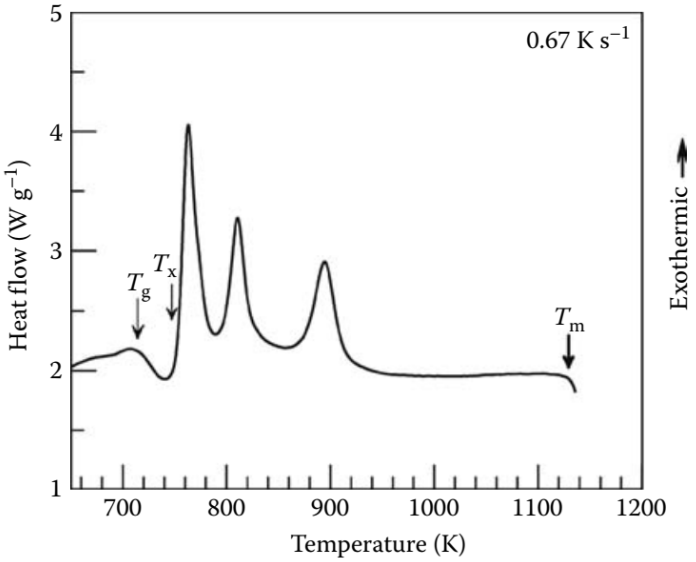

Fig. 25: Schematic DSC plot of a metalic glass, at 40 $K\ min^{-1}$. In which T_g, T_x, and T_m are the glass transitions, crystalization, and melting temperature respectively. From Suryanarayana et al. [14]

V. Process

The planar flow casting (PFC) process is a combination of thermodynamic, fluid mechanical and solidification processes. Interaction between these processes make a complete mathematical description challenging. Performing a successful cast and optimizing the results, requires a link between the input parameters, material parameters and the resulting ribbon. These parameters [36] can be found in table II. To find this link, a combination of simulations, analytical solutions and empirical data can be used. This is combined with experimental castings on the test machine to verify the found solutions.

TABLE II: Variables of the planar flow casting process from Su et al. [36]

Parameter	Description
U	Wheel speed - To be controlled
G	Gap between the wheel and nozzle - To be controlled
P	Pressure - To be controlled
B	Nozzle slot - To be controlled
W	Nozzle width
T	Ribbon thickness
T_j	Crucible temperature
T_w	Wheel temperature
q	Metal density
η	Viscosity
σ	Surface tension
C_p	Specific heat
T_m	Melting temperature
ΔH_f	Latent heat of fusion
k	Heat conductivity

The first step is to understand the underlying physics of the different processes. Therefore a review of existing literature focused on the melt spinning process is done. In order to simplify the problem the thermodynamic, fluid mechanical and solidification processes are treated separately. This is a valid approach according to Carpenter et al. [31] because the heat transfer and fluid flow are weakly coupled. Aside from Carpenter, important work on the PFC process has been done by Steen [72] and his research group [73] [74].

A. Fluid Mechanics

The fluid mechanics of melt spinning have been studied by multiple different groups. These studies focus on area such as: stability, parameter space, analytical solutions, and simulations. A short problem description of the fluid mechanics of melt spinning is as follows: liquid metal flows by metallostatic or external pressure, through a high aspect ratio nozzle, onto a moving substrate situated less then a millimeter from the nozzle. The fluid is kept on top of the wheel when the outflow pressure is in balance with the capillary pressure, dynamic pressure and pressure losses due to friction and turbulence. The capillary pressure is created by the surface tension of the liquid that is held between the nozzle and wheel surface. The dynamic pressure is the kinetic energy of the moving fluid. This movement causes losses in the system. Firstly the flow is redirected from vertical to horizontal, creating vortices in which momentum is lost. Secondly a boundary layer is created on all the surfaces in contact with the liquid, momentum is lost here as well.

If the system is not balanced, there will be either no flow or too much flow. There is no flow when the pressure is too low to overcome the capillary forces that restrict the flow through the gap. When the pressure is too high the capillary force is not able to restrict the flow in the upward section of the puddle, and therefore liquid will spill out the back of the apparatus. This can also occur when the substrate speed is too low, reducing the pressure loss in the upward section of the puddle. When the substrate speed is too high the liquid will not have time to solidify, this is not a fluid mechanical boundary however.

The relevant parameters of this process are of importance for a better understanding of the process and the ability to give predictions about the geometry of the produced ribbon. Fiedler et al. [75] writes that pressure, nozzle geometry, gap size, and melt overheat are the main parameters which influence the geometry of the created ribbon. This resulted in equation 13 for the prediction of the ribbon thickness. In which d is the ribbon thickness K a factor combining the nozzle slot breadth, gap, melt overheat, viscosity and surface tension. a_n is the nozzle slot breadth, v_s is the wheel speed, p is the ejection pressure.

$$d = K\frac{a_n}{v_s}\left(\frac{2p}{\rho}\right)^{\frac{1}{2}} \tag{13}$$

In contrast Yu [76] wrote that the gap size doesn't have a lot of influence at all, and that the ribbon thickness is mainly attributed to the wheel speed in combination with nozzle geometry. In the conclusion however, this is expanded to "nozzle passage flow resistance". In this case, if the gap becomes small enough to have an significant effect on the flow resistance, it become an influence on the ribbon thickness.

Further refinement to these results have been made by Anestiev et al. [24] They modeled three different outflow modes dependent on the ratio of the boundary layer to the gap height and if the volumetric flow rate is equal or larger than the substrate velocity as seen in figure 26. The outflow mode determines the equation to use for the losses caused by the direction change of the fluid. It refines the (loss) factor K introduced by Fiedler et al. [75].

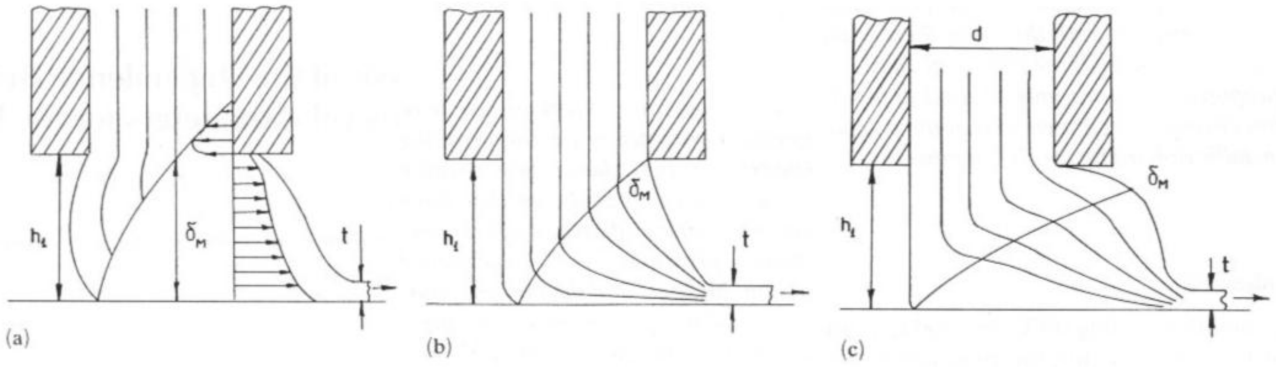

Fig. 26: Three different outflow modes as presented by Anestiev et al. [24] In which h_f (Gap height) is either smaller (a) or larger (b) than δ_M (boundary layer), and when the flow rate is larger than the substrate velocity (c).

Further improvements were made by Sung et al. [25] who worked out the effect of the gap on the friction loss factor in more detail. This can be seen in figure 27.

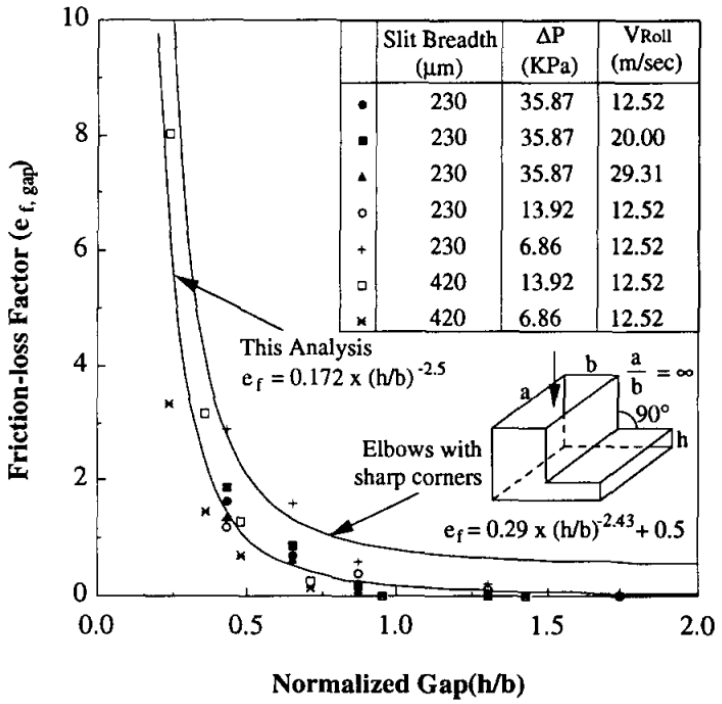

Fig. 27: Effect of the gap on the friction loss factor as presented by Sung et al. [25]

Experimental work has also been carried out. Wilde et al. [34] investigated the effect of mass flow, gap height, and wheel speed on the melt puddle characteristics. In their experimental setup, a high speed camera was used to capture the size and shape of the melt puddle during operation. Parameters such as over pressure, wheel speed, and gap size were computer controlled. They found increasing mass flow rates leading to instabilities of the puddle, causing defects in the produced ribbon. It also caused the menisci to move further away from the ejection slit, when compared to a casting with a lower mass flow. Furthermore the downstream meniscus became more shallow.

A decrease of the gap height had a similar effect on the meniscus position as increasing the mass flow had. In both cases the downstream meniscus reached a maximum at the end of the nozzle, where it became pinned. It is suggested that the pinning of the meniscus at the nozzle edge, has a stabilizing effect on the melt puddle.

Counterintuitively, with increasing wheel speed the meniscus moves upstream and the puddle becomes shorter. This phenomenon can not be fully attributed to the changing wheel speed however, because the wheel speed could not be controlled independently from the mass flow rate parameter.

The upstream meniscus didn't show as much variation as the downstream meniscus. It also didn't seem to have an effect on the stability of the puddle. Possible emerging effects with the upstream meniscus have to do with gas entrapment at low pressure, this is however not further investigated in this study.

Another experimental study was carried out by Praisner et al. [26]. Apart from over pressure and wheel speed, the effect of melt overheat was studied. Praisner et al. argued that an increase in pressure and therefore mass flow, causes the ribbon to leave the wheel earlier, due to the increased mass of the ribbon. Furthermore as presented in figure 28, Praisner et al. show that the amount of overheat has two effects on the ribbon thickness. At first the thickness decreases, this is explained by a decrease in solidification rate and heat extraction in the boundary layer. When overheat is increased further, ribbon thickness increases, due to an decrease in viscosity, allowing for more mass flow through the nozzle.

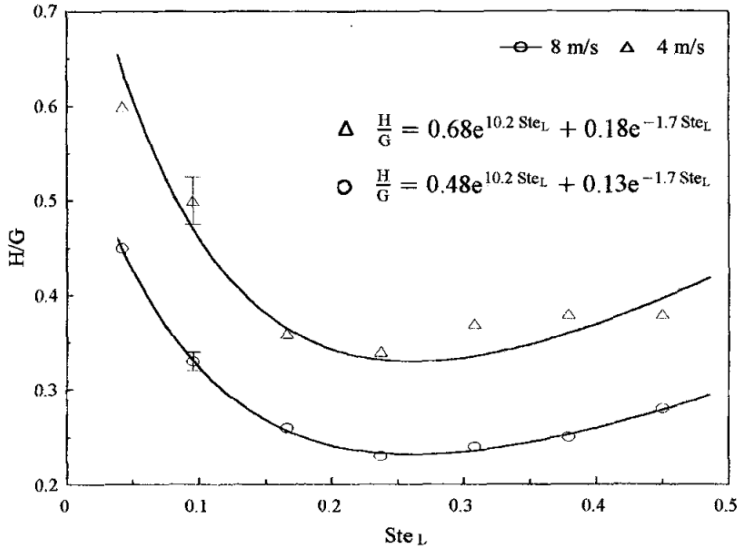

Fig. 10—Ribbon thickness *vs* Ste_L number for PFMS (P = 7 kPa, U_w = 4 and 8 ms^{-1}, G = 0.5 mm, and T_j = 195 °C to 310 °C).

Fig. 28: Effect of melt overheat as presented by Praisner et al. [26]. On the vertical axis the thickness divided by the nozzle wheel gap, and on the horizontal axis the melt overheat.

To get a better insight into the possible parameter combinations for a successful cast, Carpenter and Steen [27] introduced an operating window. They argued that the process is mainly dominated by pressure and inertial force due to the large Reynolds and Weber numbers. Therefore, they proposed an operating window in which the Weber number is plotted against the pressure index as can be seen in figure 29. In this window, each point on a straight line through the origin, representing a fixed ratio between pressure and inertial forces, results in the same ribbon geometry if these points fall within the operating limits. A different window exist for a chosen alloy and nozzle geometry. The operating limits are dictated by capillary forces and solidification speed. This window was then experimentally verified by casting ribbons with the same ratio between pressure and inertial forces.

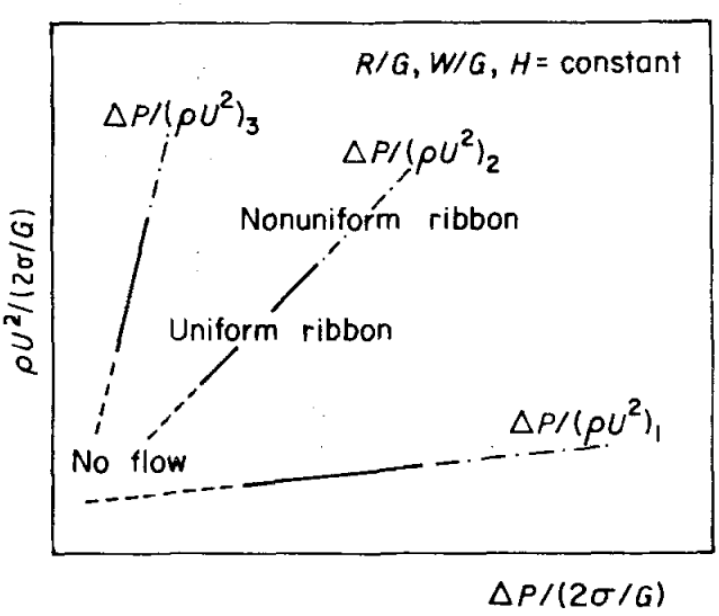

Fig. 29: Schematic operating window as presented by Carpenter and Steen [27]. On the vertical axis the inertial forces, and on the horizontal axis the pressure forces.

Byrne et al. [28] found solutions for the operating limits caused by capillary forces. This was done by calculating the pressure loss to the upstream meniscus. Depending on the pressure loss, the meniscus will be either stable or 'blow out'. If the pressure loss is too small, the capillary forces will not be able to hold the fluid in the gap, and casting will fail. The pressure loss is calculated similar to the pressure loss in a bending pipe, using a friction factor and dynamic pressure, as can be seen in equation 14.

$$P_{loss} = -\frac{1}{2} K \rho u^2 \tag{14}$$

These boundaries were then plotted in the operating window as seen in figure 30. Depending on the loss factor the boundary rotates around the origin of the plot. A loss factor between 1.8 and 2.8 was suggested, which is similar to a loss factor of 2 used for a 90° bending pipe flow. Furthermore experimental results from literature were added in order to verify the limits found. Finally an extension to the operatability is presented for negative pressures on the upstream side of the nozzle, verified by with a custom made suction device.

In a following study by Byrne et al [77] the interaction between the capillary forces and inertial forces were examined. These forces give rise to a periodic movement of the melt puddle, in the natural frequency of the puddle. Low damping in the puddle cause the vibrations to persist. In turn the thickness of the ribbon is affected, causing a wave like pattern in the lengthwise direction. Using scaling analysis a model for the time scale of the vibratory motion is found. The model is adjusted with a proportionality constant. For reference the model is compared to an ideal situation of a vibrating droplet suspended in a gravity free environment, and with a solution found for a fixed contact angle meniscus. Using this model the frequency of the vibrating melt puddle, and therefore the wave defect in the ribbon can be calculated. The frequency can be calculated according to equation 15

$$\nu = C_v \left(\frac{\sigma}{\rho G^3} \right)^{\frac{1}{2}} \tag{15}$$

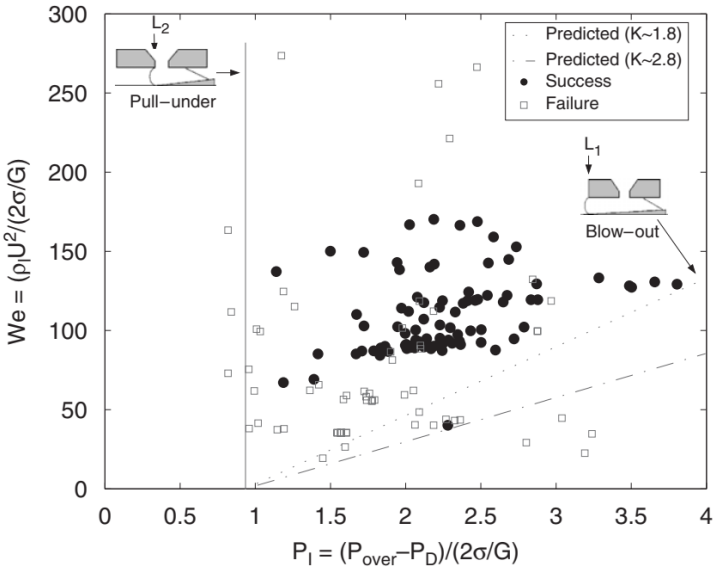

Fig. 30: Operating window as presented by Byrne et al. [28]

Theisen et al [29] modelled time dependent effects of the PFC process on the resulting ribbon. During casting the gap varies in time due to thermal expansion and out of roundness of the wheel. By calculating the temperature increase of the wheel due to the energy input from the molten metal on the wheel, a prediction of the gap size reduction was made. By adding a sinusoidal on top, variations from the out of roundness of the wheel were simulated. This results in predictions for the gap height, ribbon thickness, wheel temperature, and puddle length. The predictions were tested and are shown in figure 31.

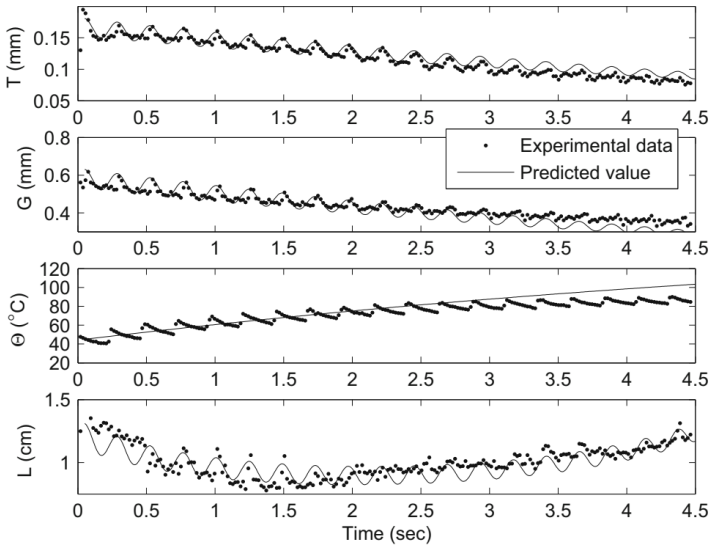

Fig. 31: Transient predictions and verification by Theisen et al. [29]

Li et al. [30] combined the work of Byrne et al [28] and Theisen et al. [29] to find an equations for the pressure loss factor K. It was found that K is dependent on the pressure, velocity of the wheel, and the normalized ribbon thickness as seen in equation 16. The normalized ribbon thickness is defined as the ribbon thickness divided by the gap size as seen in equation 17. The results were verified with one experimental casting. The values found for K were found to be between 1.8 and 2.2, in line with values predicted earlier in literature. The results from the predictions compared with the experimental casting can be seen in figure 32.

$$K = \frac{2(gH(t) - U^2/We)}{(\tau U)^2} - 1 \tag{16}$$

$$\tau = \frac{T}{G} \tag{17}$$

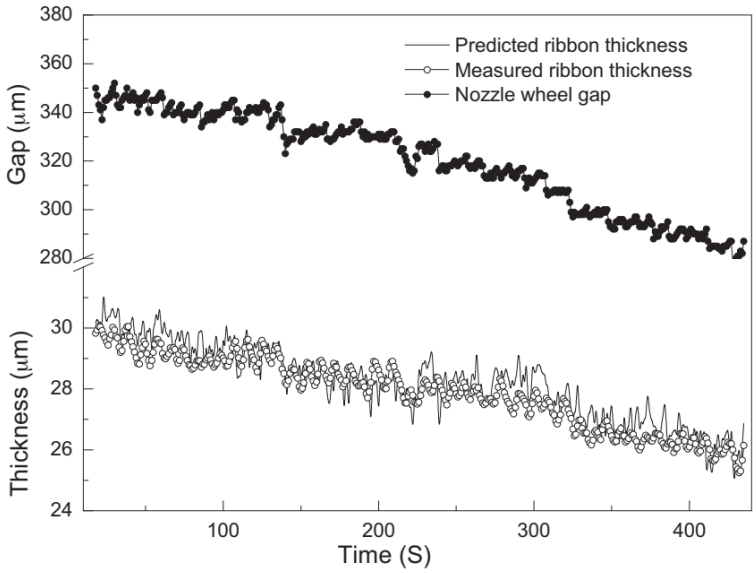

Fig. 32: Ribbon thickness predictions and verification by Li et al. [30]

Su et al [36] wrote a planar flow tuning guide, useful for bringing aforementioned knowledge into practice. By combining the operating window, experimental results from other authors, and a computational fluid dynamics (CFD) model, Su et al. devised a way to quickly find the appropriate values for the parameters governing the PFC process. Using this step by step guide, the operateability conditions for a specified alloy, ribbon thickness, and nozzle geometry can be found. Such a guide can be beneficial for quickly experimenting with different alloys and ribbon geometries. The tuning method was verified using CFD. In the resulting CFD analysis the vibration instability, caused by the interaction of capillary and inertial forces was also reconfirmed, and was in line with previous results from Byrne et al [77]. In recent work by Marot et al. [78] varying wheel speed is used at the startup phase of the process, in order to minimize sticking and oscillation on the wheel. Thereby reducing unwanted thickness variations in the ribbon. Furthermore experiments with nozzle geometry were performed. Finding a decrease in quality when using rounded of nozzle edges.

B. Thermodynamics

The second important aspect of the planar flow casting process are the thermodynamics, with a focus on the heat transfer from the melt puddle to the wheel. This parameter dictates the cooling rate achievable for the ribbon, and in turn its microsctructure. Other thermodynamic processes that have an effect on the planar flow casting process include:

- Heat transfer from the wheel to the cooling water
- Heat loss through radiation
- Heat loss through convection
- Convection inside the melt puddle
- Effect of latent heat
- Cooling water radiator

These effects are smaller, but contribute in a different way to the process. These effects have impact on the stability and longevity of the process. They therefore are important for larger industrial processes in which the quantity and timescales become larger. Understanding these parameters gives a better prediction for the final result.

Specific work on the heat transfer between the puddle and the wheel has been done by Carpenter et al. [79]. In their model, conduction, convection, and radiation, to and from the puddle are included. Heat flux to the puddle comes from the nozzle at the top of the puddle, which is significantly hotter than the wheel. Difficulties with this model lie in the fact that there is non-perfect contact between the nozzle and the puddle, and the wheel and the puddle. Gas pockets, dust, convection in the puddle, and a rough wheel surface a give rise to this imperfect contact. Furthermore there exists moving temperature profiles in the puddle, and the wheel, which increase the complexity of the system.

The heat transfer coefficient is defined by Carpenter et al. as: “The ratio of the heat flux from the metal (liquid or solid) across its boundary (interface) with the wheel, q, to the difference between the temperature at that boundary, T, and the nominal steady temperature of the chill wheel, T.” See equation 18.

$$q = H(x)(T - T_c) \tag{18}$$

The heat transfer coefficient is then calculated using two different methods. At first a heat balance is used to find a minimum value for the coefficient. The control volume used for the heat balance calculation can be seen in figure 33.

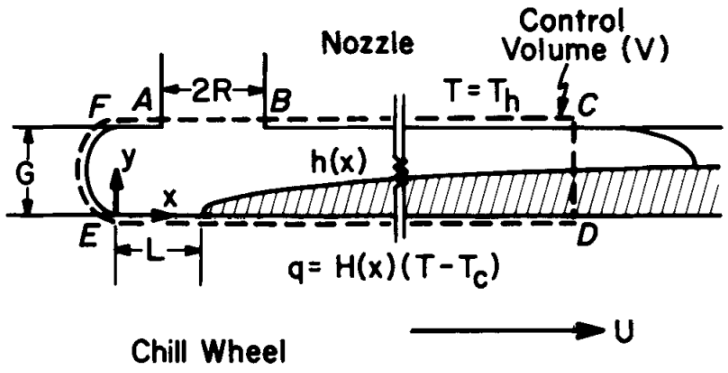

Fig. 33: Heat balance control volume, not to scale. from Carpenter et al. [31]

Second a temperature field is calculated for an idealized problem. The results from these methods are then applied to different alloys. The idealized model can be seen in figure 34.

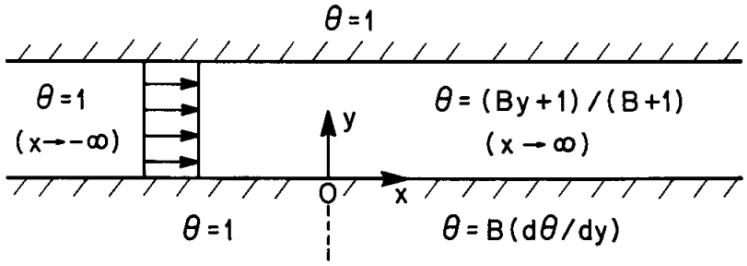

Fig. 34: Idealized problem model, not to scale. from Carpenter et al. [31]

The minimum heat transfer coefficient found by Carpenter et al. can be found in figure 35. These are minimum values for different castable alloys. Differences exist due to differences in melt temperature, latent heat, density, etc.

Metal	T_m (K)	k_l (J/m s K)	H_{min} (W/m^2 K)
Aluminum	933	100	$3.1 * 10^4$
Iron	1808	31	$4.1 * 10^3$
Nickel	1728	30	$4.2 * 10^3$
Magnesium	923	90	$2.9 * 10^4$
Copper	1256	165	$3.4 * 10^4$
Tin	505	30	$2.9 * 10^4$
Zinc	693	58	$2.9 * 10^4$

*$G = 5 \times 10^{-4}$ m, $T_c = 298$ K, and $T_h = T_m + 100$ K

Fig. 35: Minimum heat transfer coefficients for various alloys. from Carpenter et al. [31]

The resulting minimum heat transfer coefficient is significantly higher than that for free flow casting. This can be explained by the heat inflow from the nozzle that is in contact with the melt puddle during planar flow casting. This nozzle is not there for free flow casting.

The results from Cerpenter et al. are experimentally verified by Tkatch et al. [32] who devised a method for directly measuring the temperature of the melt puddle. Earlier attempts at this measurement lacked the resolution to, for instance, prove that latent heat was expelled during crystallization. These methods used in earlier work are photocalorimetric [80] or infrared [81] measurements. Tkatch et al. used an thermocouple imbedded into the cooling wheel surface, so in direct contact with the underside of the melt puddle. A thermocouple uses the thermoelectric effect to measure temperature. Temperature curves observed by Tkach et al. can be seen in figure 36.

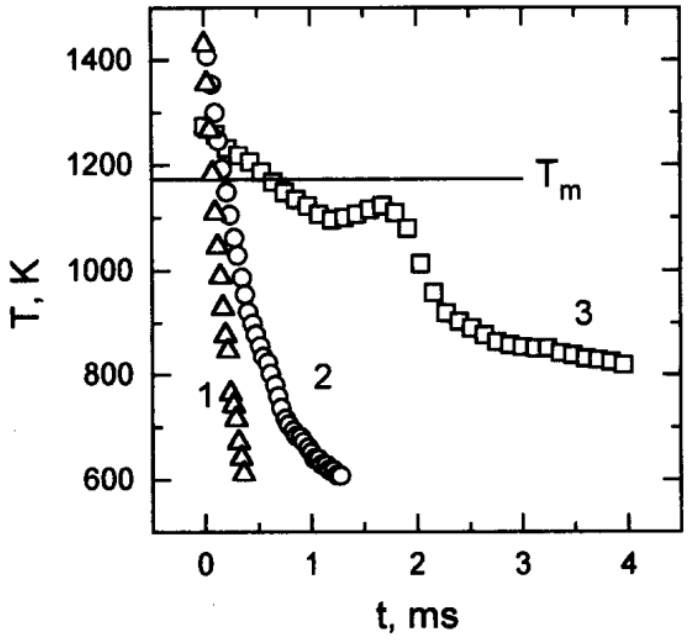

Fig. 36: Three temperature curves from Tkach et al. [32]. Curve 1 and 2 are for amorphous ribbons. Curve 3 is for a crystalline ribbon

From these temperature measurements, the cooling rate can be calculated. The cooling rate for the crystalline ribbon is slowed during solidification due the the expulsion of latent heat with crystallization. Therefore, only the part of temperature curve before solidification is used for the calculation of the cooling rate. In figure 37 the cooling rates can be seen. Using the temperature curve and the speed of the wheel, it can be calculated that solidification occurs at a distance of 7.5 mm or more. When Tkach et al. compare this with pictures from the melt puddle, which have a length of about 2 mm, it is concluded that the ribbon forms in liquid state, as a consequence of momentum transfer.

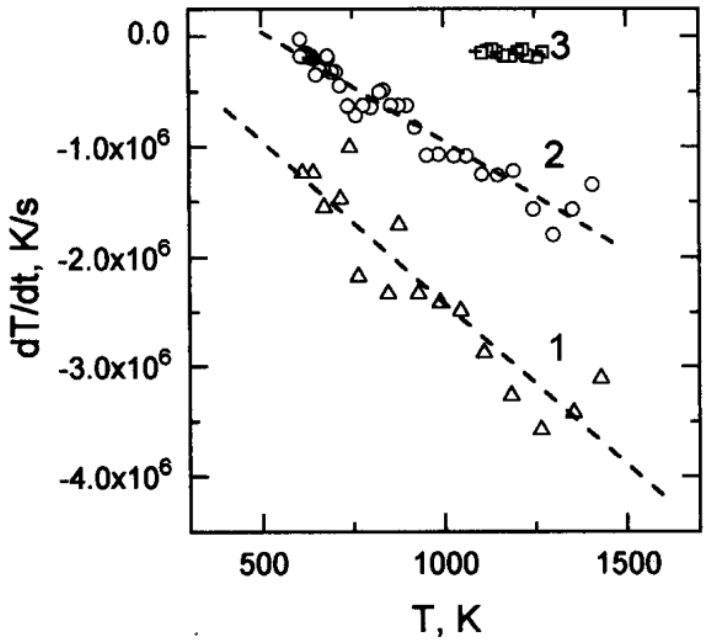

Fig. 37: Three cooling rate from Tkach et al. [32]. Curve 1 and 2 are for amorphous ribbons. Curve 3 is for a crystalline ribbon

The cooling rate appears close to linear, suggesting Newtonian cooling. However Tkach et al. point out that, due to the high Nusselt number, Newtonian cooling is not valid for this situation. Nusselt number estimations are made based on the work of Ruhl et al. [82]. Another reason why Newtonian cooling is not applicable, is the steep gradient present in the ribbon. This means that the cooling of the ribbon is not limited by the interface between the puddle and the wheel, but by the internal conduction through the ribbon. In other words the Biot number of the puddle is above one. The gradient in the ribbon can be observed by the difference in temperature on top of the puddle and at the puddle-wheel interface. The temperature gradient in the ribbon can be as high as $4.7 \cdot 10^7\ K/m$ according to Tkach et al. The effect of this can be seen in the resulting microstructure of the ribbon, which shows an increasing grain size along the height of the ribbon.

Although not physically correct, Tkach et al. still suggest using the Newtonian equation 19 and its derivative for cooling rate20, for the description of the heat transfer. In this equation T_2 and T_{10} are the initial temperatures of the melt and the substrate respectively, d is the ribbon thickness, h is the heat transfer coefficient, t is time, and ρ is density. Tkach et al. find heat transfer ranging from $4.3 \cdot 10^4$ to $4 \cdot 10^5\ W/m^2K$, for a ribbons thickness ranging from 65 to 24 μm.

$$T(t) = T_2 + (T_{10} - T_2)^{\frac{-ht}{\rho c d}} \tag{19}$$

$$\dot{T}(T) = \frac{h}{\rho c d}(T - T_2) \tag{20}$$

C. Simulations

Multiple numerical simulations have been carried out by different research groups. These simulation include, computational fluid dynamics, heat transfer, solidification, and a combinations of all. These simulations vary in detail and complexity. Earlier work lacks detail due to computing power limitations. These works use a low resolution mesh, or look at only a small part of the process. Numerical work is based on earlier mathematical models created. For example on the work by Gutierrez et al. [83] who created a mathematical model that looked at the downstream area of the process. Other work include that of Gong et al. [84], who focused on the boundary layer. The works of Wu et al. [85] and Chen et al. [86] are one of the earliest to include a 2D simulation of the puddle. The mesh sized used, was too coarse to resolve any detail in the resulting flow. Improvements to the resolution came with the work of Bussmann et al. [87]. Who apart from a finer mesh, also included surface wetting in the simulation.

The insight gained from these studies and simulations can be described using the result from a more recent study from Liu et al. [33]. In this work a 2D multi physics heat and flow simulation is made of the initial flow development during planar flow casting. This simulation is for an amorphous ribbon, so it doesn't take crystallization into account. What is included is an heat transfer model to the spinning wheel. Initial flow development is a highly unstable moment in the whole process. During this time the wheel surface has to heat up to its equilibrium temperature, and therefore initial heat transfer from the fluid to the wheel is much higher than during a stable process. This means that the release point and the menisci positions are changing during this period. According to Liu et al. stable flow develops within millisecond, at most 6 milliseconds. This however doesn't not take into account longer term transients such as wheel expansion, when the total system, including the wheel cooling system, get to equilibrium. Results from Liu et al. show flow and temperature fields developing in time, for different process parameters. The model predicts the shape and size of the melt puddle. The results found, are in accordance with images taken by experimental research from other groups. In figure 38 a comparison can be seen between the simulated work from Liu et al. and the experimental work of Wilde et al. with regards to initial flow development. Although not directly comparable due to different operating parameters and alloys used, it does show strong similarities.

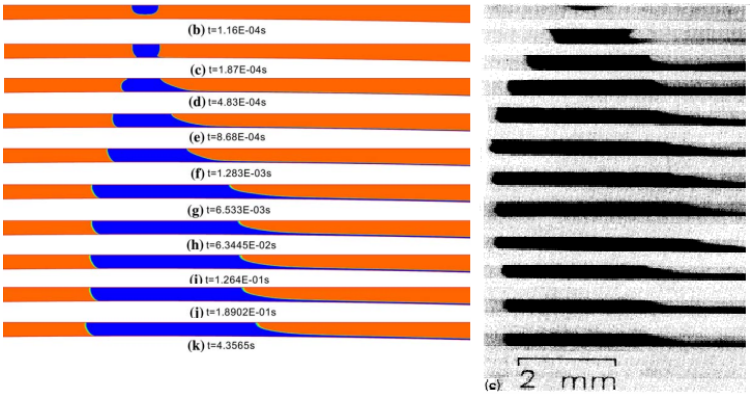

Fig. 38: Comparison between simulated results for initial flow development from Liu et al. [33] (left) and experimental results from Wilde et al. [34] (right). Both images are edited versions of the original.

Furthermore temperature profiles from the melt puddle and the cooling wheel are presented. Heat transfer in the melt puddle is the result of two circulating flows within the melt puddle, at the upstream and downstream positions. These are formed when the puddle reaches its meta-stable state. An example of these flows and temperature profiles can be seen in figure 39.

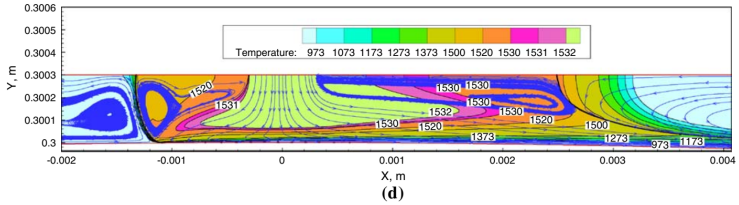

Fig. 39: Temperature profiles and streamlines in the melt puddle from Liu et al. [33] at 4.3 seconds

Temperature profiles of the cooling wheel show a heat penetrating depth of 3 mm, suggesting that the most heat is only transferred to surface of the cooling wheel. An instantanious temperature profile below the melt puddle can be seen in figure 40.

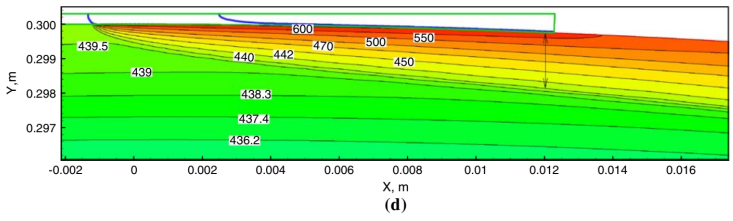

Fig. 40: Temperature profiles below the puddle from Liu et al. [33] at 4.3 seconds

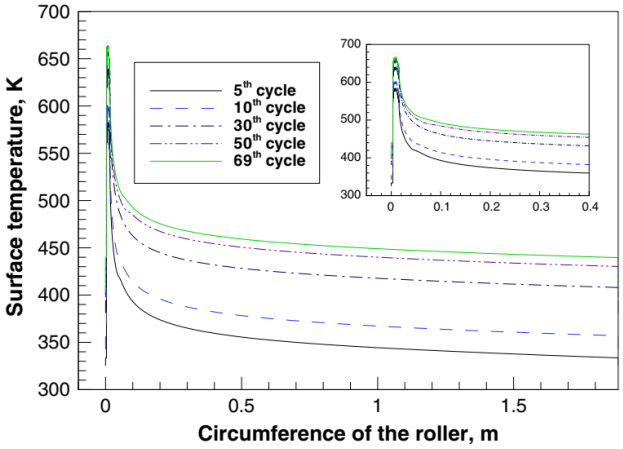

(a) Surface temperature cooling wheel for multiple different cycles

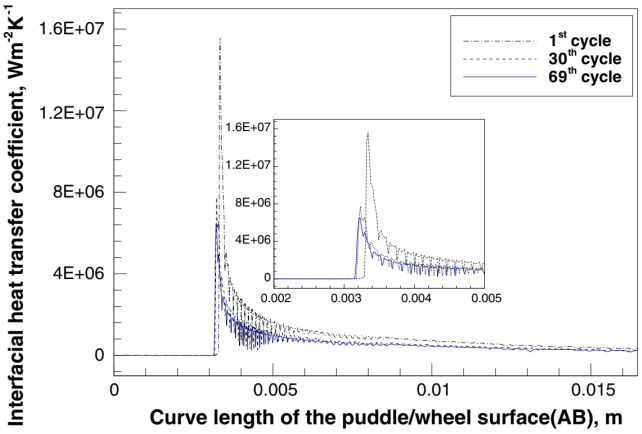

(b) Heat transfer coefficient between melt puddle and cooling wheel for multiple different cycles

Fig. 41: Results from Liu et al. [33]

Every rotation heat is added to the surface of the wheel, until an equilibrium is reached. It is shown that the heat transfer decreases exponentially with time, due to the temperature increase of the wheel. Both results can be seen in figure 41.

Liu et al. calculate that the cooling rate at the melt puddle is above $10^6\ K/s$. They conclude therefore that there will be glass forming instead of crystallization. This however, is highly dependent on the specific alloy used, which is not specified. One of the assumptions made beforehand is that the ribbon will not crystallize and therefore will not release latent heat. This in turn affects the cooling rate found using simulation. So the conclusion that no crystallization will take place seems premature.

Effects of the gap and and nozzle slit size are also simulated and discussed. A larger slit needs more time to reach stability, increases heat and mass flow through the system, and creates steeper menisci. A steeper upstream meniscus can lead to air entrapment and casting failure. A different gap size however, has a minimal effect on the temperature distribution in the wheel. A larger gap size does decrease the cooling rate of the ribbon. Longer term effect were taken into account by Theisen et al. [29], Described earlier in this work in section: V-A.

VI. Discussion

Materials get their properties from the microstructure. Controlling the microstructure is key to get the desired performance, and consistency from the material. In the rapid solidification process material from multiple flakes is combined into bulk material. Therefore the microstructure in the bulk is a mixture of different grain sizes found within the flake, and between the different flakes. In order to ensure similar properties in the bulk material, the differences in microstructure or grain sizes must be minimized. Since the microstructure is a result of the cooling rate of the material, which in turn depends on the ribbon thickness, the ribbon must be cast a thin as possible with minimal variation in thickness over the width and length of the ribbon. A goal for the planar flow casting machine is to reduce the average ribbon thickness to 50 μm. According to literature capillary instability can create thickness variations by vibrations of 40 μm. Therefore the goal is set to 40-80 μm. Creating significant improvements of the average microstructure compared to materials made on the free flow casting machine. The second goal is to achieve this whilst only controlling for the over pressure in the crucible, simplifying the casting process.

VII. Recommendation

The planar flow casting process is governed by 15 different variables, see table II. Of these variables four have a critical influence on the process and determine the final ribbon thickness. These four parameters need to be controlled in order to perform a successful cast. For an optimal result and flexibility the planar flow casting machine must be able to operate over the full range of parameters leading to a successful cast. This leads to the requirements for the design of the planar flow casting machine. The four parameters are: wheel speed, gap between the wheel and nozzle, pressure, and nozzle breadth. With these parameters an operating window can be plotted, to show which parameter combinations lead to a successful cast.

Apart from the process, material composition is important factor. Good understanding of the material is needed to determine the feasibility of certain microstructure and or desired properties. Furthermore the material also influences the process. Viscosity, latent heat, glass forming ability and crystallization time, are all factors to consider for a successful cast.

VIII. Research proposal

The following steps will be taken to fulfill the research and design goals of this project. A thorough analysis of the thermo- and fluid dynamics of the planar flow casting process will be used to choose and optimize the values of the relevant parameters found in literature. These values will be checked and further refined using a multi physics simulation created in Comsol.

When this is completed, requirements for the nozzle, external pressure system and control system will be set according to the result found previously. Then the nozzle can be manufactured, and the measurement and control systems acquired. These systems will be implemented on the existing planar flow cast test machine. During dry runs the new equipment can be validated and tuned. When successful, wet runs with molten alloy can commence, starting with a limited amount of material and parameters optimized for stability rather than cooling rate. After a full scale test run, parameters can slowly be adjusted in the direction that leads to the highest cooling rate in the ribbon.

Since direct gap control with the current test setup is not possible without a total rebuilt, pressure control will be used in order to compensate for the changes in the other variables. This control technique would relax requirements for future planar flow systems and make a movable wheel or nozzle obsolete.

The geometry and microstructure of the resulting ribbon will be analysed and compared with ribbons manufactured by free flow casting. The thickness, thickness variation over width and length, width, length, and surface quality will be quantified. For the microstructure, the same will be done for grain size, grain size distribution and phase distribution. Analysis will done using: XRD, SEM, EDX and phase transition simulations.

Finally both areas of research can be coupled. The cooling rate of the ribbon found using a heat balance and Comsol simulations, can be linked to solidification rates observed in the microstructure. Furthermore, the increased cooling rates of the planar flow casting process in comparison with the free flow casting process can be verified. This will be important in controlling and predicting material properties using process parameters.

IX. Search path

Two mind maps in figure 43 and figure 42 are utilized to organize the various topics and subtopics related to the rapid solidification process. These mind maps establish connections between different subjects, increasing in detail with each node. The scope of the review is visually represented. Knowledge on all these subjects is needed to successfully couple the planar flow parameters to the eventual material properties.

To search for resources on the planar flow casting process, the following method was employed. Since the goal of planar flow casting is the continuous casting of a rapidly solidified metal, a recent (2010) review on rapid solidification technique was chosen to start this research. This is the review of Lavernia et al. [46]. This review featured other methods for creating rapidly solidified thin ribbons, using a slightly different technique as compared with FFC or PFC. These techniques include crucible melt extraction and the melt drag method. The review added more possible search terms for further research such as: chill block melt spinning, free jet melt spinning, rapidly quenched materials, and the Taylor wire process. From this review, citations where used to find earlier mentions of planar flow casting, such as the older review from Jones et al. from 1984 [88]. From Jones et al. The patent [40] and first use of planar flow casting was found, which marks the start of the research topic. Older patents on which planar flow casting is based are for instance the patent from Strange [89] dating from 1911. With a more narrow search window and multiple search terms, the focused was moved to the physics governing the planar flow casting process. This lead to Paul H. Steen [72] and his extensive work on PFC. Via the work of Steen details on subtopics such as nozzle dimensions, fluid dynamics, heat transfer, wheel material and quality, and experimental data could be found. Two PhD dissertations on planar flow casting [73] [90] where written under supervision of Steen. Finally works on simulating the PFC process were sought by including terms as: Simulation, simulating, numerical, and modeling.

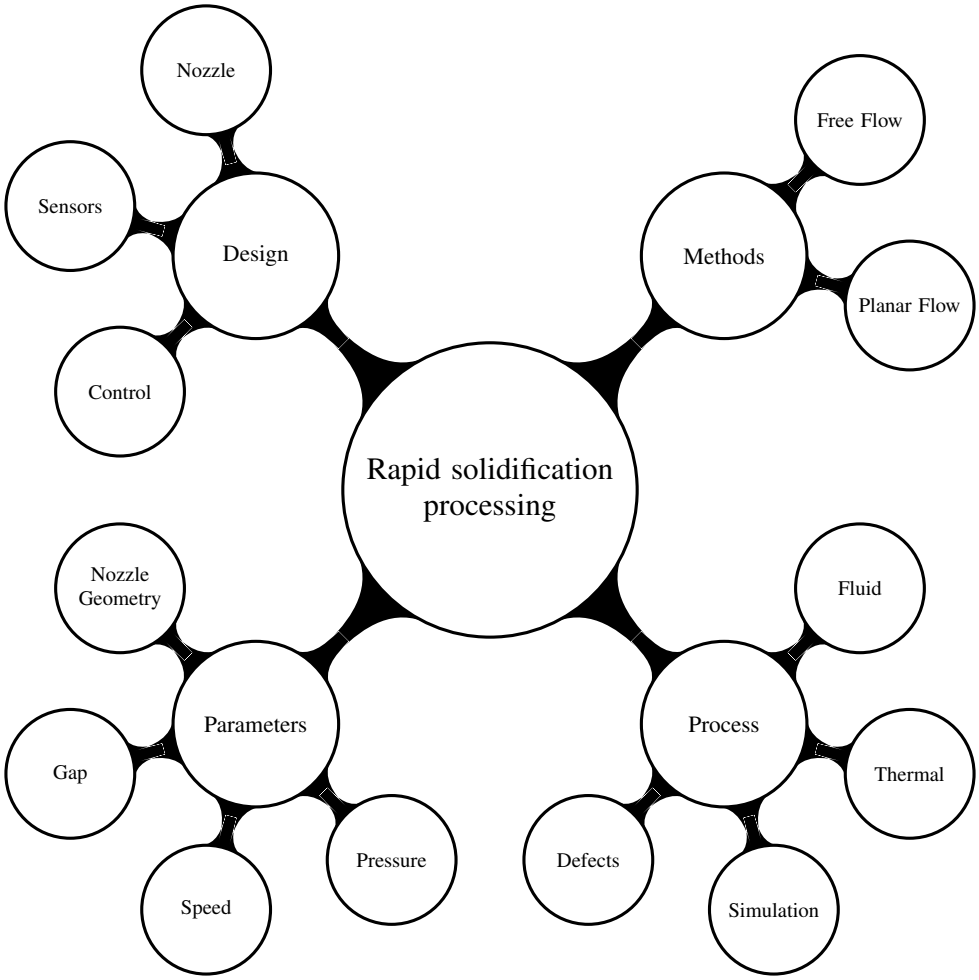

Fig. 42: Topics part of mechanical engineering included in RSP

A different approach was chosen for the material science aspect of this review. The chosen stating point was rapid solidification, the physics that separates this material from metals more commonly used in industry. Therefor the fundamentals of phase change and solidification were revisited, readily available in books on the subject [7] [2]. More specific information on the structure of rapidly cooled metals was also available in books, such as from Gusev et al. [54] on nanocrystalline metals and Kovalenko et al. [91] on the physics of amorphous metals. A more narrow search was done on the specific alloy produced at RSP. Searches on AlSi alloy, and hypereutectic AlSi alloy were done. These searches were then combined with rapid solidification.

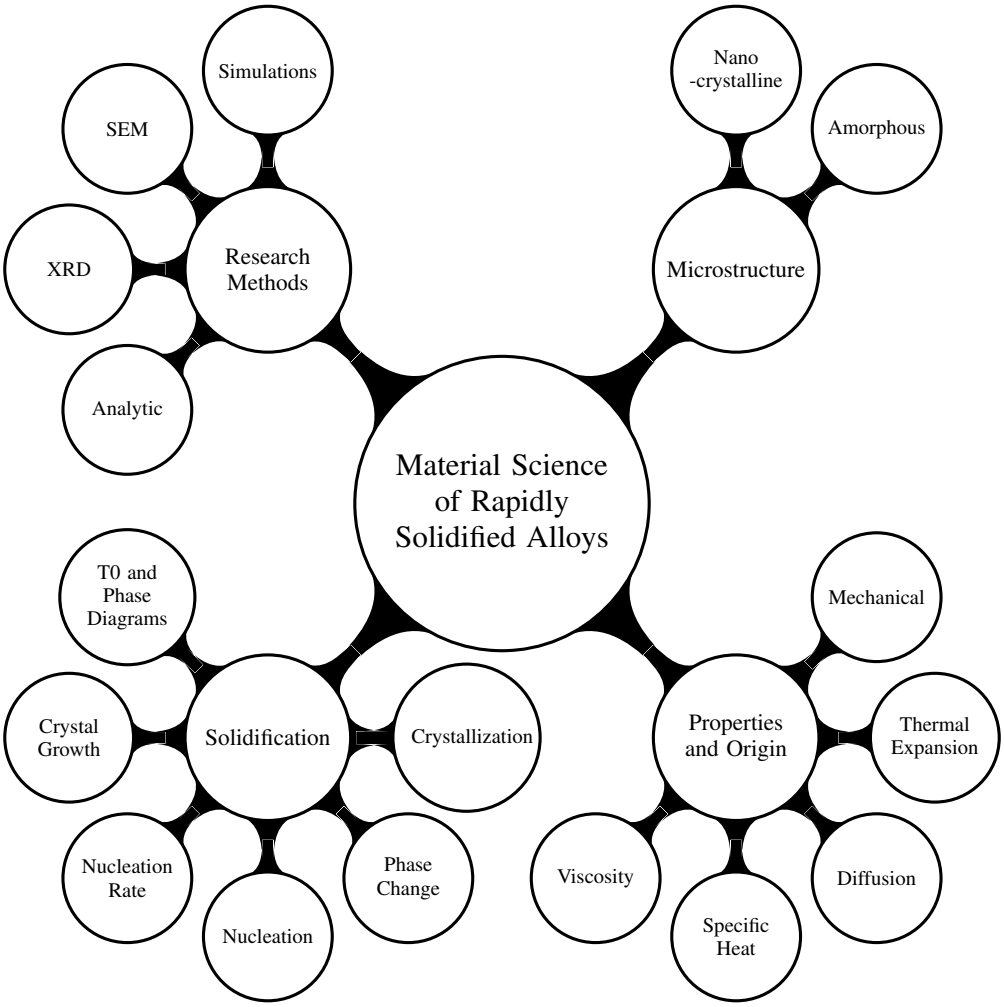

Fig. 43: Topics part of material science included in RSP

In table III the number of sources found on the different topics and subtopics of this literature review are presented. One source can occur in multiple subtopics.

In table IV Authors and co-authors with 3 or papers are presented.

TABLE III: Number of sources on the various subtopics of the rapid solidification process

Topic	**Nr. sources**
Material Science	96
- Microstructure	89
- AlSi Alloy	19
- Solidification	69
- Nanocrystalline	17
- Amorphous	23
- Simulations	4
Mechanical Engineering	68
- Planar Flow	54
- Measurement and Control	11
- Process	39
- Fluid	10
- Thermal	2
- Simulation	8
- Experiments	3
Total	161

TABLE IV: Author or co-author with 3 or more papers used in this review

Author or Co-author	**Nr. papers**
Byrne	3
Carpenter	3
Inoue	4
Lavernia	3
Steen	14
Theisen	3
Weinstein	3

REFERENCES

[1] C. J. Byrne, A. M. Kueck, S. P. Baker, and P. H. Steen, "In situ manipulation of cooling rates during planar-flow melt spinning processing," *Materials Science and Engineering: A*, vol. 459, no. 1-2, pp. 172–181, Jun. 2007. [Online]. Available: https://linkinghub.elsevier.com/retrieve/pii/S0921509307000093

[2] D. Porter and K. Easterling, *Phase Transformations in Metals and Alloys (Revised Reprint)*. CRC Press, 2009. [Online]. Available: https://books.google.nl/books?id=axDSBQAAQBAJ

[3] D. Fisher, "Fundamentals of Solidification," *Fundamentals of Solidification*, pp. 1–316, 1998, publisher: Trans Tech Publications Ltd. [Online]. Available: https://www.torrossa.com/it/resources/an/5376094

[4] W. J. Boettinger and D. K. Banerjee, "7 - Solidification," in *Physical Metallurgy (Fifth Edition)*, D. E. Laughlin and K. Hono, Eds. Oxford: Elsevier, Jan. 2014, pp. 639–850. [Online]. Available: https://www.sciencedirect.com/science/article/pii/B9780444537706000071

[5] K. F. Kelton and A. L. Greer, *Nucleation in Condensed Matter: Applications in Materials and Biology*. Elsevier, Mar. 2010, google-Books-ID: x75bXd_gYOMC.

[6] W. J. Boettinger, "Growth Kinetic Limitations During Rapid Solidification," *MRS Proceedings*, vol. 8, p. 15, 1981. [Online]. Available: http://link.springer.com/10.1557/PROC-8-15

[7] H. Fredriksson and U. Åkerlind, *Solidification and Crystallization Processing in Metals and Alloys*, 1st ed. Wiley, Aug. 2012. [Online]. Available: https://onlinelibrary.wiley.com/doi/book/10.1002/9781119975540

[8] P. G. Debenedetti and F. H. Stillinger, "Supercooled liquids and the glass transition," *Nature*, vol. 410, no. 6825, pp. 259–267, Mar. 2001, number: 6825 Publisher: Nature Publishing Group. [Online]. Available: https://www.nature.com/articles/35065704

[9] R. Busch, J. Schroers, and W. H. Wang, "Thermodynamics and Kinetics of Bulk Metallic Glass," *MRS Bulletin*, vol. 32, no. 8, pp. 620–623, Aug. 2007. [Online]. Available: http://link.springer.com/10.1557/mrs2007.122

[10] A. Hirata, P. Guan, T. Fujita, Y. Hirotsu, A. Inoue, A. R. Yavari, T. Sakurai, and M. Chen, "Direct observation of local atomic order in a metallic glass," *Nature Materials*, vol. 10, no. 1, pp. 28–33, Jan. 2011. [Online]. Available: https://www.nature.com/articles/nmat2897

[11] F. Spaepen, "A microscopic mechanism for steady state inhomogeneous flow in metallic glasses," *Acta Metallurgica*, vol. 25, no. 4, pp. 407–415, Apr. 1977. [Online]. Available: https://linkinghub.elsevier.com/retrieve/pii/0001616077902322

[12] M. Chen, A. Inoue, W. Zhang, and T. Sakurai, "Extraordinary plasticity of ductile bulk metallic glasses," *Physical review letters*, vol. 96, no. 24, p. 245502, 2006.

[13] N. Mattern, U. Kühn, H. Hermann, S. Roth, H. Vinzelberg, and J. Eckert, "Thermal behavior and glass transition of Zr-based bulk metallic glasses," *Materials Science and Engineering: A*, vol. 375-377, pp. 351–354, Jul. 2004. [Online]. Available: https://www.sciencedirect.com/science/article/pii/S0921509303011493

[14] C. Suryanarayana and A. Inoue, *Bulk Metallic Glasses*. CRC Press, Nov. 2017, google-Books-ID: XGpQDwAAQBAJ.

[15] C. A. Angell, "Formation of Glasses from Liquids and Biopolymers," *Science*, vol. 267, no. 5206, pp. 1924–1935, Mar. 1995. [Online]. Available: https://www.science.org/doi/10.1126/science.267.5206.1924

[16] A. M. Glezer, N. A. Shurygina, E. N. Blinova, I. E. Permyakova, and S. A. Firstov, "Approach to the Theoretical Strength of Ti–Ni–Cu Alloy Nanocrystals by Grain Boundary Design," *Journal of Materials Science & Technology*, vol. 31, no. 1, pp. 91–96, Jan. 2015. [Online]. Available: https://linkinghub.elsevier.com/retrieve/pii/S1005030214001753

[17] K. Lu, "Nanocrystalline metals crystallized from amorphous solids: nanocrystallization, structure, and properties," *Materials Science and Engineering: R: Reports*, vol. 16, no. 4, pp. 161–221, Apr. 1996. [Online]. Available: https://linkinghub.elsevier.com/retrieve/pii/0927796X95001875

[18] G. Wilde, "Physical Metallurgy of Nanocrystalline Metals," in *Physical Metallurgy*. Elsevier, 2014, pp. 2707–2805. [Online]. Available: https://linkinghub.elsevier.com/retrieve/pii/B9780444537706000265

[19] J. L. Murray and A. J. McAlister, "The Al-Si (Aluminum-Silicon) system," *Bulletin of Alloy Phase Diagrams*, vol. 5, no. 1, pp. 74–84, Feb. 1984. [Online]. Available: https://doi.org/10.1007/BF02868729

[20] M. Warmuzek, *Aluminum-silicon casting alloys: an atlas of microfractographs*. Materials Park, OH: ASM International, 2004.

[21] J. H. Abboud and J. Mazumder, "Ultra-refined primary and eutectic silicon in rapidly solidified laser produced hypereutectic Al–Si alloys," *Advances in Materials and Processing Technologies*, pp. 1–23, Apr. 2021. [Online]. Available: https://www.tandfonline.com/doi/full/10.1080/2374068X.2021.1913326

[22] M. Papanikolaou, K. Salonitis, and M. Jolly, "Molecular Dynamics Simulations of the Solidification of Pure Aluminium," *Light Metals 2020*, pp. 158–167, 2020, series Title: The Minerals, Metals & Materials Series. [Online]. Available: http://link.springer.com/10.1007/978-3-030-36408-3_22

[23] P. Wesseling, "Quantitative evaluation of -Al nano-particles in amorphous Al87Ni7Gd6—comparison of XRD, DSC, and TEM," *Scripta Materialia*, vol. 48, no. 11, pp. 1537–1541, Jun. 2003. [Online]. Available: https://linkinghub.elsevier.com/retrieve/pii/S1359646203001271

[24] L. Anestiev, "An analysis of the dependence between the ribbon dimensions and the technological parameters for the planar flow casting method," *Materials Science and Engineering: A*, vol. 131, no. 1, pp. 115–121, Jan. 1991. [Online]. Available: https://linkinghub.elsevier.com/retrieve/pii/092150939190350V

[25] J. Sung, M. Kim, C. Park, and Y. Kim, "Theoretical expectation of strip thickness in planar flow casting process," *Materials Science and Engineering: A*, vol. 181-182, pp. 1237–1242, May 1994. [Online]. Available: https://linkinghub.elsevier.com/retrieve/pii/0921509394908389

[26] T. J. Praisner, J. S. J. Chen, and A. A. Tseng, "An experimental study of process behavior in planar flow melt spinning," *Metallurgical and Materials Transactions B*, vol. 26, no. 1, pp. 1199–1208, Feb. 1995. [Online]. Available: http://link.springer.com/10.1007/BF02654005

[27] J. K. Carpenter and P. H. Steen, "Planar-flow spin-casting of molten metals: process behaviour," *Journal of Materials Science*, vol. 27, no. 1, pp. 215–225, Jan. 1992. [Online]. Available: https://doi.org/10.1007/BF00553859

[28] C. J. Byrne, E. A. Theisen, P. H. Steen, and B. L. Reed, "Capillary puddle vibrations linked to casting-defect formation in planar-flow melt spinning," *Metallurgical and Materials Transactions B*, vol. 37, no. 3, pp. 445–456, Jun. 2006. [Online]. Available: http://link.springer.com/10.1007/s11663-006-0029-4

[29] E. Theisen, M. Davis, S. Weinstein, and P. Steen, "Transient behavior of the planar-flow melt spinning process," *Chemical Engineering Science*, vol. 65, no. 10, pp. 3249–3259, May 2010. [Online]. Available: https://linkinghub.elsevier.com/retrieve/pii/S0009250910000849

[30] D. Li, J. Zhuang, T. Liu, Z. Lu, and S. Zhou, "The pressure loss and ribbon thickness prediction in gap controlled planar-flow casting process," *Journal of Materials Processing Technology*, vol. 211, no. 11, pp. 1764–1767, Nov. 2011. [Online]. Available: https://linkinghub.elsevier.com/retrieve/pii/S092401361100152X

[31] J. Carpenter and P. Steen, "Heat transfer and solidification in planar-flow melt-spinning: high wheelspeeds," *International Journal of Heat and Mass Transfer*, vol. 40, no. 9, pp. 1993–2007, Jun. 1997. [Online]. Available: https://linkinghub.elsevier.com/retrieve/pii/S0017931096003055

[32] V. Tkatch, S. Denisenko, and O. Beloshov, "DIRECT MEASUREMENTS OF THE COOLING RATES IN THE SINGLE ROLLER RAPID SOLIDIFICATION TECHNIQUE," *Acta Materialia*, vol. 45, no. 7, pp. 2821–2826, Jul. 1997. [Online]. Available: https://linkinghub.elsevier.com/retrieve/pii/S1359645496003771

[33] H. Liu, W. Chen, S. Qiu, and G. Liu, "Numerical Simulation of Initial Development of Fluid Flow and Heat Transfer in Planar Flow Casting Process," *Metallurgical and Materials Transactions B*, vol. 40, no. 3, pp. 411–429, Jun. 2009. [Online]. Available: http://link.springer.com/10.1007/s11663-009-9236-0

[34] P. Wilde and E. Matthys, "Experimental investigation of the planar flow casting process: development and free surface characteristics of the solidification puddle," *Materials Science and Engineering: A*, vol. 150, no. 2, pp. 237–247, Feb. 1992. [Online]. Available: https://linkinghub.elsevier.com/retrieve/pii/092150939290117J

[35] J. Abboud and J. Mazumder, "Developing of nano sized fibrous eutectic silicon in hypereutectic Al–Si alloy by laser remelting," *Scientific Reports*, vol. 10, no. 1, p. 12090, Dec. 2020. [Online]. Available: http://www.nature.com/articles/s41598-020-69072-1

[36] Y.-G. Su, F. Chen, C.-M. Chang, C.-Y. Wu, M.-H. Chang, and C. A. Chung, "Tuning the Planar-Flow Melt-Spinning Process Subject to Operability Conditions," *JOM*, vol. 66, no. 7, pp. 1277–1286, Jul. 2014. [Online]. Available: http://link.springer.com/10.1007/s11837-014-0982-3

[37] "RSP Technology - Home -." [Online]. Available: https://www.rsp-technology.com/NL/

[38] L. Katgerman and F. Dom, "Rapidly solidified aluminium alloys by meltspinning," *Materials Science and Engineering: A*, vol. 375-377, pp. 1212–1216, Jul. 2004. [Online]. Available: https://linkinghub.elsevier.com/retrieve/pii/S0921509303011146

[39] M. T. Smith and M. Saletore, "Simple, low-cost planar flow casting machine for rapid solidification processing," *Review of Scientific Instruments*, vol. 57, no. 8, pp. 1647–1653, Aug. 1986. [Online]. Available: http://aip.scitation.org/doi/10.1063/1.1138544

[40] M. C. Narasimhan, "Continuous casting method for metallic strips," US Patent US4 142 571A, Mar., 1979. [Online]. Available: https://patents.google.com/patent/US4142571/en?oq=US+Patent+4142571

[41] S. Hirosawa, Y. Shigemoto, T. Miyoshi, and H. Kanekiyo, "Direct formation of Fe3B/Nd2Fe14B nanocomposite permanent magnets in rapid solidification," *Scripta Materialia*, vol. 48, no. 7, pp. 839–844, Apr. 2003. [Online]. Available: https://linkinghub.elsevier.com/retrieve/pii/S1359646202006206

[42] S.-R. Moon, K. Byerly, P. Ohodnicki, M. McHenry, S. Simizu, A. M. Leary, V. Keylin, R. Noebe, R. Bowman, R. Beddingfield *et al.*, "Strain annealed metal amorphous nanocomposite soft magnetic materials: Manufacturing, applications, optimization, and data sheets," National Energy Technology Laboratory (NETL), Pittsburgh, PA, Morgantown, WV ..., Tech. Rep., 2019.

[43] M. Mueller, M. Riede, S. Eberle, A. Reutlinger, A. D. Brandão, L. Pambaguian, A. Seidel, E. López, F. Brueckner, E. Beyer, and C. Leyens, "Microstructural, mechanical, and thermo-physical characterization of hypereutectic AlSi40 fabricated by selective laser melting," *Journal of Laser Applications*, vol. 31, no. 2, p. 022321, May 2019. [Online]. Available: http://lia.scitation.org/doi/10.2351/1.5096131

[44] G. Onwuka, K. Abou-El-Hossein, and Z. Mkoko, "AE Monitoring of Diamond Turned Rapidly Soldified Aluminium 443," *Journal of Physics: Conference Series*, vol. 843, p. 012059, May 2017. [Online]. Available: https://iopscience.iop.org/article/10.1088/1742-6596/843/1/012059

[45] N. Overman, S. Mathaudhu, J. Choi, T. Roosendaal, and S. Pitman, "Microstructure and mechanical properties of a novel rapidly solidified, high-temperature Al-alloy," *Materials Characterization*, vol. 112, pp. 142–148, Feb. 2016. [Online]. Available: https://linkinghub.elsevier.com/retrieve/pii/S104458031530084X

[46] E. J. Lavernia and T. S. Srivatsan, "The rapid solidification processing of materials: science, principles, technology, advances, and applications," *Journal of Materials Science*, vol. 45, no. 2, pp. 287–325, Jan. 2010. [Online]. Available: https://doi.org/10.1007/s10853-009-3995-5

[47] E. J. Lavernia, J. D. Ayers, and T. S. Srivatsan, "Rapid solidification processing with specific application to aluminium alloys," *International Materials Reviews*, vol. 37, no. 1, p. 44, 1992.

[48] A. Greer, "Metallic Glasses," in *Physical Metallurgy*. Elsevier, 2014, pp. 305–385. [Online]. Available: https://linkinghub.elsevier.com/retrieve/pii/B9780444537706000046

[49] A. Inoue, "Stabilization of metallic supercooled liquid and bulk amorphous alloys," *Acta Materialia*, vol. 48, no. 1, pp. 279–306, Jan. 2000. [Online]. Available: https://www.sciencedirect.com/science/article/pii/S1359645499003006

[50] D. Miracle, W. Sanders, and O. N. Senkov, "The influence of efficient atomic packing on the constitution of metallic glasses," *Philosophical Magazine*, vol. 83, no. 20, pp. 2409–2428, Jul. 2003. [Online]. Available: http://www.tandfonline.com/doi/abs/10.1080/14786430310000098828

[51] G. Palumbo, S. Thorpe, and K. Aust, "On the contribution of triple junctions to the structure and properties of nanocrystalline materials," *Scripta Metallurgica et Materialia*, vol. 24, no. 7, pp. 1347–1350, Jul. 1990. [Online]. Available: https://linkinghub.elsevier.com/retrieve/pii/0956716X9090354J

[52] P. Knauth and J. Schoonman, *Nanocrystalline Metals and Oxides: Selected Properties and Applications*. Springer Science & Business Media, Apr. 2006, google-Books-ID: QNULBwAAQBAJ.

[53] H. Gleiter, *Progress in Materials Science: Nanocrystalline materials*. Pergamon Press, 1990, google-Books-ID: GKpMzQEACAAJ.

[54] A. I. Gusev and A. A. Rempel, *Nanocrystalline Materials*. Cambridge Int Science Publishing, 2004, google-Books-ID: kO8wzHV0xZ0C.

[55] A. M. Glezer and N. A. Shurygina, *Amorphous-Nanocrystalline Alloys*. CRC Press, Dec. 2017, google-Books-ID: ymhQDwAAQBAJ.

[56] A. S. Argon and S. Yip, "The strongest size," *Philosophical Magazine Letters*, vol. 86, no. 11, pp. 713–720, Nov. 2006. [Online]. Available: http://www.tandfonline.com/doi/abs/10.1080/09500830600986091

[57] M. Meyers, A. Mishra, and D. Benson, "Mechanical properties of nanocrystalline materials," *Progress in Materials Science*, vol. 51, no. 4, pp. 427–556, May 2006. [Online]. Available: https://linkinghub.elsevier.com/retrieve/pii/S0079642505000447

[58] O. Gusakova, V. Shepelevich, D. V. Alexandrov, and I. O. Starodumov, "Formation of the microstructure of rapidly solidified hypoeutectic Al-Si alloy," *The European Physical Journal Special Topics*, vol. 229, no. 2-3, pp. 417–425, Feb. 2020. [Online]. Available: http://link.springer.com/10.1140/epjst/e2019-900136-9

[59] S.-Z. Lu and A. Hellawell, "Growth mechanisms of silicon in Al-Si alloys," *Journal of Crystal Growth*, vol. 73, no. 2, pp. 316–328, Nov. 1985. [Online]. Available: https://linkinghub.elsevier.com/retrieve/pii/0022024885903082

[60] R.-y. Wang, W.-h. Lu, and L. M. Hogan, "Twin related silicon crystals in Al–Si alloys and their growth mechanism," *Materials Science and Technology*, vol. 11, no. 5, pp. 441–449, May 1995, publisher: Taylor & Francis _eprint: https://doi.org/10.1179/mst.1995.11.5.441. [Online]. Available: https://doi.org/10.1179/mst.1995.11.5.441

[61] K. Nogita, J. Drennan, and A. Dahle, "Evaluation of Silicon Twinning in Hypo-Eutectic Al-Si Alloys," *MATERIALS TRANSACTIONS*, vol. 44, no. 4, pp. 625–628, 2003. [Online]. Available: https://www.jstage.jst.go.jp/article/matertrans/44/4/44_4_625/_article

[62] C. Xu, H. Wang, F. Qiu, Y. Yang, and Q. Jiang, "Cooling rate and microstructure of rapidly solidified Al–20wt.% Si alloy," *Materials Science and Engineering: A*, vol. 417, no. 1-2, pp. 275–280, Feb. 2006. [Online]. Available: https://linkinghub.elsevier.com/retrieve/pii/S0921509305013377

[63] L. Tian, Y. Guo, J. Li, F. Xia, M. Liang, and Y. Bai, "Effects of Solidification Cooling Rate on the Microstructure and Mechanical Properties of a Cast Al-Si-Cu-Mg-Ni Piston Alloy," *Materials*, vol. 11, no. 7, p. 1230, Jul. 2018. [Online]. Available: http://www.mdpi.com/1996-1944/11/7/1230

[64] A. Bhowmik, Y. Yang, W. Zhou, Y. Chew, and G. Bi, "On the heterogeneous cooling rates in laser-clad Al-50Si alloy," *Surface and Coatings Technology*, vol. 408, p. 126780, Feb. 2021. [Online]. Available: https://linkinghub.elsevier.com/retrieve/pii/S025789722031450X

[65] E. Ghassemali, M. Riestra, T. Bogdanoff, B. S. Kumar, and S. Seifeddine, "Hall-Petch equation in a hypoeutectic Al-Si cast alloy: grain size vs. secondary dendrite arm spacing," *Procedia Engineering*, vol. 207, pp. 19–24, 2017. [Online]. Available: https://linkinghub.elsevier.com/retrieve/pii/S1877705817354346

[66] "Thermodynamics Software." [Online]. Available: https://thermocalc.com/products/thermo-calc/

[67] Y. Zhang, N. Mattern, and J. Eckert, "Study of direct relationship between atomic structures and glass forming abilities of Cu $_{100-x}$ Zr $_{x}$ (0x10) liquids by molecular dynamics simulations," *Journal of Applied Physics*, vol. 111, no. 5, p. 053520, Mar. 2012. [Online]. Available: http://aip.scitation.org/doi/10.1063/1.3693303

[68] T. Pinomaa, M. Lindroos, P. Jreidini, M. Haapalehto, K. Ammar, L. Wang, S. Forest, N. Provatas, and A. Laukkanen, "Multiscale analysis of crystalline defect formation in rapid solidification of pure aluminium and aluminium–copper alloys," *Philosophical Transactions of the Royal Society A: Mathematical, Physical and Engineering Sciences*, vol. 380, no. 2217, p. 20200319, Feb. 2022, publisher: Royal Society. [Online]. Available: https://royalsocietypublishing.org/doi/full/10.1098/rsta.2020.0319

[69] Y.-F. Mo, R.-S. Liu, Y.-C. Liang, H.-T. Zhang, Z.-A. Tian, Z.-Y. Hou, H.-R. Liu, L.-L. Zhou, P. Peng, and T.-H. Gao, "Formation and evolution of nano-clusters in a large-scale system of Cu–Zr alloy during rapid solidification process," *Computational Materials Science*, vol. 98, pp. 1–9, Feb. 2015. [Online]. Available: https://linkinghub.elsevier.com/retrieve/pii/S0927025614007058

[70] A. Mahata, M. A. Zaeem, and M. I. Baskes, "Understanding homogeneous nucleation in solidification of aluminum by molecular dynamics simulations," *Modelling and Simulation in Materials Science and Engineering*, vol. 26, no. 2, p. 025007, Feb. 2018. [Online]. Available: https://iopscience.iop.org/article/10.1088/1361-651X/aa9f36
[71] M. I. Mendelev, F. Zhang, Z. Ye, Y. Sun, M. C. Nguyen, S. R. Wilson, C. Z. Wang, and K. M. Ho, "Development of interatomic potentials appropriate for simulation of devitrification of Al $_{90}$ Sm $_{10}$ alloy," *Modelling and Simulation in Materials Science and Engineering*, vol. 23, no. 4, p. 045013, Jun. 2015. [Online]. Available: https://iopscience.iop.org/article/10.1088/0965-0393/23/4/045013
[72] P. H. Steen and C. Karcher, "FLUID MECHANICS OF SPIN CASTING OF METALS," *Annual Review of Fluid Mechanics*, vol. 29, no. 1, pp. 373–397, Jan. 1997. [Online]. Available: https://www.annualreviews.org/doi/10.1146/annurev.fluid.29.1.373
[73] J. W. Mattson, "On the production of crystalline and noncrystalline metals via the planar flow casting process," 2019.
[74] E. A. Theisen and S. J. Weinstein, "An overview of planar flow casting of thin metallic glasses and its relation to slot coating of liquid films," *Journal of Coatings Technology and Research*, Jul. 2021. [Online]. Available: https://link.springer.com/10.1007/s11998-021-00503-y
[75] H. Fiedler, H. Mühlbach, and G. Stephani, "The effect of the main processing parameters on the geometry of amorphous metal ribbons during planar flow casting (PFC)," *Journal of Materials Science*, vol. 19, no. 10, pp. 3229–3235, Oct. 1984. [Online]. Available: http://link.springer.com/10.1007/BF00549809
[76] H. Yu, "A fluid mechanics model of the planar flow melt spinning process under low reynolds number conditions," *Metallurgical Transactions B*, vol. 18, no. 3, pp. 557–563, Sep. 1987. [Online]. Available: http://link.springer.com/10.1007/BF02654268
[77] C. J. Byrne, S. J. Weinstein, and P. H. Steen, "Capillary stability limits for liquid metal in melt spinning," *Chemical Engineering Science*, vol. 61, no. 24, pp. 8004–8009, Dec. 2006. [Online]. Available: https://linkinghub.elsevier.com/retrieve/pii/S0009250906006130
[78] L. Marot, S. Jakob, M. Martina, P. Reimann, H. Breitenstein, M. Steinacher, and E. Meyer, "Reimann Brake Ramp for planar flow casting processes and analysis of ribbon gluing," *Journal of Materials Research and Technology*, vol. 16, pp. 734–742, Jan. 2022. [Online]. Available: https://linkinghub.elsevier.com/retrieve/pii/S2238785421014095
[79] J. K. Carpenter and P. H. Steen, "On the heat transfer to the wheel in planar-flow melt spinning," *Metallurgical Transactions B*, vol. 21, no. 2, pp. 279–283, Apr. 1990. [Online]. Available: http://link.springer.com/10.1007/BF02664195
[80] B. Bewlay and B. Cantor, "Photocalorimetric cooling rate measurements on 316l-stainless steel rapidly solidified by melt spinning," *International journal of rapid solidification*, vol. 2, no. 2, pp. 107–123, 1986.
[81] G. Stephani, H. Mühlbach, H. Fiedler, and G. Richter, "Infrared measurements of the melt puddle in planar flow casting," *Materials Science and Engineering*, vol. 98, pp. 29–32, Feb. 1988. [Online]. Available: https://www.sciencedirect.com/science/article/pii/0025541688901206
[82] R. C. Ruhl, "Cooling rates in splat cooling," *Materials Science and Engineering*, vol. 1, no. 6, pp. 313–320, 1967.
[83] E. M. Gutierrez and J. Szekely, "A mathematical model of the planar flow melt spinning process," *Metallurgical Transactions B*, vol. 17, no. 4, pp. 695–703, Dec. 1986. [Online]. Available: http://link.springer.com/10.1007/BF02657132
[84] Z. Gong, P. Wilde, and E. Matthys, "Numerical modelling of the planar flow melt-spinning process and experimental investigation of its solidification puddle dynamics," *International journal of rapid solidification*, vol. 6, no. 1, pp. 1–28, 1991.
[85] S. Wu, C. Chen, W. Hwang, and C. Yang, "Analysis for melt puddle in the planar flow casting process—A mathematical modelling study," *Applied Mathematical Modelling*, vol. 16, no. 8, pp. 394–403, Aug. 1992. [Online]. Available: https://linkinghub.elsevier.com/retrieve/pii/0307904X9290074D
[86] C.-W. Chen and W.-S. Hwang, "A modified free surface treatment for the modeling of puddle formation in planar flow casting process," *ISIJ international*, vol. 35, no. 4, pp. 393–401, 1995.
[87] M. Bussmann, J. Mostaghimi, D. Kirk, and J. Graydon, "A numerical study of steady flow and temperature fields within a melt spinning puddle," *International Journal of Heat and Mass Transfer*, vol. 45, no. 19, pp. 3997–4010, Sep. 2002. [Online]. Available: https://linkinghub.elsevier.com/retrieve/pii/S0017931002001126
[88] H. Jones, "The status of rapid solidification of alloys in research and application," *Journal of Materials Science*, vol. 19, no. 4, pp. 1043–1076, Apr. 1984. [Online]. Available: http://link.springer.com/10.1007/BF01120015
[89] E. H. Strange, "Apparatus for making metal strips, foil, sheets, or ribbons," US Patent US993 904A, May, 1911. [Online]. Available: https://patents.google.com/patent/US993904/en
[90] E. Theisen, "Transient behavior of the planar-flow melt spinning process with capillary dynamics," 2006.
[91] N. P. Kovalenko, Y. P. Krasny, and U. Krey, *Physics of Amorphous Metals*, 1st ed. Wiley, Mar. 2001. [Online]. Available: https://onlinelibrary.wiley.com/doi/book/10.1002/3527603174

Part II

Process modelling

2

Planar flow casting model

In this chapter the Python model created to explore the limits of the PFC process will be discussed. An overview of the governing equations is given and the parameters used are presented. Finally the results from this model are presented and discussed.

2.1. Operating window method

Using the properties of the test machine and the material, the limits of the casting process can be calculated. These calculations are done in Python, in order to vary the different parameters. From this, preliminary requirements for the nozzle and control system can be found. In table 2.1 properties and variables used in this model can be found.

Table 2.1: Process parameters, and material properties used for the calculation of the process limits

Parameter	Description	Range/Value
Process properties		
U	Wheel speed	0 – 30 m/s
G	Nozzle/ Wheel gap	0 – 1.0 mm
p	Total pressure	0 – 50 kPa
B	Nozzle slot breadth	1.6 mm
W	Nozzle slot width	0.5 mm
K	Pressure loss factor	2
τ	Ribbon thickness	0 – 0.1 mm
Material properties		
γ	Surface tension	0.821 N/m
ρ	Density	2500 kg/m^3
θ	Contact angle	2.6 rad

From literature it was found that the PFC process is governed by the following parameters or set of parameters, these include the nozzle geometry, gap height, wheel speed, and overpressure. Assuming the nozzle geometry cannot be changed during casting, a model is made using the remaining three parameters. These parameters are variable and are responsible for the hard limits of the process. These limits are calculated according to the process window described by Steen et al [2], and the refinements made by Byrne et al [1], and Li et al [3].

2.1.1. Flow limit

When the capillary pressure in the nozzle or in the gap equals or exceeds the overpressure in the system, no material will flow. The capillary pressure is defined be the Young-Laplace equation, and is at a maximum when the effective radius of the interface is at a minimum. In the PFC process the minimum effective radius is at the point where the fluid passes through the most narrow part of the process. This can be at either the nozzle breadth or the nozzle wheel gap. The minimum overpressure can be defined according to equation 2.1. In this equation θ is the wetting angle, which is dependent on the fluid and the contact material. A value for θ can be found in literature [1] or via melt puddle photography [4][5]. γ is the surface tension of the fluid. These values are assumed to be static. When the pressure is too low to allow for flow into the upstream gap region, air entrapment will occur, leading to a process failure. Therefore this equation sets the limit for the minimum pressure needed to overcome the capillary forces, at a certain gap size.

$$p_{\text{min}} = \frac{2 \cdot \gamma \cos\theta}{\min(W, G)} \tag{2.1}$$

2.1.2. Pressure limit

When the pressure is too high, material will flow upstream, against the motion of the surface of the wheel. This occurs when the overpressure minus the pressure loss in the upstream region of the puddle, is larger than the capillary pressure. Therefore, the maximum overpressure before failure is equal to the pressure loss, plus the capillary pressure, defined according to equation 2.2. The pressure loss of the system is dependent on the flow velocity and the wheel speed U, which is directly related to the ribbon thickness τ and the gap size G. K is defined as the loss factor which is fitted to a particular system and process. K is in the range of 2-3. In the loss factor, variables such as viscosity and thermal expansion of the fluid are captured. The ribbon thickness to gap size ratio (τ/G) is set to 0.16 [1]. This value comes from experiments.

$$p_{\text{max}} = 0.5 \cdot K \left(\frac{\tau}{G}\right)^2 \rho U^2 + \frac{2 \cdot \gamma \cos\theta}{G} \tag{2.2}$$

2.1.3. Wheel speed limit

The final limit of the process is a speed limit. If the wheel speed becomes too high, there is not enough time to transport the necessary amount of heat from the ribbon to the wheel to enable solidification. Furthermore, high speeds can cause instabilities in the fluid flow. The point at which these instabilities occur can be found using the Weber number, which relates a fluids inertia to its surface tension. When the Weber number is high, the fluid flow in a multiphase flow, such as a liquid and gas flow, can become unstable. This instability decreases the heat flow from the liquid to the wheel. The Weber limit for the PFC process is experimentally determined to be 200 [1].

These three limits form the operating window of the PFC process. Within this window, it is possible to produce various ribbon thicknesses by changing the operating parameters within this window. There are multiple parameter combination which will lead to the same ribbon thickness.

2.2. Model

The equations described above are then used to numerically calculate the different limits. A function is used to calculate all relevant equations for all variable combinations. The minimum pressure, maximum pressure, Weber number, and thickness are calculated. The model makes the following calculations:

- Weber number
- Capillary pressure
- Ribbon thickness
- Pressure loss
- Maximum pressure
- Minimum pressure

At first the Weber number We is calculated in equation 2.3, using the density ρ, wheel speed U, surface tension γ, and the gap G.

$$We = \frac{\rho U^2}{2 \cdot \gamma / G} \tag{2.3}$$

Next the capillary pressure p_{cap} is calculated, which is used for the limiting pressure later on. In this equation 2.4 θ is the contact angle between the liquid and the wheel.

$$p_{\text{cap}} = \frac{\gamma \cdot (1 - \cos(\theta))}{G} \tag{2.4}$$

Then the resulting ribbon thickness τ is calculated according to equation 2.5. In this equation p is the total pressure (applied pressure and static pressure) and K is the pressure loss factor.

$$\tau = \frac{G}{U} \cdot \frac{\sqrt{2(p - p_{\text{cap}})}}{(1 + K)\rho} \tag{2.5}$$

In equation 2.6 the pressure loss in the puddle is calculated. T/G is set to 0.16 which is an experimentally determined value [1].

$$p_{\text{loss}} = 0.5 \cdot K \cdot (\tau / G)^2 \rho U^2 \tag{2.6}$$

Finally in equation 2.8 and 2.7 the maximum and minimum pressures are calculated.

$$p_{\text{min}} = p - p_{\text{cap}} \tag{2.7}$$

$$p_{\text{max}} = p - p_{\text{loss}} - p_{\text{cap}} \tag{2.8}$$

The function returns the results of these equation. Now the operateability windows can be created. Two vectors of the variable parameters are created withing the space of interest. For each parameter combination together with the fixed variable, the function is called. The results of the functions are than checked with the operateability limits from equations 2.9, 2.10 and 2.11.

$$We < 200 \tag{2.9}$$

$$p_{\text{min}} > 0 \tag{2.10}$$

$$p_{\text{max}} \leq 0 \tag{2.11}$$

If the results are inside the limits, a pixel will be created which has the thickness value mapped to a green gradient. If the results are outside of this limit, the pixel will be colored according to which limit has been surpassed. The implementation in Python can be found in appendix A.

2.3. Operating window results

Three example parameter spaces are plotted, for a fixed speed, pressure and gap. The fixed parameters are chosen such that a successfully casting is possible, but not necessarily optimal. The other two parameters are varied such that an operating range becomes visible. In the operating range the resulting ribbon thickness is presented with a color gradient.

In figure 2.1 the pressure is set to 15 kPa, whilst the wheel speed and gap are varied. As can be seen from the figure, under these condition the pressure is not high enough to allow for flow through a gap smaller than 100 µm. This area is presented in black. Just above this area at the smallest possible gap, the ribbon is at its thinnest. At low wheel speeds, below 10 m/s, the system quickly becomes pressure limited presented in red, meaning that the pressure will be too large, and the fluid will blow out the left side of the gap. The small slit in which a ribbon is theoretically possible, between the red and black areas, will in practice be of limits due to small variation in gap size and pressure. When moving to higher wheel speeds, 15 m/s, a larger stable area opens up. In this area a gap variation of 500 µm will still result in a successful cast, making this parameter combination an ideal starting point for experimental testing. Moving further to the right by increasing the wheel speed, solidification cannot occur any longer and the area is of limits again, presented in blue. A second observation that can be made is that the ribbon thickness decreases with increasing wheel speed as well.

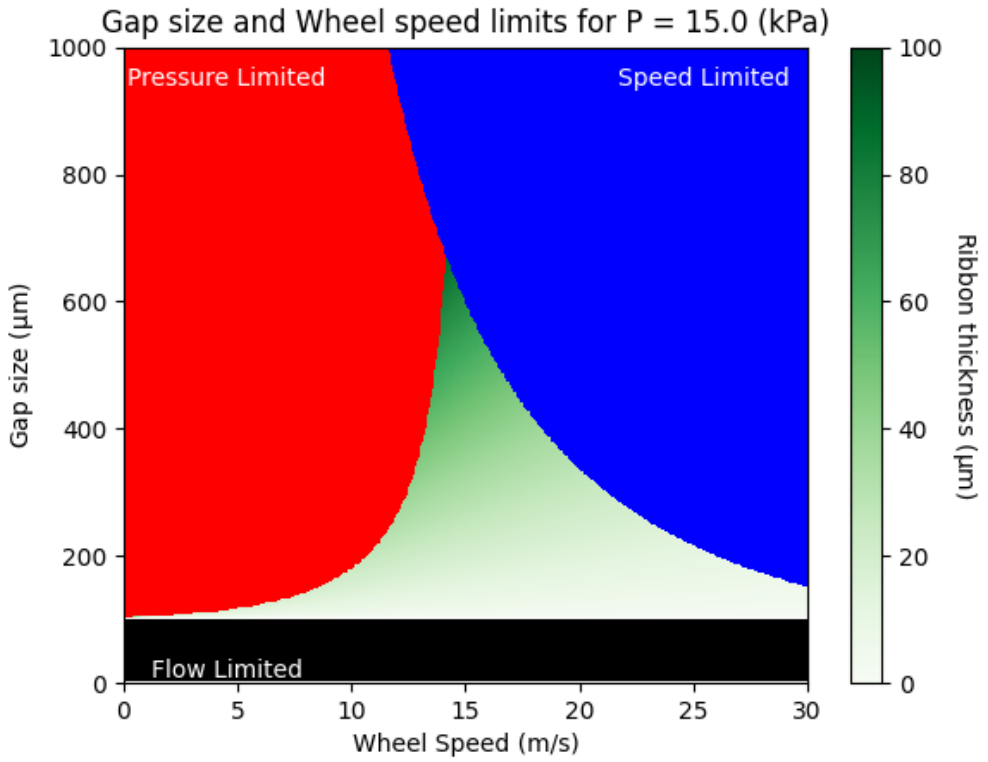

Figure 2.1: Operating range under constant pressure. The green gradient represents the resulting ribbon thickness. The red area causes a blowout on the backside of the gap. The blue area will not fully solidify the ribbon. In the black area the pressure is not sufficient to allow for flow through the nozzle and/or gap.

In figure 2.2 the speed is set to 15 m/s whilst the pressure and the gap are varied. In this figure it is clear that for a smaller gap, the pressure has to be increased in order to make flow possible. On the other hand at high pressure, blow out can only be prevented by decreasing the gap size. As in figure 2.1 there is a vary narrow region in which casting is theoretically possible but will be near impossible in reality due to variation in gap size caused by vibrations or other disturbances. This is the case for pressures exceeding 20 kPa. From this figure a gap size of 400 µm and a pressure of 15 kPa, will be a good starting point for testing. Leaving ample room for unforeseen variations in both variables. For gap size above 600 µm the wheel speed is to high to completely solidify the ribbon.

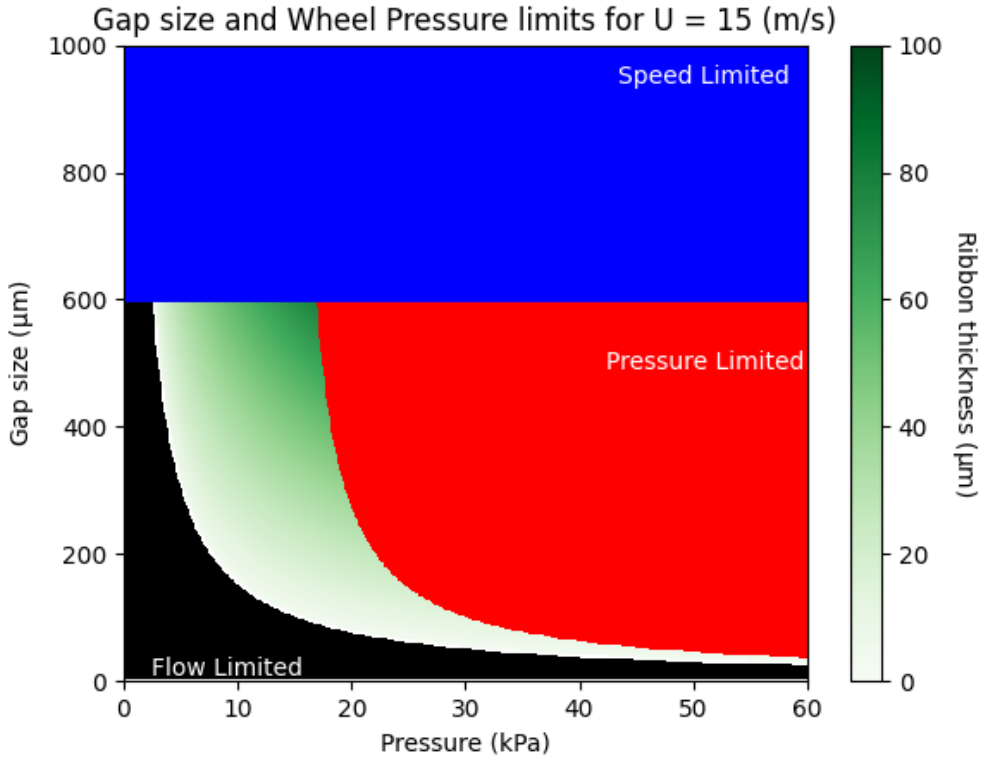

Figure 2.2: Operating range for a constant speed. The green gradient represents the resulting ribbon thickness. The red area causes a blowout on the backside of the gap. The blue area will not fully solidify the ribbon. In the black area the pressure is not sufficient to allow for flow through the nozzle and/or gap.

In the last figure 2.3 the gap is held constant at 500 µm. At this height the wheel speed will be limited to 16 m/s to still allow for solidification. By increasing pressure and wheel speed simultaneously the rate of production can be increased without changing the thickness of the ribbon.

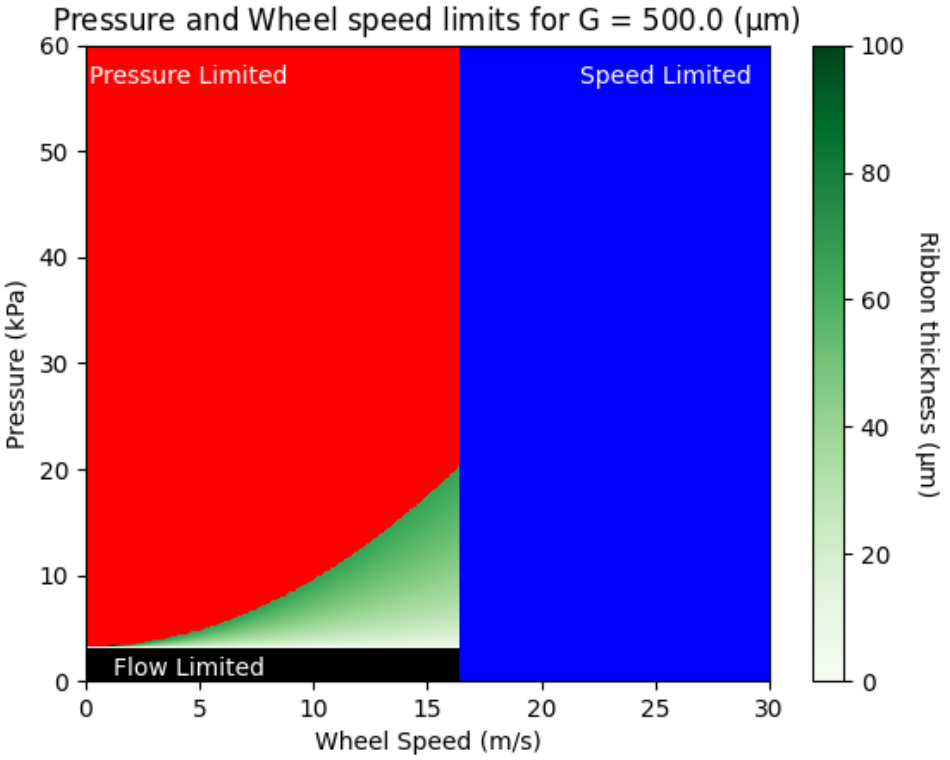

Figure 2.3: Operating range for a constant gap. The green gradient represents the resulting ribbon thickness. The red area causes a blowout on the backside of the gap. The blue area will not fully solidify the ribbon. In the black area the pressure is not sufficient to allow for flow through the nozzle and/or gap.

2.4. Discussion

The model presented in this chapter shows were the limits of the PFC process are, in terms of the three main operating parameters. Similar operating windows are present in literature. However they are often presented with much more information condensed into one figure, requiring a strong background in fluid dynamics in order to interpret them correctly. The figures presented here are based on the same mathematics, but they are presented in such way that is becomes clear what is possible and what is not, and which parameters have what effect on the PFC process. By changing the variables used in the Python model, these figures can be created for different materials, nozzles, and other processing parameters ranges.

The result from this model will be the starting point of the Comsol simulation in the next chapter. Furthermore they will be used for the requirements of the nozzle, sensors and actuators of the test machine. The model is also integrated in the system and control simulation presented in chapter 4.

3

Comsol Simulation

In order to verify the results found with the Python model, a Comsol simulation is made. This simulation will go a step further, by tracking all temperature dependent variables not considered before. Furthermore this simulation serves as an independent verification that is not based on the equation from PFC literature. The simulation will be a coupled fluid and thermodynamics simulation. The fluid dynamics are simulated according to the Navier-Stokes equations for laminar incompressible flow. The heat transfer is simulated for radiation, conduction, and convection.

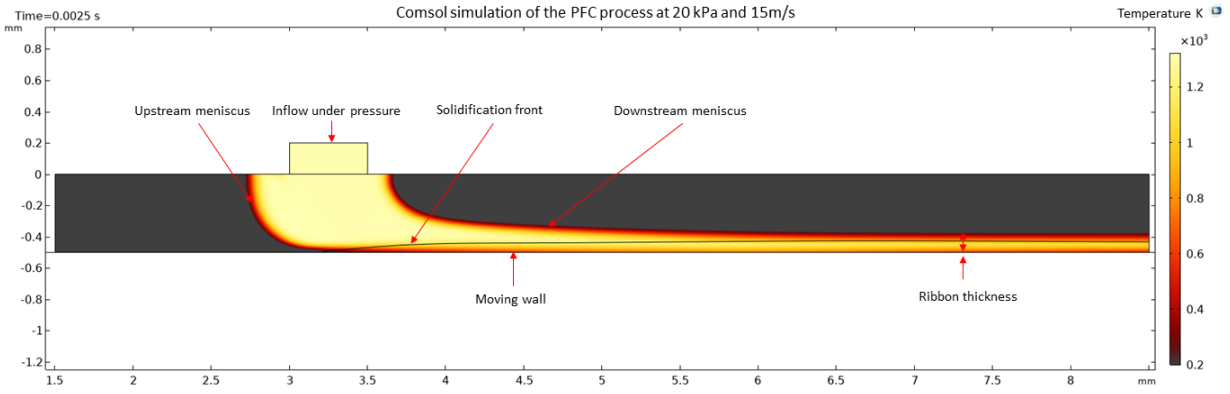

Figure 3.1: Results from a Comsol simulation of the PFC process. Temperature is represented with a color gradient from dark red to yellow. The surrounding air is dark grey. The solidification front is presented as a black line starting at the first contact point with the wheel in the lower left side of the puddle.

In figure 3.1 one of the results from the Comsol simulation is presented. Molten metal flows from the top rectangle, into the gap, rapidly cooling and solidifying when it reaches the bottom moving substrate. This simulation was made using a pressure of 20 kPa, a wheel speed of 15 m/s, and an overheat of 15 K above the melting temperature. This result is 0.025 s after the start of the simulation. Both menisci, the solidification front, the ribbon thickness, and the temperature field can be read from this figure.

This simulation will lack a control system and will only be valid for prescribed and constant values for the gap size, overpressure and wheel speed.

The difficulty with the Comsol simulation is twofold, firstly the solidification process is a highly non-linear process. This causes convergence issues, and requires a fine mesh and small time steps. Secondly, there is no preset Multiphysics coupling available in which all the physics of this problem are represented. To solve a multiphase flow problem, with a moving boundary, either the phasefield or the level set method can be used. These two methods however, do not work in conjunction with the built-in phase change physics. Therefore a workaround is used as presented by Samara et al. [6]. In this method the viscosity of the fluid representing the metal alloy, is made to change rapidly by a factor of 1000 at the melting temperature. This way it is still a fluid, but it acts like a solid for simulation purposes. Similarly, a change in heat capacity at this temperature is used in order to release the latent heat into the system, as would happen with crystallization of the material.

3.1. Methods

The simulation is carried out in 2D, due to the computational requirements of the fluid dynamics calculations. This is valid for a large part of the process, in the direction of the third dimension the size of the nozzle is much larger than the slot breadth. Therefore, effects from the boundaries on the side can be neglected since they are far away from the bulk of the flow. This is in contrast with FFC were the depth dimension is in the same order of magnitude as the nozzle breadth, resulting in are similar large effect from both boundaries. In figure 3.2 The geometry of system as used in Comsol is presented. In this figure the boundary conditions and the initial conditions are marked. In table 3.1 the parameters used by Comsol are presented.

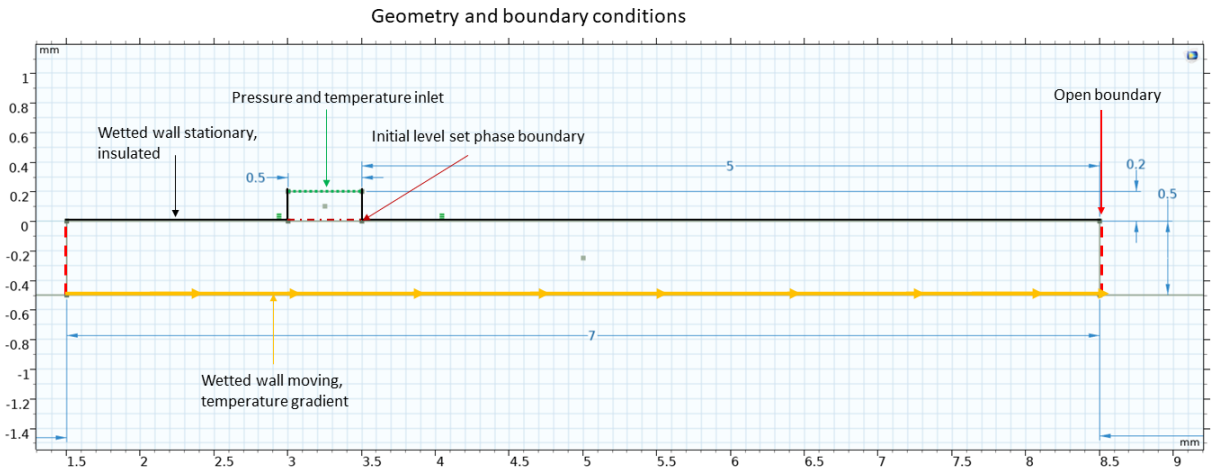

Figure 3.2: Comsol setup, geometry, initial conditions and boundary conditions. The geometry is defined as walls (in black and yellow) and open boundaries (in red and green).

Table 3.1: Material properties of AlSi40 for the Comsol simulation

Property	Description	Value
T_m	Melting temperature	1010 K
ΔT	Melting range	270 K
C_{pl}	Heat capacity liquid	1100 J/(kg·K)
C_{ps}	Heat capacity solid	900 J/(kg·K)
C	Action function constant	10^3
q	Action function constant	10^{-1}
μ_l	Viscosity	1.23×10^{-3} Pa·s
k	Conductivity	237 W/(m·K)
Lf	Latent heat	396 kJ/kg

The general setup of the Comsol simulation is as follows, to keep track of the boundary for the two phase flow, consisting of air and liquid metal alloy, the level set physics is used. This method allows for use in combination with the moving boundary function which is otherwise not possible with a moving mesh setup [7]. The level set method is responsible for the simulation of the capillary physics, which are essential for this process. To accurately model the capillary physics, a contact angle is specified between the boundary of the two phases and the wall. The value for this angle is empirically determined by high speed photography for molten aluminium alloy and a copper surface [1].

In figure 3.2 the geometry and the boundary conditions of the Comsol simulation are presented. The geometry consist of two rectangles, of which the top one is the last part of the nozzle with a width of 0.5 mm. In this rectangle the molten metal is initiated. Therefore, the initial phase boundary between the metal and the air is present at the underside of this rectangle. On the upper side of this rectangle an inlet is

defined with an overpressure, which acts as the external pressure plus the metallostatic pressure in the crucible. This pressure is constant. At this inlet also the temperature of the inflowing fluid is defined, which is constant. The sides of the rectangle are stationary wetted walls, which are insulated so no heat transfer takes place. The second large rectangle represents the space between the nozzle and the wheel, the gap. This space is initially filled with air and has two open boundaries on either side. The top and bottom are wetted walls, of which the top is stationary and insulated. The bottom is moving and allows for heat transfer. The height of the gap is set at 0.5 mm and the length is 7 mm. Depending on the solidification rate, this length might not be sufficient to capture all relevant physics, and has to be increased for slower solidifying systems. Not pictured is a 27 x 5 mm large rectangle below the moving wetted wall presented in yellow. This rectangle is only used as a rudimentary place holder for a heat transfer simulation to the cooled wheel.

The rotating wheel is implemented by the moving wall feature in the Multiphysics coupling feature ”wetted wall”. This feature couples the fluid physics with the multiphase physics. The moving wall imparts a force on the fluid via friction in the boundary layer on top of the boundary that represents this wall. Because only a small part of the moving wheel is simulated, the curved surface can be represented as this straight wall, because the curvature is minimal at this scale. For convergence improvements the wall speed is ramped up as soon as the liquid metal comes in contact with the wall. The other surfaces in contact with the liquid are also designated as wetted walls, but without wall movement.

The parameters used in the Comsol simulation are presented in table 3.1. For the air phase, the built-in material properties are used.

The solidification model is validated by simulating a molten droplet. The results from this simulation show that the droplet solidifies from the bottom up, after which it solidifies from the edges inward. This is expected since most heat is lost on the cold plate, after which most heat is lost to the surrounding air.

3.1.1. Fluid dynamics

The fluid dynamics of both the air and liquid metal are governed by the laminar flow node. Despite the high Reynolds number of the process, it can still be considered laminar due to the stabilizing effect of the solidification process. The liquid metal starts at the top of the nozzle, and is forced through the system with a prescribed pressure. The inflow pressure is set to 15 - 60 kPa. The outflow boundary at both sides of the gap are set to an open boundary.

3.1.2. Heat transfer

For the heat transfer simulation, the temperature of the inflowing fluid is set. Furthermore the initial temperature of the air surrounding melt puddle is set to the temperature of the liquid metal as well. This is done to prevent unrealistic heat conduction through phase boundary from the metal to the air. Due to the nature of the boundary, which averages the material parameters in the boundary area, there is a larger than natural heat loss to the air. This can also be prevented by decreasing the boundary size, this is however more computationally intensive. It can be shown that the heat loss to the air is minimal under these conditions in reality. An important part that is still missing from this simulation is the temperature of the nozzle. This is currently modelled as an insulator, in reality this will have a significant impact on the heat flow from the nozzle trough the liquid metal to the wheel. This is because the nozzle is heated to the same temperature as the liquid metal. The wheel is simulated as a solid block, initially at the temperature of the liquid metal. At the under side boundary of the block a temperature is prescribed which decreases with time in the simulation. In reality the wheel starts cold, this however leads to convergence problems in the simulation due to the extreme temperature gradient which would appear as soon as the liquid hits the wheel. This workaround is chosen because both situation would eventually lead to the same equilibrium state. The solid block captures the heat capacity of the wheel, and allows for a temperature profile to be set up at the boundary between the wheel and the liquid metal. All other boundaries are either insulated or an open boundary at the location of fluid outflow.

The heat flow and the fluid flow are coupled in the non-isothermal flow node. This node allow for a temperature gradient along the fluids.

3.1.3. Solidification

The solidification is modelled using the material properties node. For the liquid metal multiple material properties are set up, such that that they model a change from fluid to a crystallized solid, dependent on the temperature. For the viscosity a differentiable curve is used over the temperature range, defined as the mushy zone, in this range the first phase starts to crystallize in the fluid but the fluid is not fully crystallized yet. At the end of the range, the fluid is completely solid. At this temperature the viscosity is increased a 1000 fold. This has as effect that the velocity gradient present in the fluid, which runs from 0 to the speed of the wheel, from top to the bottom of the fluid, is diminished since in the solid ribbon the velocity profile is uniform. Solidification inserts heat into the system due to the latent heat released by crystallization. This is modelled by decreasing the heat capacity of the material with temperature whilst simultaneously adding heat energy equal to the latent heat of the material. This is done using a Gaussian distribution for the latent heat, spread out over the melting range. The viscosity $\mu(T)$ is modelled according to equation 3.1. In which A is the action function 3.2 which smoothly transitions the viscosity from the liquid value μ_l to the solid value.

$$\mu(T) = \mu_l(1 + A(T)) \tag{3.1}$$

In equation 3.2 the constants C and q are chosen such that the viscosity increases 1000 fold.

$$A(T) = \frac{C(1 - B(T))^2)}{B(T)^3 + q} \tag{3.2}$$

In equation 3.3 the heat capacity $C_p(T)$ change and latent heat L_f addition are modelled accordingly.

$$C_p(T) = C_{ps} + (C_{pl} - C_{ps}) \cdot B(T) + L_f D(T) \tag{3.3}$$

In this equation, B represents the heaveside function as programmed in Comsol (equation 3.4), to transition from the liquid heat capacity C_{pl} to the solid heat capacity C_{ps} over the melting temperature range T_m.

$$B(T) = flc2hs((T - T_m), \Delta T_m) \tag{3.4}$$

D is a Gaussian function (equation 3.5) that guarantees that the latent heat is added to the melt, spread over the melting temperature range.

$$D(T) = \exp\left(\frac{-T(T - T_m)^2}{\Delta T_m}\right) / \sqrt{\pi \Delta T_m^2} \tag{3.5}$$

These equation are implemented according to Samara et al. [6].

To see the phase boundary between the solidified phase and the liquid phase, a plot of the viscosity is made. This is done since Comsol doesn't recognise a phase boundary or different material at this location. Furthermore the temperature is plotted, and the phase boundary between the liquid and the gas.

3.1.4. Mesh

A small mesh is used, with a long rectangular mesh 7 layers deep for boundary flow optimisation flow [8]. The mesh size is chosen to allow for convergence in as little time as possible by balancing calculation time per time step and time step size.

3.2. Results

Four different simulations are made, of which three (in figure 3.3, 3.4 and 3.5) are only fluid dynamics simulations, and one (in figure 3.1) includes heat transfer and solidification. To probe the pressure limit, it is increased from 20 kPa (within the successful ribbon space) to 30 kPa (just above) and 60 kPa. Furthermore the speed is increased from 15 m/s to 25 m/s. The simulations with a pressure below the blowout pressure results in a puddle which stays in place on top of the wheel, from which a thin layer of liquid is pulled along the direction of the wheel. On the left a meniscus can be seen, keeping the liquid from reaching the left boundary. In the simulation with heat transfer and solidification, the liquid starts to solidify from the bottom, increasing in height with distance to the right. The thickness of the ribbon formed can be found in table 3.2. When the liquid starts to solidify, the velocity profile in the ribbon changes. Before solidification, the velocity profile is increasing from top to bottom, until it reaches the boundary layer where the velocity is equal to the wheel speed. This will result in a decreased mass flow rate as compared with a solidified ribbon. Therefore, when solidification starts, mass flow rate increases and the puddle size shrinks. A cooling rate of $2 \cdot 10^5$ K/s can be determined by dividing the length over which solidification takes place with the wheel speed, and dividing the decrease in temperature with this time.

Table 3.2: Comsol results

Pressure	Wheel speed	Ribbon thickness
30 kPa	15 m/s	150 µm
60 kPa	15 m/s	Unsuccessful
20 kPa	25 m/s	80 µm

In figure 3.3 the parameters are chosen to allow for maximum room for error

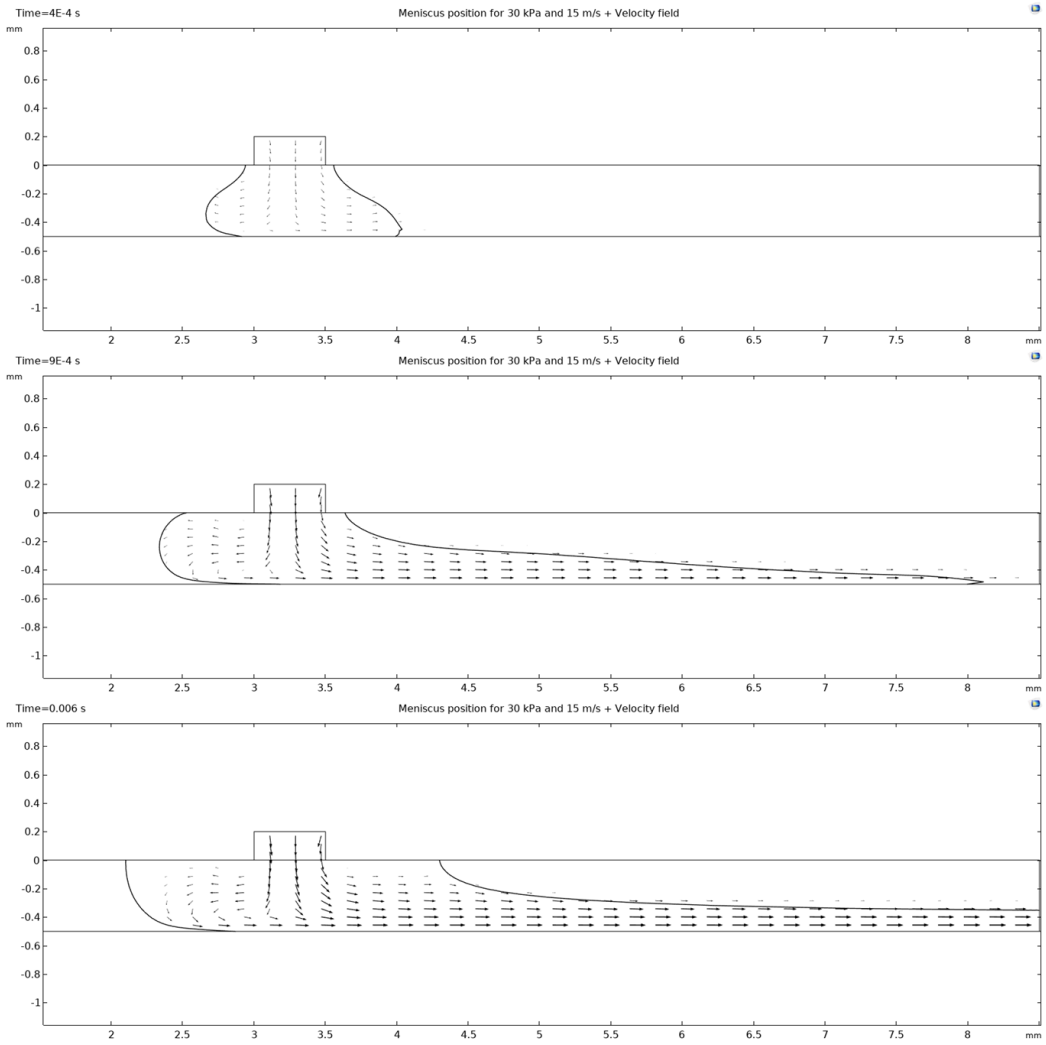

Figure 3.3: Menisci positions and flow field for 30 kPa and 15 m/s at intervals: 4E-4 s, 9E-4 s, and 0.006 s. Puddle stays on top of the wheel and forms a ribbon of 150 µm.

In figure 3.5 the pressure is increased in order to force a blowout.

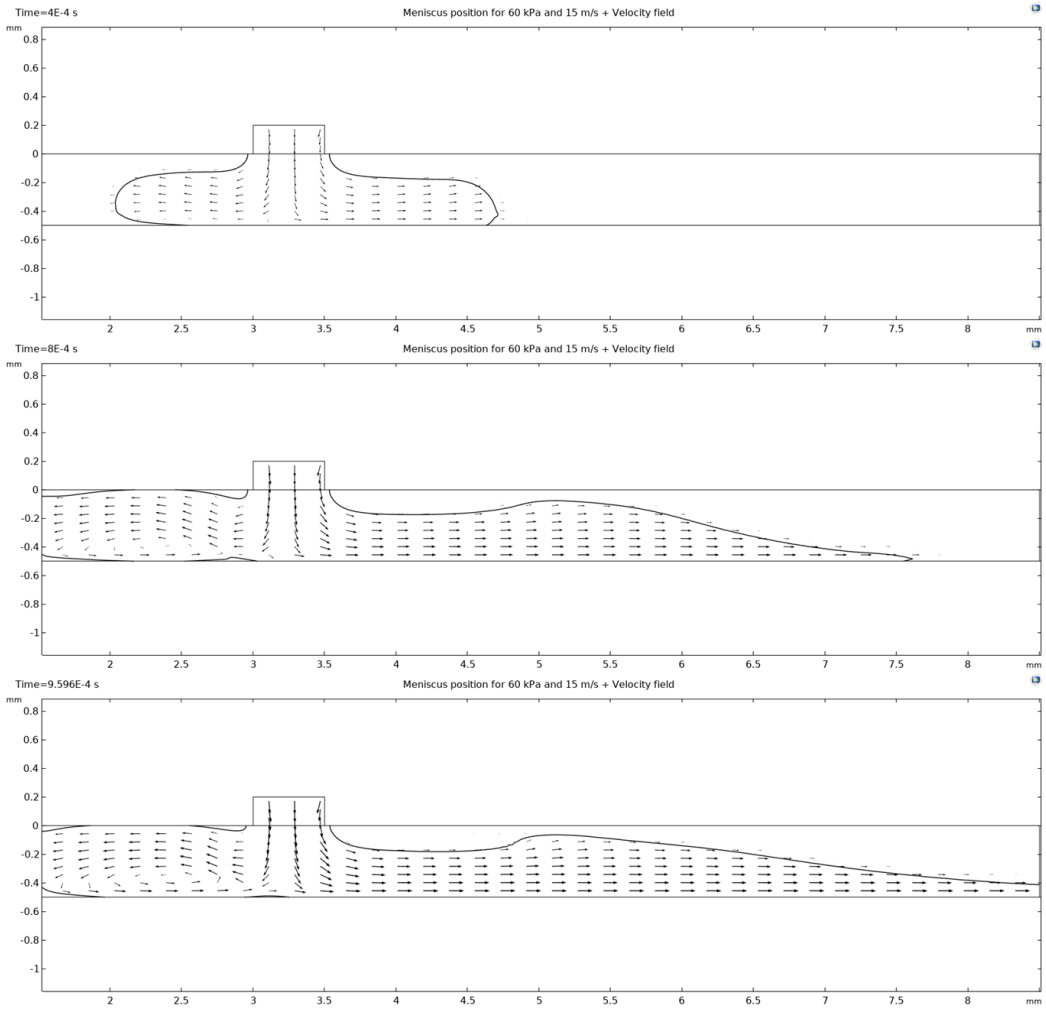

Figure 3.4: Menisci positions and flow field for 60 kPa and 15 m/s at intervals: 4E-4 s, 8E-4 s, and 8E-4 s. At this pressure the fluid leaves the simulation at the left boundary. The speed of the wheel is not sufficient to keep the puddle on top of the wheel.

Finally the wheel speed is increased from 15 m/s to 30 m/s at 20 kPa pressure.

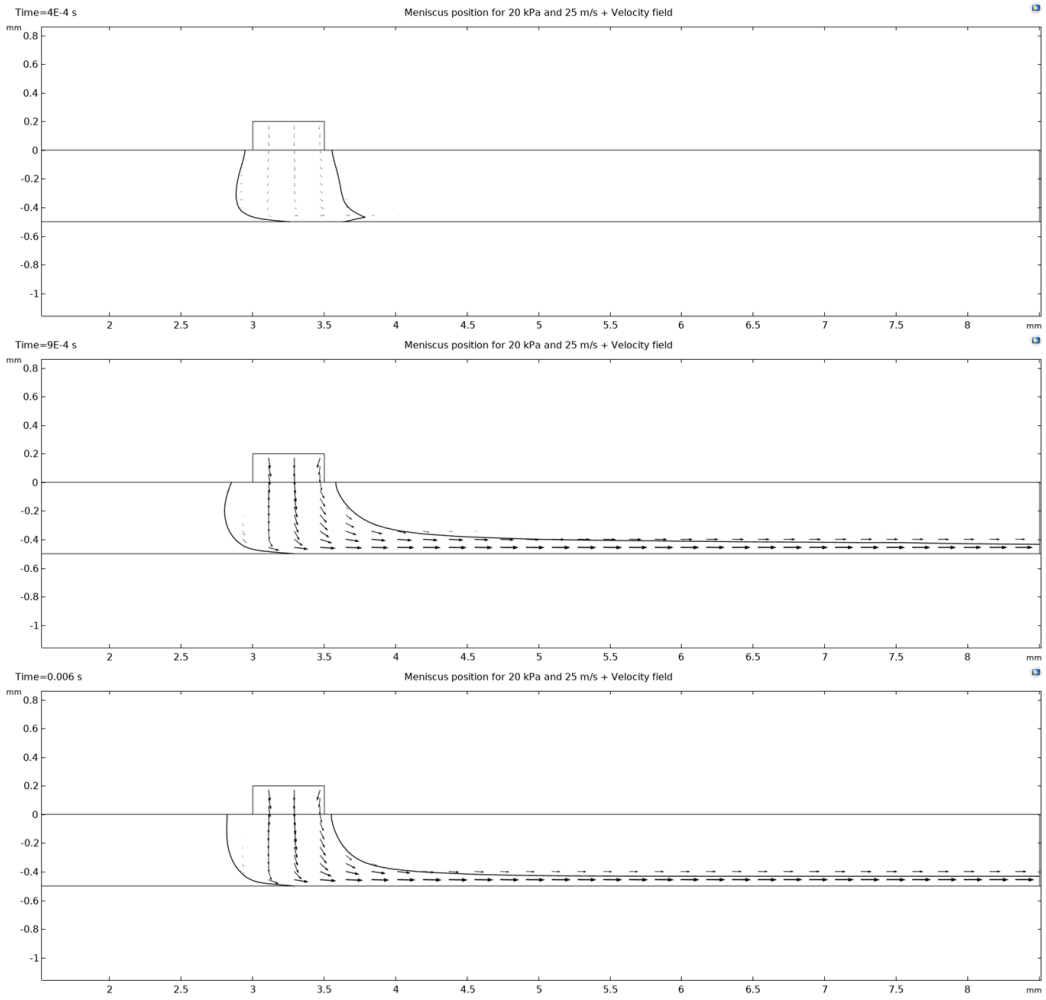

Figure 3.5: Menisci positions and flow field for 20 kPa and 25 m/s at three different intervals. At increased speed the ribbons becomes significantly thinner.

3.3. Discussion

The results found are comparable to the model presented in chapter 2, experimental results [9] and other simulation results from literature [10]. Ribbon thickness, cooling rates, and the operating parameters, all fall within the same order of magnitude as values expected from literature. The most significant difference found, is the pressure at which blow out occurs. An extra increase in pressure was made, since at 30 kPa no blow out occurred as expected. Therefore a pressure of 60kPa was tested. It is evident from figure 3.4 that at 60 kPa blow out does occur, and that therefore the limit according to the simulation must lie somewhere between 30 kPa and 60 kPa. A limit higher than expected from earlier calculations but within a reasonable margin (same order of magnitude). This difference can be explained by the difference between the simulation and the setup in reality. In the real system, disturbances are present that are not simulated, these include, vibrations, pressure variation, gap size variations, wheel speed variations, and material properties that are dependant on temperature. In the simulation these values are assumed to be static, or have a simplified linear relation. This means that the simulation is an idealized situation in which the process is more stable than in reality. Furthermore, the model that is used for the calculation of the parameter space is fitted to the experimental data, by means of the pressure loss factor. This factor is responsible for the determination of the pressure limits of the system. The results found with this simulation are an overestimation of the limits of the real system.

The presented results can be used to estimated the ribbon thickness as a function of the input parameters and the cooling rate of the real system. This in turn can be used in the prediction and analysis of the microstructure of the material.

Ideally more simulations have to be made, that include heat transfer and solidification. However, with these features enabled, at a certain point in the simulation, around 0.006 s, mathematical artefacts show up. These artefacts present themselves as the metal phase appearing out of nowhere in the right upper corner of the simulations area. These particles or blobs are computationally demanding and slow the simulation down 1000 times. The cause of these artefacts lies in the mathematics governing the heat transfer due to convection in rapidly moving flows. The exact nature of this problem is not further explored and a quick solution was not found. To circumvent this problem, solidification is turned off for a number of experiments, for instance to check for different values of the parameter space. This does decrease the reliability of the results since they do not include all relevant physics.

Other difficulties in the simulation are related to the large gradients in temperature and viscosity. These gradients exist between the two fluids, the fluid and the solid, and the wheel and the solid. These gradients can be decreased by increasing the boundary thickness, but this comes at a cost of accuracy, and has other undesired effects. Since the properties of the material are averaged over this boundary, unrealistic heat flow will occur over this boundary when it is too large. Another effect is that the meniscus position is not clearly defined with a large boundary. Therefore a balance is sought between accuracy and simulation time, by adjusting the boundary, temperature difference between the wheel and the fluid, and the viscosity increase upon solidification.

The limiting factor of the Comsol model is the decreasing time step when solidification occurs. Optimizations need be sought in the area of the nonlinear viscosity. Maybe another approach is needed to simulate solidification, since the original paper also struggles with long simulation times. This simulation is even more nonlinear than their problem.

The Comsol model only includes all necessary physics to simulate the PFC process for fixed parameters. To further improve the accuracy and realism of the simulation, variable parameter for the gap, pressure wheel speed can be used. By using variable geometry, the gap size changes caused by vibrations, thermal expansion and machine adjustments can be modelled. Furthermore the control system modelled in Python could be implemented in order to verify its abilities during casting.

Another improvement would be to extend the cooling wheel simulation. The cooling wheel is externally cooled by water. The wheel increases in temperature every rotation until an equilibrium is reached, with a certain temperature profile on the wheel. This can be simulated by applying a velocity to the solid block. this way the temperature field can move or rotate with the wheel. By extending the length of the block the cooling effects of the water can be simulated. Finally the right side temperature profile is used as an input for the left boundary temperature profile.

The final improvement that can be made is to simulate the heat transfer from the nozzle to the melt puddle. Currently the nozzle is insulated, but in reality a significant heat flow exist between the nozzle and the wheel through the melt puddle. This is an important difference when compared with the FFC process where the nozzle and the melt puddle are not in contact.

To overcome the time constraints due to long simulation times, multiple parameter variations of the model could be simulated parallel on a cluster.

These adjustments would lead to a simulation as close to reality as possible but might also be unnecessarily complex and time consuming. Focusing on decreasing simulation time would have priority, in order to simulate multiple different variable combination.

4

System and Control

In this chapter a control system is presented, to control the ribbon thickness of the PFC process. The control system includes the plant, which is based on the model presented in chapter 2. The model is extended to include thermal expansion of the cooling wheel, and gap variations due to out of roundness of the wheel. Furthermore the crucible above the meltspinner is modelled as a spring damper system. The controller used is a PID controller. The controller uses an error signal that is calculated by the difference between a ribbon thickness setpoint value and the ribbon thickness calculated with the pressure and gap sensor input data. The output signal of the controller is used by the actuator to apply pressure to the crucible. This actuator is modelled to have a certain delay and maximum pressure it can deliver. The sensors are modelled to have a sampling time and a certain accuracy.

4.1. The system

Using the operation limits, requirements for a control system can be defined. For the most relaxed requirements, a point is chosen in the middle of the green area in each of the graphs from figure 2.3, 2.1 and 2.2. This results in a gap size of 300 µm, a wheel speed of 15 m/s, and an overpressure of 15 kPa. With these parameters, the gap can vary from 150 to 600 µm, the pressure from 5 to 120 kPa, and the wheel speed from 13 to 16 m/s, whilst still successfully casting a ribbon. These large variations are only possible assuming two of the three variables stay constant. In reality all three variables will vary at the same time, which requires tighter tolerances than the extremes described above. Furthermore, a successful casting is only the first step to have full control over the ribbon thickness during the process.

With the process limits in mind, and a starting point for the controllable variables, a sensor and control system can be modelled. This model consists of a controller, actuator, the system itself, and data acquisition. Each part is modelled separately. This model will couple the system requirement to the ribbon thickness. Using limits and disturbances on each individual part, insight can be gained on the effects on the thickness of the ribbon. What follows is a description of all the modelled parts. Values for the parameters used in the model a presented in table 4.1 and 4.2. A block diagram of the control system is presented in figure 4.1.

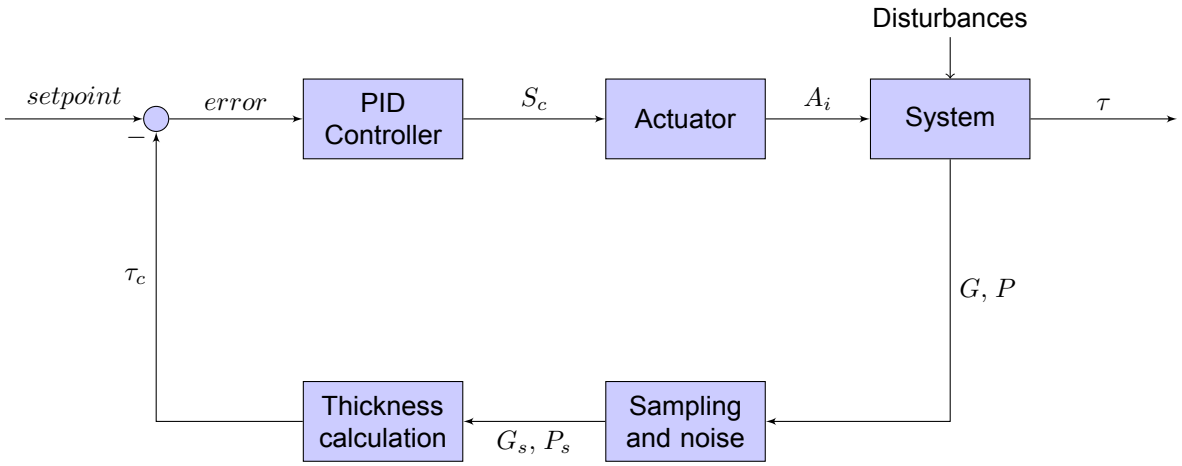

Figure 4.1: Control system block diagram. Each block is a modelled part of the system. The arrows represent the signal or output from each block. The output is then used by the next block or presented in the control system response.

4.2. The plant

The plant is modelled as a spring damper system. The compressed gas above the incompressable liquid metal acts like a spring. The liquid metal forced through the nozzle and the gap, acts like the damper of the system. The system is actuated by an external pressure source. The pressure essentially compresses the spring, in order to push the liquid metal trough the nozzle. This spring is variable, because the volume of gas increases with a decreasing amount of liquid in the system. The temperature of the gas is assumed to be constant, but can in reality vary and have an effect on the pressure inside of the crucible.

When the liquid metal drains from the system, the metallostatic pressure decreases. The speed at which the metal drains, is calculated by multiplying the wheel speed with the ribbon thickness. Because the mass flow out of the crucible, must be equal to the mass flow out of the system through the ribbon, see equation 4.3. This can be done assuming the density stays constant when the metal solidifies and the cast is successful, so no liquid metal spills off the wheel.

The flow through the system, and thus the ribbon thickness, are in turn dependent on the resistance to the flow caused by the gap and nozzle. Therefore the disturbances on the size of the gap have to be modelled. These consist of the thermal expansion of the system, and a periodic oscillation due to the out of roundness of the wheel. The thermal expansion of the wheel can be calculated by assuming that in order to solidify, the ribbon needs to loose the overheat, and the excess energy from the phase transition, the latent heat, as can be seen in equation 4.2. In reality the ribbon can loose more energy to the wheel.

This simplifications circumvents the need for a heat transfer coefficient between the wheel and the alloy which can be difficult to establish. The wheel in turn is cooled by cooling water with a constant temperature. The heat flow to the cooling water will increase with an increasing temperature of the wheel, until the heat flow into the wheel is equal to the heat flow out, as defined by equation 4.4. The expansion of the wheel is then calculated using the geometry of the wheel and the thermal expansion coefficient of the material of the wheel, as defined by equation 4.6. At this point the system reaches equilibrium and the wheel will not expand further. The thermal expansion of the wheel has a stabilizing effect on the system, since it decrease the metal flow through the system which in turn decreases the heat flow to wheel and thus the expansion. This means that without control this effect would not lead to a thermal runaway event.

The disturbance of the wheel is the periodic change in gap sized caused by the out of roundness of the wheel. Since the exact shape of the wheel is not known, the out of roundness is modelled using a sinusoidal change in the gap size with a factor between 0.9 and 1.1, with the same frequency as the wheel.

Other disturbances that are present in the system but are not modelled include: Inertial vibrations caused by the interacting of the inertial forces and the surface tension forces [11], and other vibration present in the system, from the electric motor, pumps or other external sources.

Table 4.1: Thermodynamic properties

Parameter	Description	Range/Value
Cp_{al}	Specific heat aluminium alloy	938 J/kg·K
T_m	Melting range	400 K
T_{wheel}	Wheel Temperature	295 – 400 K
T_{water}	Water Temperature	275 K
ρ_{AlSi}	Density aluminium alloy	2500 kg/m^3
Lf	Latent heat	396 kJ/kg
Cp_{wheel}	Specific heat wheel	385 J/kg·K
M_{wheel}	Wheel mass	100 kg
$\dot{V}_{water}$	Water flow rate	0.0005 m^3/s
H_w	Heat transfer coefficient	$4.5 \cdot 10^2$ W/(m^2 K)
A	Heat transfer area	1 m^2
r_0	Wheel radius	0.3 m

4.3. Sampling and noise

The limits of the controller are in part determined by the accuracy and speed of the sensors. This is implemented by sampling only every 64 values from the numeric simulation, and randomly adding noise to these values. This results in a sampling frequency of 15 Hz. For the pressure sample a random value between -50 and 50 kPa is added, and for the gap between -10 and 10 µm.

With the noisy pressure and gap values, a ribbon thickness is calculated by rewriting equation 2.2 to ribbon thickness. The difference between this value and the setpoint value, is then used as the error for the PID controller.

4.4. Actuator and controller

The PID controller is a standard controller quickly tuned for sufficient results, and not further optimized. In table 4.2 the values for K_p, K_i and K_d can be found.

The signal from the controller is then used by the actuator to exert pressure on the system, the actuator cannot change the pressure instantly but has a delayed and smoothing reaction simulated by averaging the set pressure with the a number of previous pressure values. Since the actuator represents a physical device, it will be limited by a maximum pressure it is able to deliver, or release from the system at one time. These limitation are build in by cutting these values at a maximum per time step.

4.5. Model

The control model works in a similar fashion as the PFC model, with a few added features. The model is now time dependent, with fixed starting values. Therefore, a function is setup to calculate the system state each time step, with the variable values from the previous time step. Each time step the following calculations take place:

- Wheel temperature
- Gap
- Ribbon thickness
- Static pressure
- Spring constant
- Total pressure
- Outflow

Table 4.2: Control system parameters

Parameter	Description	Range/Value
Signals		
S_c	Control signal	
A_i	Actuator input	0 – 50 kPa
τ	Ribbon thickness	0 – 1.0 mm
G	Gap	0 – 1.0 mm
p	Pressure	0 – 50 kPa
G_s	Sampled gap	0 – 1.0 mm
P_s	Sampled pressure	0 – 50 kPa
τ_c	Calculated thickness	0 – 1.0 mm
PID Controller		
K_p	Proportional gain	6E6
K_i	Integral gain	1E5
K_d	Derivative gain	5E6
Disturbances		
OOR	Out of roundness	10 µm
f	Wheel frequency	10 Hz
α	Thermal expansion	16.5 m/(m ·k)
N_G	Uniform noise on gap measurement	10 µm
N_G	Uniform noise on pressure measurement	100 Pa
t_s	Sampling interval	1/64

The wheel temperature T_{wheel} is calculated by taking the temperature at the previous time step $(t-1)$ and adding the temperature change δT according to equation 4.1.

$$T_{wheel} = T_{wheel}(t-1) + \delta T \tag{4.1}$$

To calculate the temperature change, first the heat flow in and out of the wheel have to be known. The heat inflow can be calculated according to equation 4.2 using the mass flow $\dot{M}$, Latent heat L_f, the density ρ_{AlSi} and specific heat capacity of the alloy Cp_{al}.

For the temperature change, a function is called dependent on the previous temperature, wheel speed and ribbon thickness, and is calculated according to the equations: 4.3, 4.2, 4.4, and finally 4.5.

$$Q_{in} = \dot{M} \cdot \rho_{AlSi} \cdot (T_m \cdot Cp_{al} + L_f) \tag{4.2}$$

The mass flow out of the crucible 4.3 is equal to the wheel speed U times the thickness of the ribbon τ. The thickness is calculated according to the equation presented in the previous chapter 7 in equation 2.5.

$$\dot{M} = \tau \cdot U \tag{4.3}$$

To calculate the heat flow out of the wheel, the temperature difference between the cooling water and the wheel is multiplied with a heat transfer coefficient and the heat transfer area.

$$Q_{out} = AH_w(T_{wheel} - T_{water}) \tag{4.4}$$

To determine the temperature change of the wheel, the net heat flow is divided by the mass of the wheel M_{wheel} multiplied with its heat capacity Cp_{wheel}.

$$\delta T = \frac{Q_{in} - Q_{out}}{Cp_{wheel} M_{wheel}} \tag{4.5}$$

Finally the new temperature can be found by adding the temperature change to the previous temperature.

The following variable is the gap size. The gap size is dependent on the expansion of the wheel due to temperature and the out of roundness of the wheel. Using equation 4.6 the decrease in gap size due to the expansion of the wheel is calculated. In this equation α is the thermal expansion coefficient of the wheel and r_0 is the radius of the wheel at the initial temperature. δr is the change in wheel radius and can later be used to find the change in gap size.

$$\delta r = 2\pi \cdot \alpha \cdot r_0 \cdot \delta T \tag{4.6}$$

Next the periodic oscillation due to the out of roundness OOR of the wheel is applied. Without knowing the true geometry of the wheel it is simplified to a a sine function with a frequency and amplitude, and is calculated according to equation 4.7. The amplitude is the difference between the high side of the wheel and the low side. The frequency f is determined by the speed of the wheel. t is the simulation time

$$Disturbance = OOR \cdot \sin 2\pi \cdot f \cdot t \tag{4.7}$$

Using the expansion of the wheel and the disturbance from the out of roundness, the gap size can be calculated.

Next using the outflow determined in equation 4.3 the static pressure is decreased. At the same time the spring factor is adjusted according to the outflow.

When all the variable are set, the applied pressure from the actuator can be determined. This is done by modeling the controller, actuator and data acquisition. The following steps will be taken:

- Sample the pressure and gap data
- Add noise to the data
- Calculate the ribbon thickness
- Apply the controller
- Apply the actuator
- Apply the actuator to the plant

The data is sampled by only using gap and pressure data of every 64th time step. To these values, random noise is added. The range of the created noise is set to 10 µm for the gap data, and 0.1 kPa for the pressure data. These noise level are well within the capabilities of modern measuring equipment.

The ribbon thickness is calculated again using the equation presented in the previous chapter 7 in equation 2.5.

The controller can now use this value to determine the error with respect to the setpoint.

In the actuator function the control signal is cut off at the maximum pressure the actuator can provide each time step. This value is set to 300 Pa. Furthermore, the actuator dynamics are taken into account. This is done averaging the new pressure with older values.

The PID controller function operates as follows: Each time step the error e accumulates in the integral variable i, the derivative variable d is the difference between the current error and the previous error. Finally these values are multiplied by the K_i and K_d factors and the error itself with the K_p factor. The output of the control system can then be defined according to equation 4.8

$$Output = K_p \cdot e + K_i \cdot i + K_d \cdot d \tag{4.8}$$

Finally the output of the actuator is added to the pressure in the plant. Completing the loop for one time step. For the whole simulation, all the previous functions are ran trough a loop, and all the intermediate results are saved. These results are then plotted and presented in figures 4.2 and 4.3. The complete implementation in Python can be found in appendix B.

4.6. Results

To verify the system, two plots are provided, one controlled in figure 4.2 and one uncontrolled in figure 4.3. By comparing these plots the effect of the controller can be observed. In the controlled plot in figure 4.2 The oscillating gap causes a similar oscillation in the ribbon thickness. The response of the system can be observed by the step function in the gap size. A step increase of the gap at 5 s, and a step at 10 s decreasing the gap. These steps represent a gap setting change in the test machine which has a minimal step value of 50 µm. When a major disturbance presents itself, such as the change in gap size, the ribbon thickness slightly overshoots the setpoint. These steps also show the overshoot of the system and the damped oscillation of the PID controller. The red dots represent the sampled data point of the system, whilst the blue lines represent the ”real” system. The effects of the actuator can be seen by comparing the control signal with the actuator signal. Here it can be seen that the actuator signal has a cutoff at the start and at the two steps. The control signal rapidly changes due to the oscillations in the wheel and the disturbances of the measurements. These are limited and smoothed by the actuator, which cannot react quick enough to exactly follow this signal. In the uncontrolled plot in figure 4.3, the effect of the decreasing pressure and decreasing gap size due to temperature can be seen. The control signal and actuator input are none in the uncontrolled system. In this graph the pressure of the system is declining due to the emptying of the crucible. The ribbon thickness is oscillating and generally declining, due to the decrease in pressure. The ribbon thickness does follow the step that is made with the gap.

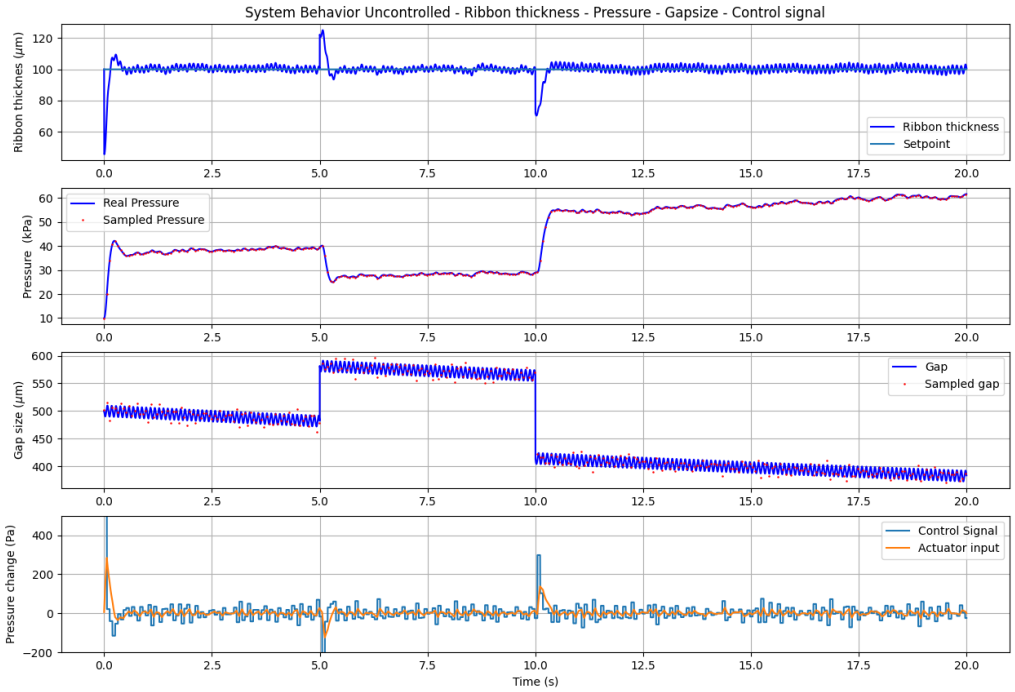

Figure 4.2: Controlled system response. From top to bottom: In the first plot the ribbon thickness (dark blue), compared with the setpoint for the ribbon thickness (light blue). In the second plot the pressure (blue) and the simulated measured pressure (red dot). In the third plot the gap (blue) and the simulated measured gap (red dot). In the last plot the control signal (blue) and actuator input (orange)

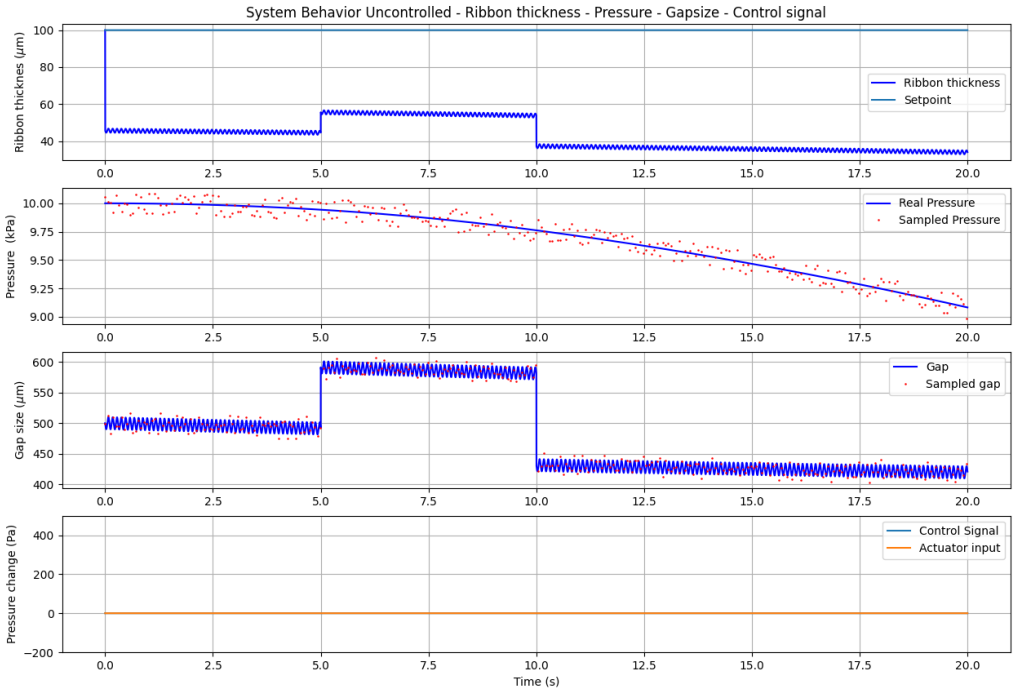

Figure 4.3: Uncontrolled system response. From top to bottom: In the first plot the ribbon thickness (dark blue), compared with the setpoint for the ribbon thickness (light blue). In the second plot the pressure (blue) and the simulated measured pressure (red dot). In the third plot the gap (blue) and the simulated measured gap (red dot). In the last plot the control signal (blue) and actuator input (orange)

4.7. Discussion

The system and control model shows the effect of various disturbances on the resulting ribbon. It provides insight into the controllability of the system. With the use of this model it becomes clear what is feasible with the current setup and chosen sensors and actuators. It is however still a model and has to be tuned to the actual machine. The ribbon thickness calculated by the controller uses the same equations as the plant uses for updating the system. Therefore the results are very accurate. The thickness calculation uses assumptions such as the pressure loss factor which might not be exactly the same as the pressure loss in the real system. By tuning these parameter during experimentation, the model can become an accurate description of the test machine, and the controller will be able to properly control the system. The PID controller used, is a simple one, and is not necessarily the best option for this machine. The controller itself can be better tuned, or a more complex or different controller could be used. A simplified heat flow model is used. A more sophisticated model for the heat flow from the alloy to the wheel is needed. However this model does capture the effect of the expanding wheel and the equilibrium which will be reached. In practice the equilibrium will be reached at a different time than presented here.

5

Design Requirements

In this chapter the knowledge gained from previous chapters and literature will be used to set the requirements for the nozzle, pressure system, and the gap sensor. Apart from quantitative requirements also qualitative ones will be discussed. The requirements are needed in order to make the necessary changes to the test machine, to make the PFC process possible.

5.1. Sensor

5.1.1. Range, and precision

To make PFC work, the gap size has to be reduced below 0.5 mm. For the best results the gap size has to be stable during the whole process. The effect of the gap on the wheel scales with approximately 1/6, lowering the precision requirements for the gap sensor. The variations in ribbon thickness due to high frequency oscillations are in the order of 5 µm. From chapter 4 it can be concluded that a precision of 10 µm, gives sufficient controllability of the system. The measurement range is set to 0.6 mm to allow from some slack.

5.1.2. Frequency

High frequency disturbances cannot be controlled via pressure control, due to limitations of the actuation system. Therefore this is not the leading requirement on frequency. However, for scientific interest it would be beneficial to measure the disturbances caused by the out of roundness of the wheel. Therefore a requirement is set to measure at least 10 times the frequency of the wheel. Giving a requirement of 0.5 kHz

5.1.3. Requirements

Measuring the gap is problematic due to the environment of the sensor. The sensor must give accurate results under the influence of the following disturbances.

- Dust: The wheel is constantly scraped to keep it clean. This scraping produces dust, of which a large part is vacuumed away. The dust that reaches the environment can influence the measurement of the gap directly, or after some time when components gets covered in dust.
- Thermal radiation: Due to the high temperature of the molten metal, it starts radiating in the infrared spectrum, this can have negative effects on optical systems working is this spectrum. It can also cause components of the measurement system around the metal to heat up and produce wrong results.
- Lighting changes: Just as the thermal radiation, radiation in the visible spectrum can have an effect on an optical measurement system. Light is produced by the glowing hot metal, which can create difficulties for a light based measurement system.
- Temperature change: There will be a temperature gradient on the components of the system once the metal starts flowing and the whole system has to reach a new equilibrium. This will also have an effect on the measurement devices in the vicinity.
- No contact: For ease of use and installation a no contact sensor is preferred. Minimizing wear and tear on the sensor and production machine.

These requirements rule out most distance sensing techniques. Mainly optical techniques are used for this precision and distance range, however due to the environment these are excluded [12]. A promising method is capacitance or eddy current sensing due to the robustness of the technique.

Considering these requirements a potential candidate for a measuring system is capacitance distance measurement. This technique is used in the turbine industry in order to measure the gap between the blades and the turbine housing [13]. This is a hostile environment with very high temperatures and other disturbances. The technique works by measuring the change in capacitance between the sensor and the object at high frequency. This technique works on conductive and insulating materials. However it is not clear what is effect of molten flowing metal is on the sensor. Therefore two things can be done: A test setup in a steady environment like a gutter through which molten aluminium is poured a then measuring the distance to the gutter. Alternatively measurements can be taken just before the puddle on the wheel whilst the sensor is attached to the nozzle.

Another use of this sensor is the monitoring of the wheel wear.

Table 5.1: Sensor requirements

Requirement	Value
Precision	5 µm
Range	0.6 mm
Frequency	0.5 kHz

5.1.4. Implementation

The sensor produces a voltage linearly scaled with the distance of the object measured. Measurements take place at a specified frequency and can be read out with a myDAQ. Since the gap between the nozzle and the wheel need to be measured, the device should be placed such that is measures this gap directly or via a proxy which is in a way directly proportional to the gap. The ideal placement would be attached to the nozzle this however is difficult due to the high temperature of the nozzle, the need for it to be replaced, and an eventual external heating of the nozzle. Therefor the closest position would be to attach is to the same attachment point as were the nozzle is attached and compensate for the nozzle expansion in software.

5.2. Pressure system

The pressure of the fluid expelled through to nozzle, is one of the four main parameters responsible for a successful cast on the planar flow casting machine. The pressure in the fluid is a result of metallostatic pressure from the crucible, the nozzle size and shape, and the gap size. The pressure in the crucible can be controlled by pressurising the crucible with an inert gas. Pressure can be increased trough a regulator allowing for compensation of the decreasing metallostatic pressure with the emptying of the crucible, and for a changing gap size, or different nozzle design. This is a flexible solution allowing for a constant pressure during casting and extra pressure on the nozzle if desirable. Practically this solution comes with a few drawbacks. For pressurisation of the crucible it has to by air tight to a certain degree to allow for pressure to build. The crucible needs to be refillable therefore an airtight hatch would be necessary. This results in a redesign of the crucible. There could also be an increased risk of gas inclusions with a pressurised system. Pressurising molten metal is not without risk. This risk has to analysed and extra precautions around the operating machine have to be taken. The pressure system should be able to at least compensate for the metallostatic pressure loss. Extra pressure is preferred to increase the control speed of the system, to account for step changes in the gap. Therefore a pressure system with the capabilities to deliver 100 kPa overpressure is required.

5.3. Nozzle

The nozzle can be optimized for every specific alloy produced at RSP. This means that the nozzle needs to be changed every time a different alloy is produced, and that multiple nozzles need to be designed. Alternatively a compromise can be sought so only one nozzle has to be used. Flow stability will be the most important factor in nozzle design since it will have the highest impact on ribbon and material quality. Flow stability has to do with the interaction between the nozzle and puddle. When a stable flow is reached, the nozzle can be further improved by optimising for high cooling rate of the ribbon, this will be the same as improving the stability of the flow since this will allow faster rotation of the wheel hence decreasing ribbon thickness and increasing cooling rate. As a final improvement production rate can be looked at. The higher the production rate of the material the cheaper it will be to produce and the more applications of the material will become available. The nozzle width is not a significant factor in ribbon thickness according to Su et al.[14]. The effects of a larger nozzle slot are: easier flow of material out of the nozzle requiring lower pressure for the same volume flow. Unequal thermal expansion of the wheel can have an effect on the shape of the ribbon in transverse direction. The unequal thermal expansion is caused by the fact that the wheel will be hotter in the middle of the puddle than on the edge. Therefore the gap size in the middle of the puddle will decrease more than on the edge causing a concave shape in the ribbon, and a change in grain size of the width of the ribbon. To counteract this effect the nozzle can be shaped concave itself in order to make room for the expansion the wheel in the middle of the puddle. The will give the ribbon a more rectangular cross section, with a uniform cooling rate and grain size throughout. For every alloy there will exist a different optimal shape. It will save a lot of complexity to use a general design which compromises over all the alloys. Since the nozzle is not critical for the functions of the planar flow casting production method, it would be possible to start testing with an existing nozzle. For this a rectangular slotted nozzle would be best suited, and the optimal gap size between the nozzle and the wheel for the specific wheel can be calculated. The nozzle design will therefore have to be based on the outflow pressure and gap shrinkage.

5.4. Discussion

By using the results from previous models, and knowledge of the environment in which casting takes place, requirements could be put on parts of the test machine that need adjustments. A specific nozzle design is not made, since it would require a study on its own. With these adjustments the PFC test machine will be able to produce a ribbon. To check if this ribbon is of better quality and has a high solidification rate, the microstructure of the current material will be quantified in the next chapter.

Part III

Material Science

6

Material Analysis

6.1. Introduction

To analyse the phase composition of the resulting ribbon, XRD, SEM, and EDS are employed. These measurements are then compared to an analytical model for non-equilibrium phase composition and the Scheil equation.

6.2. Sample preparation

To prepare the sample for analysis, it is positioned upright into an hot embedding conductive resin, which is compressed at an elevated temperature to be able to grind and polish the cross section of the ribbon. This process could influence the microstructure of the material since it is in a metastable state. Elevated temperatures could cause grain growth in the specimen. Therefore the size of the grains in the specimen where compared optically with a cold resin based sample, and a sample after hot isostatic pressing. All three samples possess primary silicon crystals with a size in the order of 5 µm, given confidence in minimal grain growths at these temperatures. A changing eutectic composition cannot be ruled out, because there is no comparison made at this level of magnification. After sanding and polishing to 1 µm particle size, the sample was etched with HF10, to enhance the visibility of the sub micrometer features in the SEM. Using the images obtained from this sample, measurements can be taken on the feature size of the eutectic phase.

The etched sample is not suitable for EDS analysis since it effects the composition of the material. The HF etches Al faster the Si, skewing the composition data. Therefore the sample is polished again, losing the feature data, but improving the EDS measurement. Using the EDS, multiple points are measured at two different locations in the sample, furthermore two line scans are made across the boundary of the primary Si phase and the eutectic phase, and a 2D analysis is done.

Finally the sample is analysed using XRD, in order to rule out any non crystalline phases present in the sample. For the XRD measurement, a part of the ribbon is cut that is as flat as possible to minimize any boundary effects at the extremes of the scanner angle. This sample is placed on top of a Si wafer that is calibrated with the XRD machine. Measurements from both sides of the ribbon are taken, and automatically analysed in software.

6.3. SEM

In figure 6.1 multiple images are displayed, each with a higher magnification. Image A is an overview of the ribbon created with an optical microscope. The ribbon is held in a black resin in a steel holder (on top and bottom of the image). A magnified image is taken with the SEM, of the part within the small red rectangle. The image is magnified 5000 times. From this image (C), two distinct areas become visible. A smooth lighter area and a non smooth more detailed area. This area is further investigated by zooming in to a magnification of 30.000. Now it becomes clear that there is a detailed structure present in this area, with feature sizes in the range of 100 nm. In this image the distance between 30 of these features are measured, as displayed in the digitally zoomed in images on the right of the figure.

The microstructure of the material can be deduced from these images. It can be seen that two different phases have formed. The primary Si appears more even in texture and color than the eutectic phase. Zooming in further on the eutectic zone, reveals a secondary structure with feature sizes in the order of 100 nm. These features have a round or cylindrical shape, sometimes described as fibre like [15]. The composition of the individual features is not measured, but it is assumed that these are primary Si, and that the Al-α matrix has been etched away around the Si.

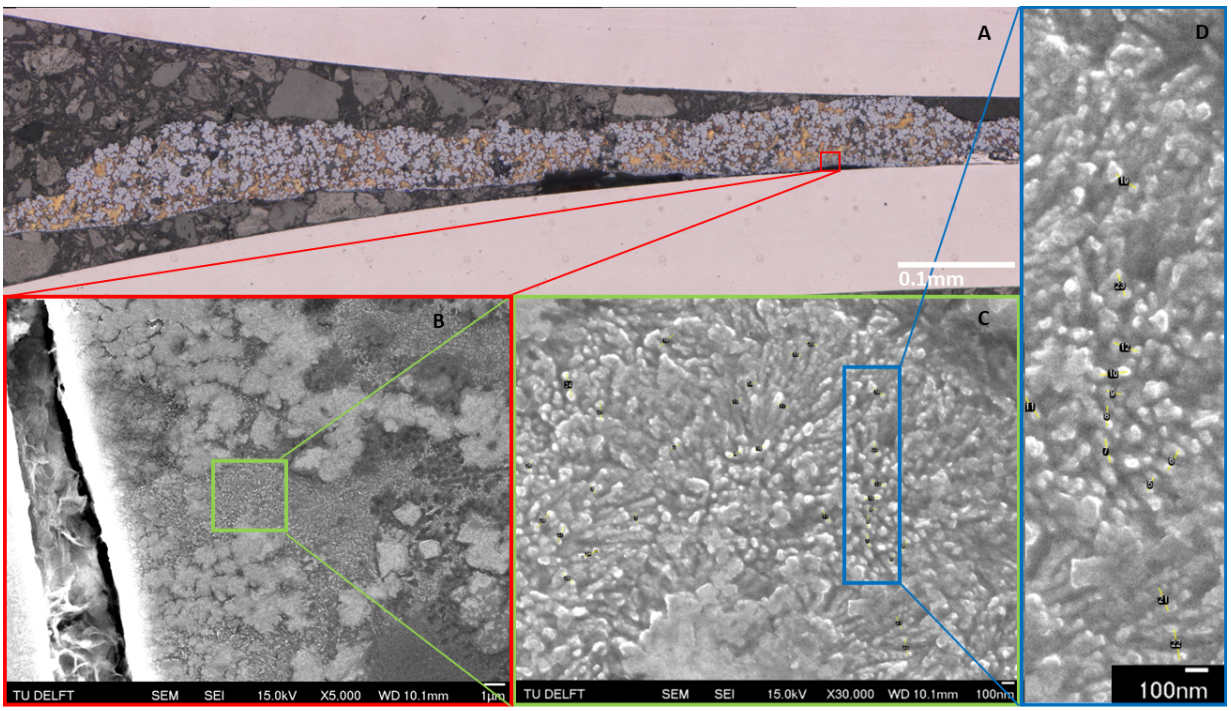

Figure 6.1: Sample overview. Image A is an optical micrograph of the cross section of the meltspun AlSi40 ribbon. B and C are SEM magnifications in the red area giving an overview of the phases present in the ribbon and the structure of the eutectic. D are examples of distance measurements between features found in the eutectic.

A more detailed view can be gained in figure 6.2. In this figure the boundary between the eutectic phase and the primary silicon phase is investigated. Furthermore a closer look is taken at the eutectic zone. In image A an overview of the investigated area is presented. Following the areas outlined in red, it can be seen that the eutectic phase surrounding the Si phase, is significantly coarser than that further away from the Si phase. In these areas more material is etched away than in the middle of the eutectic phase, suggesting a different composition of the material. It is possible that in this area aluminium has diffused out of the primary Si phase, which holds almost no aluminium in equilibrium conditions. This leaves a higher percentage of aluminium around the Si phase, which in turn is etched away more quickly than the Si. Areas like these are present around all primary Si phase, and are extra clear when the eutectic area is small, due to it being surrounded by primary Si. Following the green outlined areas, the shape and size of the eutectic phase can be observed. From the 100.000 times magnified image (D) the fibrous nature of this phase is not clear, since hard straight edges can be observed instead of the more round shapes found in literature.

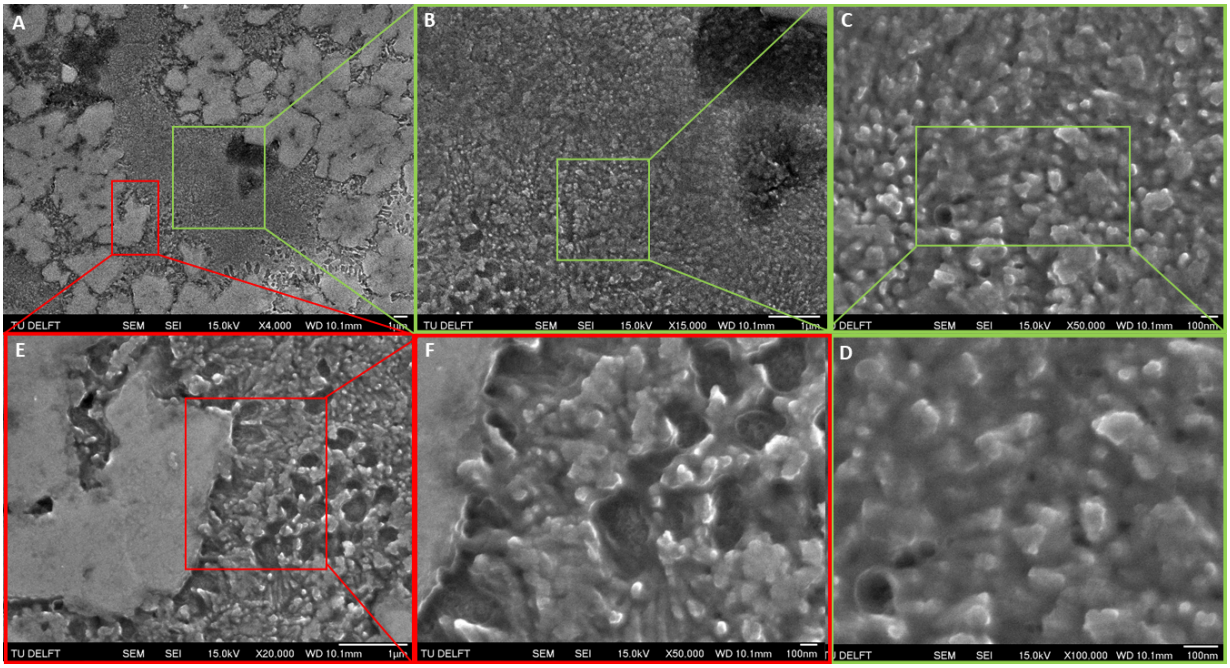

Figure 6.2: SEM micrographs of meltspun AlSi40. Images A, B, C, D show an increasing magnification of the eutectic zone. Images E and F are magnifications of the boundary between the primary silicon crystal and the eutectic zone.

Table 6.1: SEM equipment and setup

Instrument	JEOL JSM-6500F
Magnification	4.000x - 100.000x
Voltage	15.0kV
WD	10.1 mm
Detector	SEI and BEI

6.4. EDS

In order to verify if the analysis of the different phases observed in the SEM images is correct, an EDS scan is made. Via dispersive x-ray spectroscopy, the composition of the material can be determined. This analysis can be done point wise, line wise or an area can be scanned. In figure 6.3 two locations are presented were multiple points have been scanned. In tables 6.3 and 6.2. The EDS analysis shows that the Si content in the primary Si phase is at least 73 atom percent. This value is an average from the analysis beam volume, and could therefore be influenced by material beneath the primary Si. It is also possible that what appears to be a single Si crystal, are in fact multiple Si crystals close together with a small amount of eutectic phase in between. Using the unetched sample not enough detail can be provided to rule this out, however these types of areas can be seen in the etched samples. A 2D EDS scan can make these areas visible. In figure 6.4 a 2D EDS scan is presented. From this image it becomes clear that some Si phase areas consists of multiple smaller Si crystals. In the upper right corner this is clearly visible.

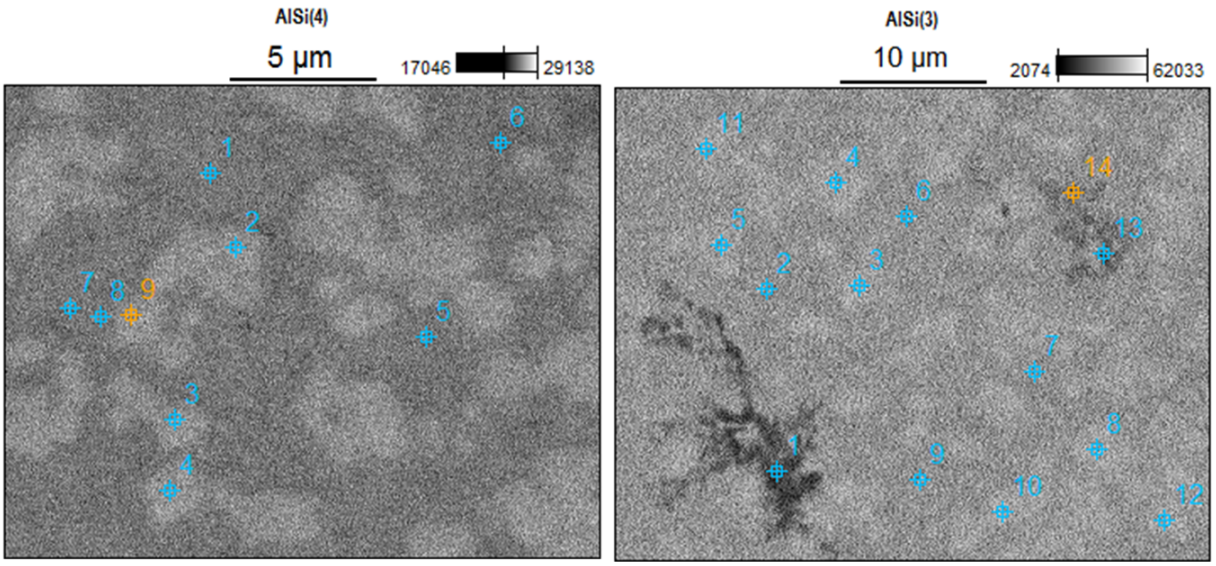

Figure 6.3: Multiple EDS point scans in two different areas of the meltspun AlSi40 ribbon.

Table 6.2: EDS results for measurement AlSi(4), figure 6.3 of the meltspun AlSi40 ribbon.

Data point	Al Atom (%)	Si Atom (%)
1	72.74 ±0.37	21.19 ±0.24
2	11.40 ±0.16	84.58 ±0.42
3	16.16 ±0.18	79.15 ±0.41
4	07.70 ±0.14	87.40 ±0.43
5	77.47 ±0.38	15.89 ±0.21
6	47.22 ±0.29	34.51 ±0.28
7	73.03 ±0.37	20.96 ±0.24
8	68.75 ±0.36	24.43 ±0.25
9	13.05 ±0.17	82.50 ±0.42

When looking at the primary Si in figure 6.3, a slight gradient from the middle to the edge of the crystal can be observed. This suggest a composition gradient within the crystal. The same can be observed for the eutectic matrix between two crystals. With an EDS line scan this gradient can be quantified. The line scan show a decreasing concentration of Si from the center to the crystal boundary. Right after the boundary the concentration of Si seems to dip further than the eutectic value observed in the middle between two crystals. Suggesting a Si depleted zone in the eutectic at the edge of the primary Si crystal. In the etched samples this can be observed by the less fine features at this location. This implies that a higher aluminium content was present here, which was etched away. This line scan is presented in the following chapter 7 along the results of the material model created for the analysis of this material.

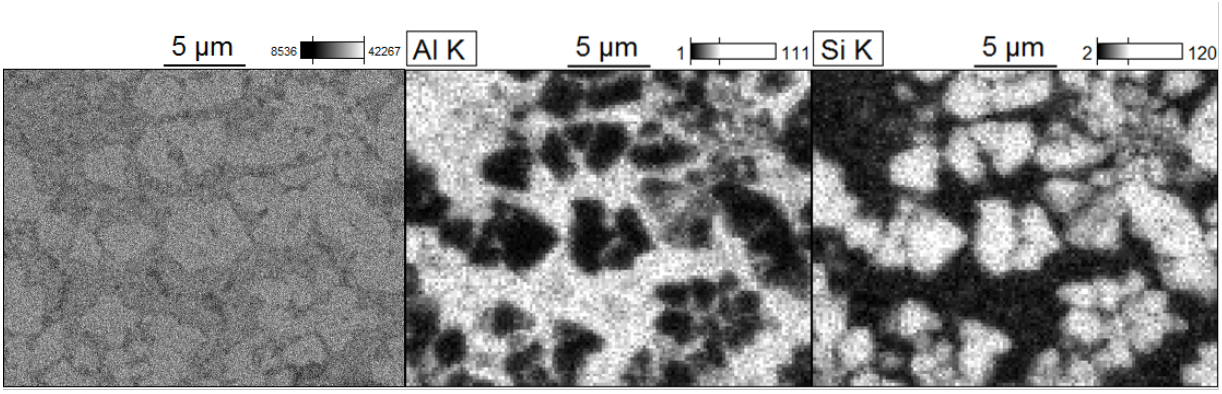

Figure 6.4: 2D EDS scan of the meltspun AlSi40 ribbon.

Table 6.3: EDS results for measurement AlSi(3), figure 6.3 of the meltspun AlSi40 ribbon.

Data point	Al Atom (%)	Si Atom (%)
1	22.58 ± 0.12	48.3 ± 0.19
2	77.66 ± 0.30	16.27 ± 0.11
3	16.26 ± 0.09	78.72 ± 0.28
4	18.37 ± 0.10	76 ± 0.27
5	21.28 ± 0.11	73.43 ± 0.27
6	76.73 ± 0.29	16.49 ± 0.11
7	79.42 ± 0.30	17.44 ± 0.11
8	12.22 ± 0.08	80.62 ± 0.29
9	75.66 ± 0.29	17.65 ± 0.11
10	5.47 ± 0.06	88.26 ± 0.31
11	43.65 ± 0.18	49.52 ± 0.20
12	3.68 ± 0.05	89.7 ± 0.31
13	34.95 ± 0.16	45.5 ± 0.19
14	46.58 ± 0.19	34.47 ± 0.16

6.5. XRD

In order to fully rule out the existence of an amorphous phase in the sample, a XRD analysis has been done. The SEM is not able to provide enough detail to see the crystal lattice. Therefore it is not possible to see if the atoms in the primary Si or in the eutectic phase are in a lattice or in an amorphous state. The XRD analysis is presented in figure 6.5 shows no signs of an amorphous phase present in the ribbon. The XRD analysis is carried out over the full width of the ribbon sample. The top and bottom side of the ribbon are measured. The results are compared with a pure Si monocrystallic plate. The XRD measurement (black line) matches well with the Al and Si phase. A bump is present at low 2theta angle which could be caused by an amorphous phase present. A second measurement with an empty wafer was taken to ensure that this bump belongs to random noise instead of an amorphous phase. Large quantities of amorphous phase can therefore be ruled out in this sample. Turning the sample upside down gave the same result (not shown in the figure). The settings for the XRD measurement can be found in table 6.4.

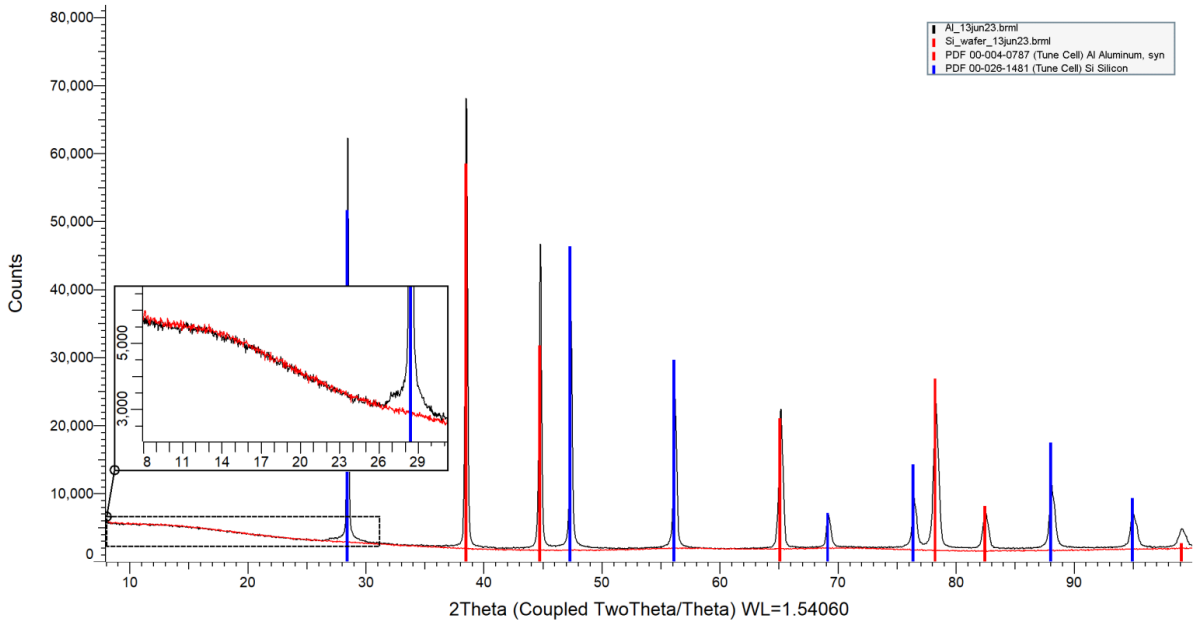

Figure 6.5: XRD measurement of the meltspun AlSi40 ribbon

Table 6.4: XRD equipment and setup

Instrument	Bruker D8 Advance diffractometer Bragg-Brentano geometry Cu Kα radiation, 40 kV, 40 mA
Divergence Slit **Sample Spinning** **Soller Slits** **Detector**	Fixed, Illuminated length 6 mm No Diffracted beam 2.5 degrees LynxEye XE-T position sensitive detector in High Resolution setting
Measurement	Coupled θ-2θ Step size 0.04° 2θ Counting time per step 1s
Data Evaluation	Bruker software Diffrac.EVA vs 6.1

6.6. Discussion

To analyse the microstructure of the AlSi alloy created via meltspinning, SEM, EDS, and XRD have been used. The results from these measurements show a two phase crystalline microstructure, consisting of primary Si crystals with a size in the order of 5 µm, and an eutectic phase consisting of alternating Si and Al phases with a feature size in the order of 100 nm. Furthermore the composition of these phases is different than what would be expected according to the equilibrium phase diagram. The Si phase contains significant amount of aluminium, normally only present in trace amounts. A slight shift to the right can be observed in the XRD measurements at high 2theta angle, suggesting significant strain in the crystal lattice. This is however not further investigated. The composition of the eutectic phase has been shifted towards containing significantly more Si. In the following chapter a material model will be presented to explain the found microstructure and its composition.

7

Material modelling

For the calculation of the phase composition two methods are used. Firstly a kinetic phase diagram is constructed. In this diagram the non-equilibrium liquidus and solidus boundaries are constructed based on the equilibrium phase diagram, solidification speed, and diffusion speed of the material. Secondly this kinetic diagram is then used as a starting point for a Scheil calculation, which incorporates the changing concentration of the liquid during rapid solidification.

For the kinetic phase diagram calculation, it is assumed that the solidus and liquidus lines approach the T0 line at an equal rate, when rapidly solidifying. The T0 temperature is the composition at which the liquid crystallizes without phase separation. This happens when the solidification front moves so fast that diffusion of in the liquid can be neglected. Therefore the T0 composition can be seen as the extreme composition which the system reaches with ever increasing solidification rates. To which degree the solidus and liquidus lines shift towards the T0 line is determined by the rate of liquid diffusion, and the solidification rate.

The Scheil calculation assumes no solid diffusion takes place due to the speed of the solidification front, at the same time it assumes infinite liquid diffusion. This means that at the solidification boundary the liquid is always at its equilibrium composition. Solid diffusion is several orders of magnitude slower than liquid diffusion. This assumption can be made because it is a good predictor for phase composition as the solidification rate is much lower than typical for PFC. However the infinite liquid diffusion assumption is not applicable, since it is known that partitionless alloys can be produced with PFC.

Using a combination of the kinetic phase diagram and the Scheil equation would therefore improve the calculated phase composition since the infinite liquid diffusion assumption is replaced with the kinetic phase diagram calculation. The final calculation will result in a plot of the concentration against the solid fraction. From this the concentration profile of the primary Si crystal and the eutectic composition can be deduced. This result can then be compared with EDS data. Finally a verification attempt of the results is made by using the found composition and the area ratio of the two phases form the SEM images. In table 7.1, the parameters used in the material model are presented.

7.1. Kinetic phase diagram

To calculate the kinetic phase diagram, the method employed by Pieratoni et al. [16] is used, who in turn adapted it from Boettinger et al [17]. The standard AlSi phase diagram from Murray et al. [18] is used. This diagram includes the T0 data. The first step is to calculate the kinetic partition coefficient. The partition coefficient k is the ratio between the solidus C_S composition and the liquidus composition C_L, and is defined according to equation 7.1, the definition is the same for equilibrium and kinetic partition coefficient.

$$k = \frac{C_S}{C_L} \tag{7.1}$$

The new kinetic composition is calculated according to equation 7.2. In this equation k_V is the kinetic partition coefficient, k_e is the equilibrium partition coefficient, when the solidification speed approaches 0. D is the diffusion across the interface. a0 is the interface thickness. V is the speed of solidification front.

$$k_V = \frac{k_e + a0\frac{V}{D}}{1 + a0\frac{V}{D}} \tag{7.2}$$

Next the kinetic concentration lines are constructed. Equation 7.3 ensures that the solidus and the liquidus line approach the T0 line and an equal rate. In this equation $C_L(V)$ is the kinetic liquidus concentration, $C_S(V)$ is the kinetic solidus concentration $C_L(0)$ and $C_S(0)$ are respectively the equilibrium liquidus and solidus concentration. C_{T0} is the T0 concentration.

$$\frac{C_L(V) - C_{T0}}{C_L(0) - C_{T0}} = \frac{C_S(V) - C_S(0)}{C_L(0) - C_{T0}} \tag{7.3}$$

The diffusion coefficient and interface thickness, are two parameters of great influence on this equation. Both value are difficult to determine analytically or measure directly. The diffusion coefficient can fluctuate wildly (orders of magnitude) [19][20] with the conditions at the interface.

The result of these calculation is plotted on top of the original phase diagram in figure 7.1. From this figure the new eutectic compositing and temperature can be found. The eutectic decreases in temperature and increases in Si concentration. This has as a result that the eutectic will solidify at an earlier stage in an hyper eutectic system, because there the Si solidifies first, decreasing the Si concentration in the remaining liquid. Other notable effects are that both liquidus lines drop in temperature, whilst the solidus lines increase in temperature. Where there would be almost no aluminium present in the primary silicon crystal, now a significant percentage of atoms are incorporated in the Si crystal. This can be seen in the EDS data.

Table 7.1: Parameter used in the material model

Description	Parameter	
Kinetic partition coefficient	k_V	
Equilibrium partition coefficient	k_e	
Liquidus concentration	C_L	
Solidus concentration	C_S	
T0 concentration	C_{T0}	
Si starting concentration	C_0	
Solid fraction	f_S	
Constants		
Description	Parameter	Value
Interface thickness	a0	0.5 nm [16]
Solidification rate	V	0.5 m/s
Interface diffusion coefficient	D	$4.3E-9$ m^2/s [19]

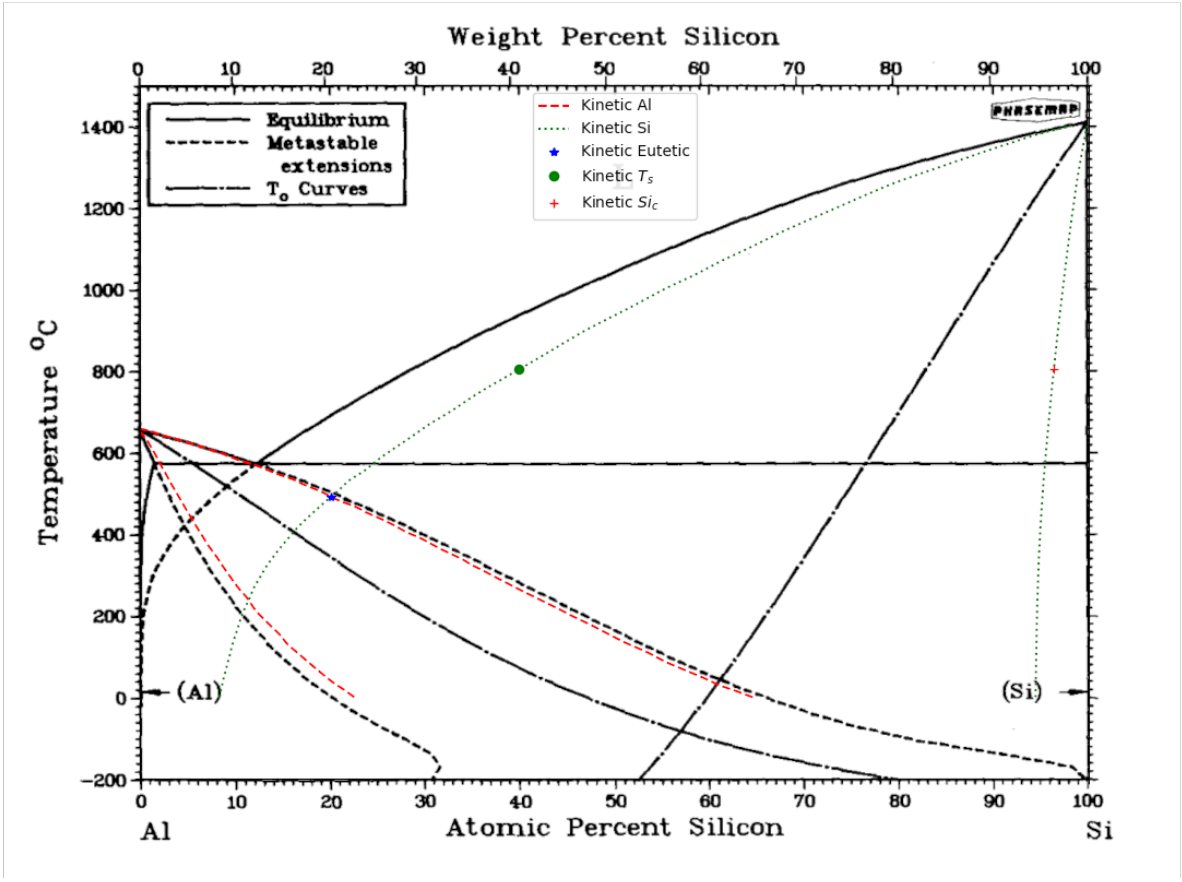

Figure 7.1: Original AlSi phase diagram extended with the kinetic phase diagram. Using the red and green dotted lines, the kinetic composition for the AlSi40 alloy can be determined. The dotted lines show the temperature shift of the liquidus and solidus lines, caused by rapid cooling of the metal. The new eutectic point is presented with a blue star. The new composition for AlSi40 can be calculated using the lever rule presented as the green circle and red plus.

7.2. Scheil equation

The result from the kinetic phase diagram form the starting point for the Scheil calculation. This calculation uses a partition coefficient, starting composition and the eutectic point. All these values will be taken from the kinetic phase diagram instead of the equilibrium diagram. With the Scheil equation the concentration profile of the primary Si crystal can be calculated until the eutectic forms. This data can be plotted against a line scan, which starts inside a primary Si crystal and crosses over the boundary with the eutectic. Because the line scan is made from one Si crystal to another, the results from the Scheil equation are mirrored at the center of the eutectic phase.

According to the Scheil equation the boundary between the two phases is very sharp, this is in accordance with the SEM images and the theory that the crystals have a hard well defined boundary. However when looking at the EDS data the boundary is soft and more spread out over a distance. The concentration profile is not a step like function as would be expected. This is due to the nature of the measurement. The EDS beam scanner has a certain volume which is measured. At 5 kV and this particular AlSi alloy, this volume is in the neighbourhood of 0.25 µm in all directions. This results in a measurement that is averaged over this volume. When moving over a step like feature the resulting measurement will be sloped. Therefore this effect is simulated on top of the results from the Scheil equation with a convolution. The results can now better be compared. The beam convolution will have a width similar to that of the real measurement, and will therefore average over values 0.25 µm, in both directions. Furthermore, the beam effect is decreased a the edges of the beam since the volume of the beam is spherical.

The Scheil equation is presented in equation 7.4. In this equation C_S is the concentration of Si in the solid. k_V is the kinetic partition coefficient calculated earlier, C_0 is the initial concentration of Si, and f_S is the fraction solidified. f_S runs from 0 to 1. To compare the results with the line scan, the result is mirrored, as if the same calculation is made starting from the second Si grain. The Scheil equation is valid until the eutectic concentration is reached, which is also taken from the non-equilibrium phase diagram. This means that equation 7.4 is valid until f_S equals 0.25. The results are presented and compared in figure 7.2

$$C_S = k_V C_0 (1 - f_S)^{k_V - 1} \tag{7.4}$$

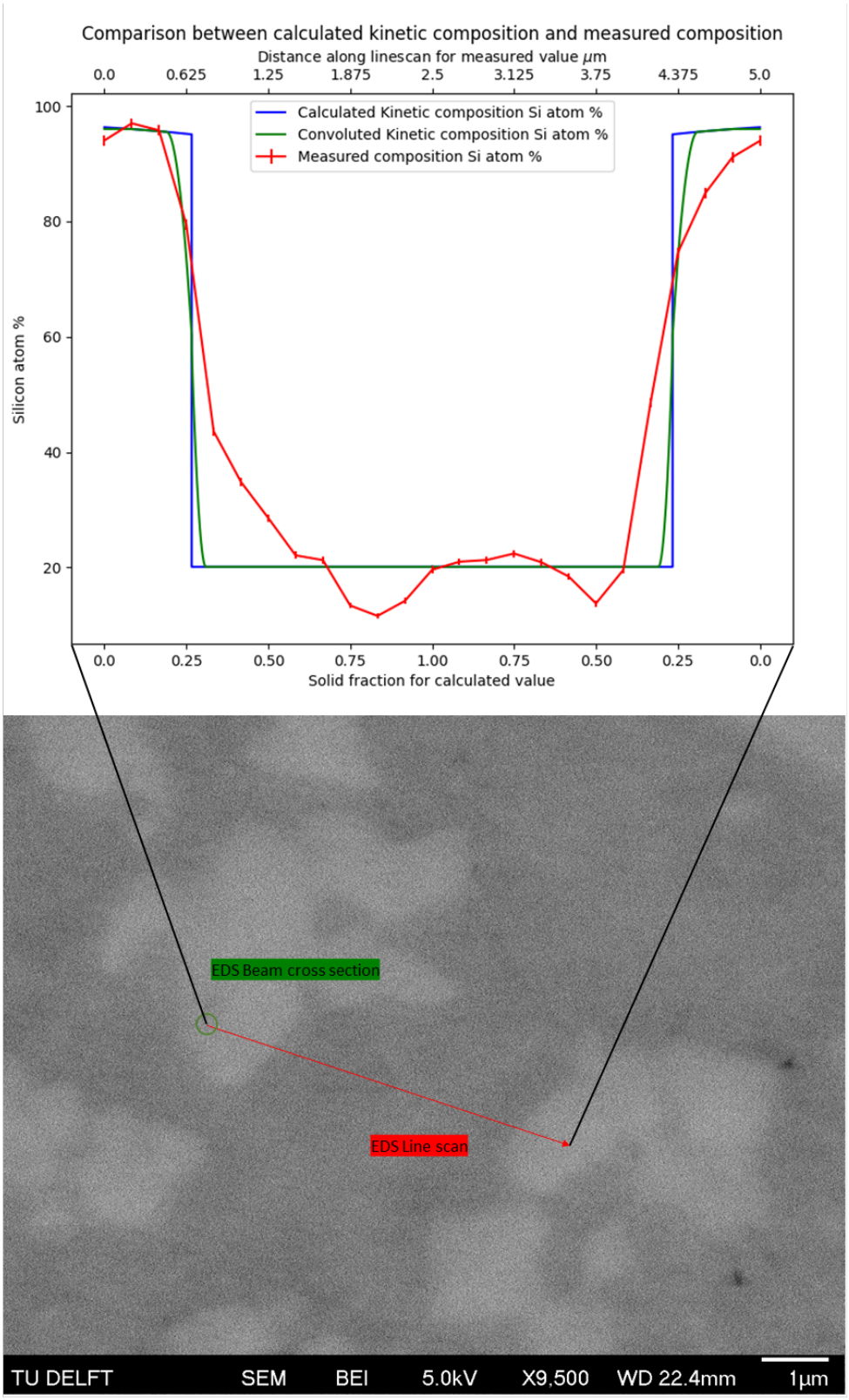

Figure 7.2: In this figure the results from the EDS line scan are compared with the results from the kinetic phase diagram and the Scheil equation. The red line represents the line scan. The green and blue lines are the calculated values with and without beam convolution. In the SEM image the line scan location and direction is presented in red and the the beam size, on which the beam convolution is based is represented by the green circle.

7.3. Grain size

The average grain size is calculated by taking measurements of each Si grain, the shortest and longest distance from side to side. The average grain size for this location is 3.2 µm across. The features in the eutectic are on average spaced 102 nm apart see table 7.2 and figure 7.3. The dark areas in this image have the same composition as the eutectic phase and are therefore likely etch effects. This is however not further investigated.

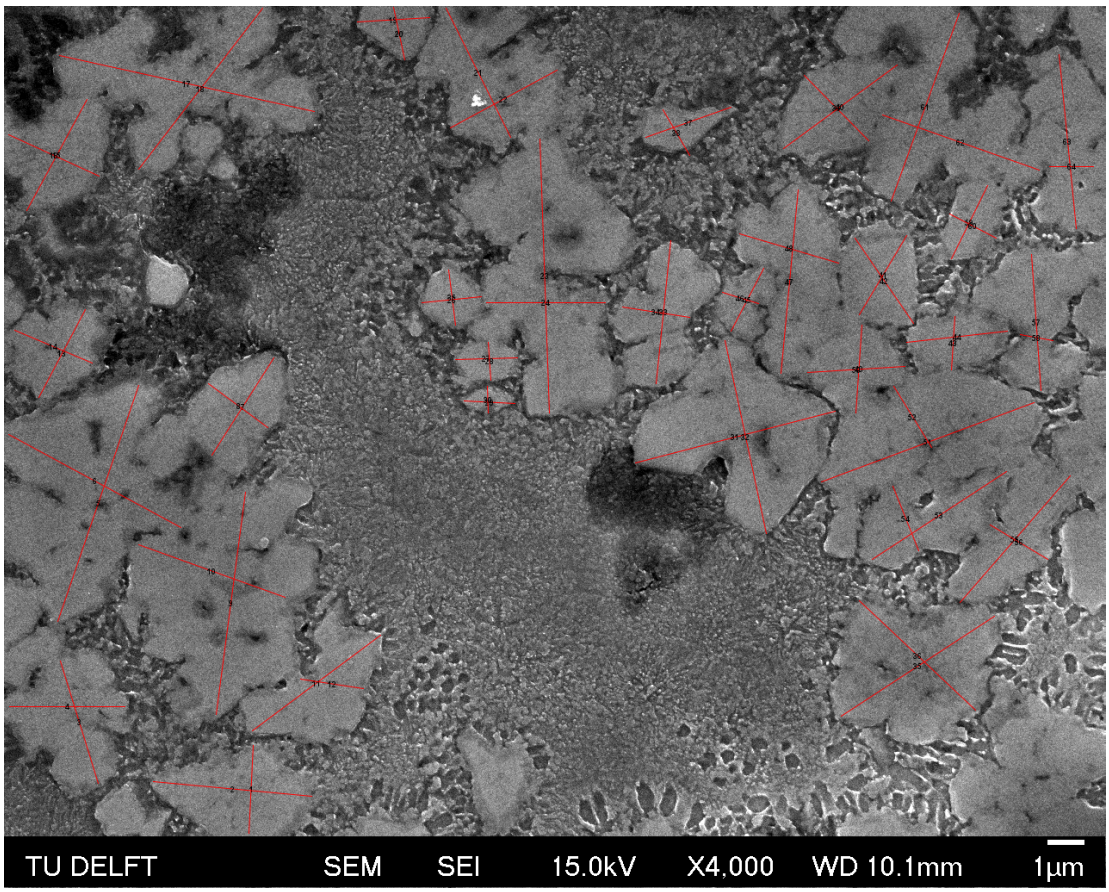

Figure 7.3: Average grain size calculations. These are based on two measurements on each grain. Results can be found in table 7.2

Table 7.2: Feature size

Measurement	Average length
Primary Si crystal	3.2 µm
Eutectic feature size	102 nm

7.4. Area composition calculation

For a second verification, the ratio of the area of the different phases can be compared with the one expected from the kinetic phase diagram. This calculation is carried out by using ImageJ to convert the SEM image into a binary image, with the Si represented as white and eutectic phase as black. This is done be choosing a certain cut off value, where all values above the cutoff become white and the other black. This results in an image with white speckles throughout the black eutectic areas, because the value can not be precisely split this way. Two methods are employed to get rid of this noise. Firstly the image is edited with a Gaussian blur to reduce the noise. Second after binarisation, the image is eroded, converting all the pixel at an edge to black. This results in the deletion of all single pixel white areas. This is done multiple times whilst comparing it to the original SEM image, to make sure that no actual grains are lost. Finally the image is dilated, adding a white pixel at all edge values, the same amount of times. This restores the grains to their original size. The resulting image is presented in figure 7.4. In this image one half is original whilst the other half is the result of the modification. As can be seen the grains are the same size and fit nicely with each other on the boundary of both images. This is done for multiple SEM images. Now the ratio between the Si and eutectic phase can be calculated by dividing the black area by the white area. The value can then be compared to the value for equilibrium solidification, or the expected value according to the non-equilibrium calculation for AlSi40. For this comparison the weight fraction has to be converted to the volume fraction. The results can be found in table 7.3.

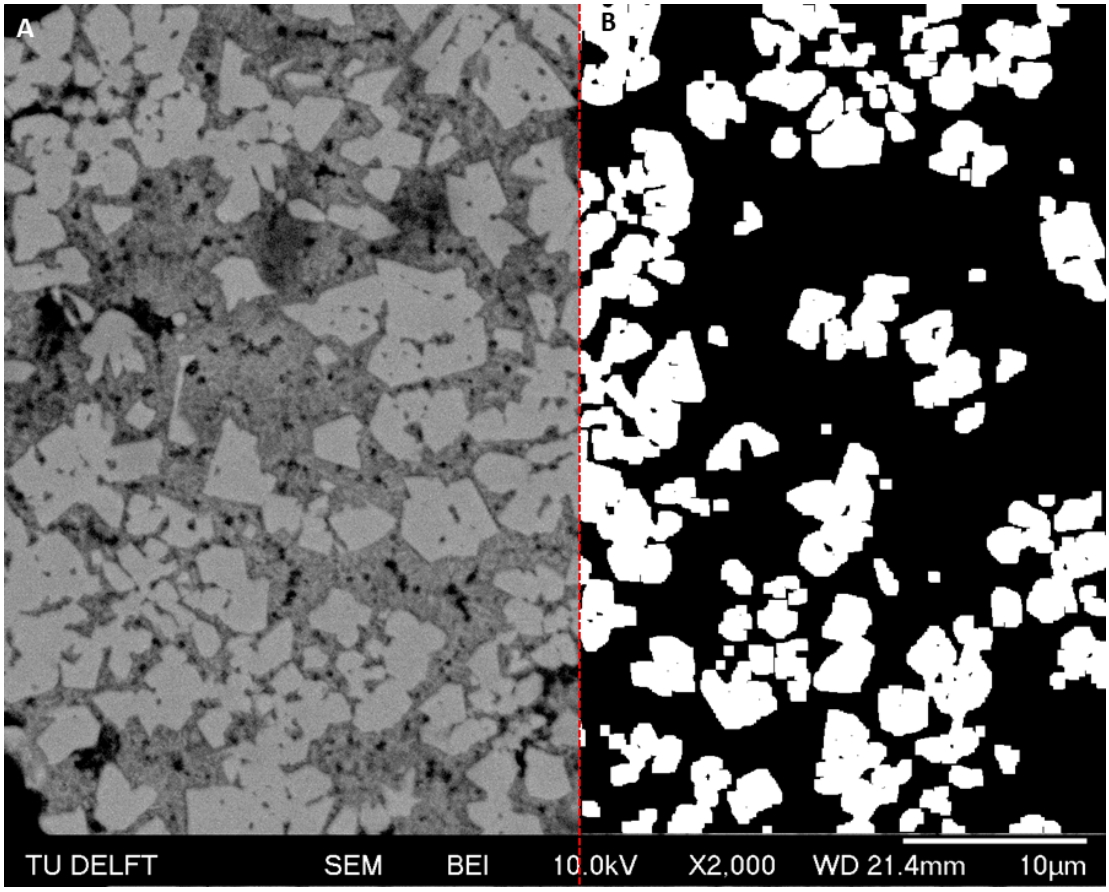

Figure 7.4: Results from the binary conversion of an back scatter SEM image. Image A is the left half of the original SEM image, image B is the result of the converted image. On the boundary a red line is plotted. On the boundary the comparison between the original grain size and the converted grain size can be made.

7.5. Discussion

With the material model, an explanation is provided for the microstructure observed in the rapidly solidified ribbon. The measurements showed a composition that deviated from the equilibrium phase diagram. By construction a non-equilibrium phase diagram is was shown that the experimental observations can be theoretically explained, by assuming that diffusion in the solid phase is negligible and that diffusion in the liquid phase is severely hindered. What the exact non-equilibrium phase diagram looks like, is highly dependent on the chosen diffusion coefficient, solidification rate, and interface thickness. However that it lies somewhere between the equilibrium diagram and the T0 line is certain. From the XRD analysis is can be concluded that there is no amorphous phase so the solidification rate is not high enough to move below the T0 line. With the parameters chosen for this diagram, the results are close to the measured values. Furthermore, the Scheil equitation correctly predicts a decrease in Si concentration from the center to the edge of the grain. By adding the beam convolution it can be seen that the prediction for the phase transition between the Si grain and the eutectic is reasonable. For a better prediction the exact solidification rate of the ribbon must be determined. The solidification rate can be determined via multiple methods. On way is to look at the dwell time of the puddle on top of the wheel. When a successful ribbon is cast, the ribbon has to solidify within this time. This way a maximum for the solidification rate can be established. A more accurate experiment is to look at the size of the melt puddle this can be done by high speed photography of the melt puddle, this is called the puddle length.

The solidification rate can also be determined through simulations; however, due to the many assumptions that must be made, regarding the heat transfer coefficient from the puddle to the wheel, a certain level of uncertainty exists. This is the method used in this case.

From the microstructure solidification rate can also be deduced. This is done via the secondary arm spacing in the eutectic structure. This relationship is exponential so a small deviation in coefficients will lead to a vastly different solidification rate.

As described earlier when the diffusion coefficient and interface thickness are well known, it should be possible to say something about the solidification rate by analysing the concentration profiles of the Si and eutectic phase, or by the ratio of these phases present in the material. This would be done by doing the Scheil and kinetic phase calculation in reverse.

The verification method using the area ratio does not give any insightful results. The area ratio using the SEM images show to much variation. For this method to work, new images would have to be taken, were a large part of the ribbon is measurable. This is difficult since the image must be magnified enough to able to clearly determine the phase boundary.

Table 7.3: Area ratio silicon

Calculated	Si Area percentage
Equilibrium	29 %
Non equilibrium	24 %
Measurement	**Si Area percentage**
1	44 %
2	26 %
3	54 %

Part IV

Closure

8

Conclusion

The planar flow casting process, extensively described in literature and used in material scientific research for years, was revisited in order to transition from academia to industrial production. Due to the complexity of the process not many large scale application for this process have been successful. Models were created in order to capture all relevant physics of the process and make their influence on the process clear and quickly interpretable. Efforts were made to verify this model using a modern simulation package from Comsol. The first results show great similarity between the model and the simulations, however it would require more optimization and refinement in order for it to be useful as a production tool. This work was then used to build a model for the system and control setup applicable for the testing facility at RSP Technology. This facility is limited in the adjustments that can be made to the existing test machine. Therefore, a pressure based control system is chosen, in order to reliably create a product with a constant geometry and quality. This method requires the least modifications to the existing system and is most practical to implement. Sensor and actuator requirements were chosen according to the system and control model, in which their influence on the system was quantified.

Important work still to be done, is to experimentally validate the three process models created and used in this work. These experiments be done once the modifications to the test machine are completed. The difficulty is that these modifications would be based on this work, which in turn is not validated yet. The experimental work has to be used to improve the model, for which assumptions are used which are dependent on specific situations.

To get a complete picture of the PFC process, the product is analysed as well. The main goal of this technique is to rapidly solidify metals. Therefore, it is important to understand the influence of the process on the microstructure of the material. This was done be studying the effects of rapid solidification of metals in general and AlSi alloys in particular. Multiple investigative techniques have been used to get insight into the microstructure of the ribbon created with the current production method. These techniques include SEM, EDS and XRD. The results found were then compared to a material model created for rapid solidification. This model consists of both a kinetic phase diagram, and the use of the Scheil equation. The created model showed strong similarities with the microstructure observed, most clearly in the extended solubility of Al in primary Si and the shift in eutectic composition, favoring a higher percentage of Si. Other notable observations are the average grain size of the primary Si of 5 μm and the feature spacing in the eutectic phase of 100 nm. The methods employed for the characterisation of the material can be used in order to study the change of the material, with a change of process in the future. With this model it will be possible to conclude if the planar flow process improves the quality and solidification rate of the material. Such a comparison is however not done yet, but all the prerequisites are in place to do this analysis.

Therefore the next steps for this research are implementation of the necessary modification to make PFC possible. Secondly, experimental verification of the models used for the PFC process. Finally comparing the product created with PFC in the same manner as the FFC product was analysed.

References

[1] Cormac J. Byrne et al. “Capillary puddle vibrations linked to casting-defect formation in planar-flow melt spinning”. en. In: *Metallurgical and Materials Transactions B* 37.3 (June 2006), pp. 445–456. DOI: 10.1007/s11663-006-0029-4. URL: http://link.springer.com/10.1007/s11663-006-0029-4 (visited on 10/29/2021).

[2] Paul H. Steen et al. “FLUID MECHANICS OF SPIN CASTING OF METALS”. en. In: *Annual Review of Fluid Mechanics* 29.1 (Jan. 1997), pp. 373–397. DOI: 10.1146/annurev.fluid.29.1.373. URL: https://www.annualreviews.org/doi/10.1146/annurev.fluid.29.1.373 (visited on 03/09/2022).

[3] Deren Li et al. “The pressure loss and ribbon thickness prediction in gap controlled planar-flow casting process”. en. In: *Journal of Materials Processing Technology* 211.11 (Nov. 2011), pp. 1764–1767. DOI: 10.1016/j.jmatprotec.2011.05.019. URL: https://linkinghub.elsevier.com/retrieve/pii/S092401361100152X (visited on 11/03/2021).

[4] Ryu Seino et al. “Observation of melt puddle behavior in planar flow casting in air”. en. In: *Journal of Alloys and Compounds* 586 (Feb. 2014), S150–S152. DOI: 10.1016/j.jallcom.2013.04.189. URL: https://linkinghub.elsevier.com/retrieve/pii/S0925838813011213 (visited on 03/08/2022).

[5] Cormac J. Byrne et al. “Capillary stability limits for liquid metal in melt spinning”. en. In: *Chemical Engineering Science* 61.24 (Dec. 2006), pp. 8004–8009. DOI: 10.1016/j.ces.2006.06.026. URL: https://linkinghub.elsevier.com/retrieve/pii/S0009250906006130 (visited on 03/01/2022).

[6] Farid Samara et al. “Natural Convection Driven Melting of Phase Change Material: Comparison of Two Methods”. en. In: ().

[7] *Two-Phase Flow Modeling Guidelines*. en. URL: https://www.comsol.com/support/learning-center/article/Two-Phase-Flow-Modeling-Guidelines-59411 (visited on 09/01/2023).

[8] *Your Guide to Meshing Techniques for Efficient CFD Modeling*. en. URL: https://www.comsol.com/blogs/your-guide-to-meshing-techniques-for-efficient-cfd-modeling/ (visited on 09/01/2023).

[9] J. K. Carpenter et al. “Planar-flow spin-casting of molten metals: process behaviour”. en. In: *Journal of Materials Science* 27.1 (Jan. 1992), pp. 215–225. DOI: 10.1007/BF00553859. URL: https://doi.org/10.1007/BF00553859 (visited on 01/31/2023).

[10] Heping Liu et al. “Numerical Simulation of Initial Development of Fluid Flow and Heat Transfer in Planar Flow Casting Process”. en. In: *Metallurgical and Materials Transactions B* 40.3 (June 2009), pp. 411–429. DOI: 10.1007/s11663-009-9236-0. URL: http://link.springer.com/10.1007/s11663-009-9236-0 (visited on 03/07/2022).

[11] B.L. Cox et al. “‘Herringbone’ defect formation in planar-flow melt spinning”. en. In: *Journal of Materials Processing Technology* 213.10 (Oct. 2013), pp. 1743–1752. DOI: 10.1016/j.jmatprotec.2013.04.009. URL: https://linkinghub.elsevier.com/retrieve/pii/S0924013613001386 (visited on 03/08/2022).

[12] Garry Berkovic et al. “Optical methods for distance and displacement measurements”. en. In: *Advances in Optics and Photonics* 4.4 (Dec. 2012), p. 441. DOI: 10.1364/AOP.4.000441. URL: https://opg.optica.org/aop/abstract.cfm?uri=aop-4-4-441 (visited on 03/07/2022).

[13] A. G. Sheard. “Blade by Blade Tip Clearance Measurement”. en. In: *International Journal of Rotating Machinery* 2011 (2011), pp. 1–13. DOI: 10.1155/2011/516128. URL: http://www.hindawi.com/journals/ijrm/2011/516128/ (visited on 03/09/2022).

[14] Yu-Guang Su et al. “Tuning the Planar-Flow Melt-Spinning Process Subject to Operability Conditions”. en. In: *JOM* 66.7 (July 2014), pp. 1277–1286. DOI: 10.1007/s11837-014-0982-3. URL: http://link.springer.com/10.1007/s11837-014-0982-3 (visited on 10/29/2021).

[15] Jaafar Hadi Abboud et al. “Ultra-refined primary and eutectic silicon in rapidly solidified laser produced hypereutectic Al–Si alloys”. en. In: *Advances in Materials and Processing Technologies* (Apr. 2021), pp. 1–23. DOI: 10.1080/2374068X.2021.1913326. URL: https://www.tandfonline.com/doi/full/10.1080/2374068X.2021.1913326 (visited on 11/03/2022).

[16] M Pierantoni et al. “THE COUPLED ZONE OF RAPIDLY SOLIDIFIED A1-Si ALLOYS IN LASER TREATMENT”. en. In: ().

[17] William J. Boettinger. “Growth Kinetic Limitations During Rapid Solidification”. en. In: *MRS Proceedings* 8 (1981), p. 15. DOI: 10.1557/PROC-8-15. URL: http://link.springer.com/10.1557/PROC-8-15 (visited on 04/26/2023).

[18] J. L. Murray et al. “The Al-Si (Aluminum-Silicon) system”. en. In: *Bulletin of Alloy Phase Diagrams* 5.1 (Feb. 1984), pp. 74–84. DOI: 10.1007/BF02868729. URL: https://doi.org/10.1007/BF02868729 (visited on 05/03/2023).

[19] P. Magnin et al. “Eutectic growth: A modification of the Jackson and Hunt theory”. en. In: *Acta Metallurgica et Materialia* 39.4 (Apr. 1991), pp. 453–467. DOI: 10.1016/0956-7151(91)90114-G. URL: https://linkinghub.elsevier.com/retrieve/pii/095671519190114G (visited on 09/26/2023).

[20] O. Krause et al. “Determination of aluminum diffusion parameters in silicon”. en. In: *Journal of Applied Physics* 91.9 (May 2002), pp. 5645–5649. DOI: 10.1063/1.1465501. URL: https://pubs.aip.org/jap/article/91/9/5645/293035/Determination-of-aluminum-diffusion-parameters-in (visited on 07/26/2023).

A

PFC model Python code

Listing A.1: PFC model Python code

```
# -*- coding: utf-8 -*-
"""
Created on Tue Aug 1 22:14:18 2023

@author: roald
"""

import numpy as np
import matplotlib.pyplot as plt
import matplotlib.colors as mcolors

cmapr = mcolors.ListedColormap(['red'])
cmapb = mcolors.ListedColormap(['blue'])
cmapbk = mcolors.ListedColormap(['black'])

plt.close('all')

def PFC(G=0.9E-3, P=50000, U=15):
    # Constants
    sigma = 0.821
    K = 2
    Rho = 2400 * 0.6 + 0.4 * 2570
    theta = 2.618


    # Calculate parameters
    z = (2 * sigma) / G
    We = (Rho * U**2) / z
    Pcap = (sigma * (1 - np.cos(theta))) / G
    T = (G / U) * np.sqrt((2 * (P - Pcap)) / ((1 + K) * Rho))
    Ploss = 0.5 * K * (0.16)**2 * Rho * U**2
    Pmin = P - Pcap
    Pmax = P - Ploss - Pcap

    return T, Pmin, Pmax, We

# Define ranges for parameters
P = np.linspace(0, 60000, 100)
U = np.linspace(0, 30, 100)
G = np.linspace(0, 1E-3, 100)
```

```
# Calculate values for each parameter combination

def limit_plot(T, Pmin, Pmax, We, X, Y):
    Pmin_limit = np.ma.masked_where(Pmin > 0, Pmin)
    We_limit = np.ma.masked_where(We < 200, We)
    Pmax[np.isnan(Pmax)] = 1
    Pmax_limit = np.ma.masked_where(Pmax <= 0, Pmax)

    plt.imshow(T*1E6, extent=[X.min(), X.max(), Y.min(), Y.max()],
               cmap='Greens', vmin=0, vmax=100, origin='lower', aspect='auto')
    cbar = plt.colorbar()
    cbar.set_label(r'Ribbon thickness ($\mu$m)', rotation=270, labelpad=15)
    plt.imshow(Pmax_limit, extent=[X.min(), X.max(), Y.min(), Y.max()],
               cmap=cmapr, origin='lower', aspect='auto')

    plt.imshow(Pmin_limit, extent=[X.min(), X.max(), Y.min(), Y.max()],
               cmap=cmapbk, origin='lower', aspect='auto')

    plt.imshow(We_limit, extent=[X.min(), X.max(), Y.min(), Y.max()],
               cmap=cmapb, origin='lower', aspect='auto')
    plt.text(0.15*X.max(), 0.02*Y.max(), 'Flow Limited', color='white', ha='center', va
        ↪ ='center')
    plt.text(0.85*X.max(), 0.95*Y.max(), 'Speed Limited', color='white', ha='center', va
        ↪ ='center')

    return

def Pressure_plot(G, U, P):
    # data calc
    T = np.zeros([len(G), len(U)])
    Pmin = np.zeros([len(G), len(U)])
    Pmax = np.zeros([len(G), len(U)])
    We = np.zeros([len(G), len(U)])

    for x in range(len(G)):
        for y in range(len(U)):
            T[x, y], Pmin[x, y], Pmax[x, y], We[x, y] = PFC(G=G[x], P=P, U=U[y])

    # plotting
    plt.figure(1)
    plt.ylabel('Gapsize ($\mu$m)')
    plt.xlabel('Wheel Speed (m/s)')
    plt.title(f'Gapsize and Wheel speed limits for P = {P/1000} (kPa)')
    plt.text(0.15*U.max(), 0.95*1E6*G.max(), 'Pressure Limited', color='white', ha='
        ↪ center', va='center')
    limit_plot(T, Pmin, Pmax, We, U, G*1E6)

def Speed_plot(G, U, P):
    T = np.zeros([len(P), len(G)])
    Pmin = np.zeros([len(P), len(G)])
    Pmax = np.zeros([len(P), len(G)])
    We = np.zeros([len(P), len(G)])

    # data calc
```

```
    for x in range(len(G)):
        for y in range(len(P)):
            T[x, y], Pmin[x, y], Pmax[x, y], We[x, y] = PFC(G=G[x], P=P[y], U=U)

    # plotting
    plt.figure(2)
    plt.ylabel('Gapsize ($\mu$m)')
    plt.xlabel('Pressure (kPa)')
    plt.title(f'Gapsize and Wheel Pressure limits for U = {U} (m/s)')
    plt.text(0.85/1000*P.max(), 0.5*1E6*G.max(), 'Pressure Limited', color='white', ha='
        ↪ center', va='center')
    limit_plot(T, Pmin, Pmax, We, P/1000, G*1E6)

def Gap_plot(G, U, P):
    T = np.zeros([len(P), len(U)])
    Pmin = np.zeros([len(P), len(U)])
    Pmax = np.zeros([len(P), len(U)])
    We = np.zeros([len(P), len(U)])

    # data calc
    for x in range(len(P)):
        for y in range(len(U)):
            T[x, y], Pmin[x, y], Pmax[x, y], We[x, y] = PFC(G=G, P=P[x], U=U[y])

    # plotting
    plt.figure(3)
    plt.ylabel('Pressure (kPa)')
    plt.xlabel('Wheel Speed (m/s)')
    plt.title(f'Pressure and Wheel speed limits for G = {G*1E6} ($\mu$m)')
    plt.text(0.15*U.max(), 0.95/1000*P.max(), 'Pressure Limited', color='white', ha='
        ↪ center', va='center')

    limit_plot(T, Pmin, Pmax, We, U, P/1000)

# Plot the figures
Step = 500 #1000 max
U = np.linspace(0, 30, Step)
G = np.linspace(0, 1E-3, Step)
P = 15000
Pressure_plot(G, U, P)

P = np.linspace(0, 60000, Step)
U = np.linspace(0, 30, Step)
G = 0.5E-3
Gap_plot(G, U, P)

P = np.linspace(0, 60000, Step)
G = np.linspace(0, 1E-3, Step)
U = 15
Speed_plot(G, U, P)
```

B

System and control model Python code

Listing B.1: Control system Python code

```
import time as tm
import random
import numpy as np
import matplotlib.pyplot as plt
from scipy import signal
###
cp = 938
enthalpy = 3.87*10**5
tm = 400 #933
twater = 298
densitywater = 1000
cpwater = 4184
twheel = 298
cpwheel = 385
masswheel = 100
waterflow = 0.0005
density = 2400*0.6 + 0.4*2570
###
thickness_factor = 1
spring_factor = 0.0000001
theta = 2.618
sigma = 0.821
U = 15
K = 2
Rho = 2400 * 0.6 + 0.4 * 2570
gap1 = 0.5E-3

class Plant:
    def __init__(self):
        #self.fluid_flow = 4
        self.pressure = 10000
        self.spring_constant = 1
        self.total_outflow = 0
        self.wheeltemp = 295
        self.thickness = 100E-6
        self.gap = gap1

    def update_state(self, control_signal, disturbance):
        outflow_factor = 0.1 # Decrease in pressure with outflow of fluid
```

```
        # Update equations for the plant behavior
        #self.fluid_flow = control_signal
        self.wheeltemp += tempchange(self.thickness, U, self.wheeltemp)
        #self.gap = gap1*disturbance - 16.5*10**-6*(self.wheeltemp-295)*0.3
        self.gap = gap1 - disturbance - 16.5*10**-6*(self.wheeltemp-295)*0.3

        Pcap = (sigma * (1 - np.cos(theta))) / self.gap


        self.pressure += self.spring_constant * control_signal

        self.thickness = (self.gap / U) * np.sqrt((2 * (self.pressure - Pcap)) / ((1 + K
            ↪ ) * Rho))
        self.total_outflow += self.thickness * thickness_factor
        self.pressure -= outflow_factor * self.total_outflow
        self.spring_constant += spring_factor * self.total_outflow

        #self.fluid_flow = np.sqrt(self.pressure) * abs(disturbance)

    def get_fluid_flow(self):
        return self.fluid_flow

    def get_wheeltemp(self):
        return self.wheeltemp

    def get_thickness(self):
        return self.thickness

    def get_pressure(self):
        return self.pressure

    def get_total_outflow(self):
        return self.total_outflow

    def get_gap(self):
        return self.gap

class PIDController:
    def __init__(self, kp, ki, kd):
        self.kp = kp
        self.ki = ki
        self.kd = kd
        self.last_error = 0
        self.integral = 0

    def control_signal(self, error):
        # PID control algorithm
        self.integral += error
        derivative = error - self.last_error
        output = (self.kp * error) + (self.ki * self.integral) + (self.kd * derivative)
        self.last_error = error
        return output

class actuation:
```

```
    def __init__(self):
        self.previous = 0
        self.signal = 0
    def apply_signal(self, signal):
        # Simulate actuator behavior
        # You can replace this with your own actuator model
        self.signal = (self.previous*100 + signal)/101
        self.previous = self.signal
        #signal = max(-400,signal)
        return self.signal

def tempchange(thickness, speed, twheel):
    width = 0.01
    qin = thickness*width*speed*density*(cp*tm + enthalpy)
    #print(qin, 'qin')
    qout = (twheel - twater)*450#densitywater*cpwater*waterflow
    #print(qout, 'qout')
    dt = (qin-qout)/(cpwheel*masswheel)
    #print(dt, 'dt')
    return dt*1E-3


def add_noise(signal, noise_level):
    # Simulate noise
    noise = random.uniform(-noise_level, noise_level)
    return signal + noise

def generate_disturbance(time, amplitude, frequency):
    # Generate sinusoidal disturbance
    disturbance = (0*1 + 10E-6 * np.sin(2 * np.pi * frequency * time)) - 0*time/(
        ↪ max_iterations*sampling_time)
    return disturbance


def sample_signal(signal, sampling_time):
    # Simulate signal sampling with fewer data points
    #tm.sleep(sampling_time)
    return signal

plt.close('all')
# Control loop parameters
on = 1
kp =6E6*on
ki =1E5*on
kd =5E6*on
noise_level = 10
sampling_time = 1 # Increased sampling time for fewer data points
setpoint = 100E-6
max_iterations = 20000
disturbance_amplitude = 0.02
disturbance_frequency = 0.010

# Initialize components
plant = Plant()
controller = PIDController(kp, ki, kd)
actuation = actuation()
```

```
# Data storage for plotting
time_data = []
fluid_flow_real_data = []
fluid_flow_sampled_data = []
pressure_real_data = []
pressure_sampled_data = []
disturbance_data = []
setpoint_data = []
control_signal_data = []
outflow_data = []
thickness_data = []
gap_sampled_data = []
gap_real_data = []
actuator = []
wheeltemp_data = []
# Control loop
for i in range(max_iterations):
    # Read plant state
    wheeltemp = plant.get_wheeltemp()
    thickness = plant.get_thickness()
    pressure = plant.get_pressure()
    total_outflow = plant.get_total_outflow()
    gap = plant.get_gap()
    # Add noise to the plant state
    #noisy_fluid_flow = add_noise(fluid_flow, noise_level)

    # Calculate control error
    #error = setpoint - noisy_fluid_flow

    # Generate disturbance
    time = i * sampling_time
    disturbance = generate_disturbance(time, disturbance_amplitude,
        ↪ disturbance_frequency)
    if i >= max_iterations/4:
        #disturbance = disturbance*1.2
        disturbance = disturbance - 100E-6
    if i >= max_iterations/2:
        #disturbance = disturbance*0.7
        disturbance = disturbance + 150E-6
    # Sample the plant state with fewer data points
    if i % 64 == 0: # Sample every alternate iteration
        # Apply PID control on the sampled plant state

        # Apply control signal to actuator
        #actuator.apply_signal(control_signal)

        # Update plant state

        # Sample the plant state
        noisy_gap = add_noise(gap, noise_level*1E-6)
        noisy_pressure = add_noise(pressure, noise_level*10)

        Pcap = (sigma * (1 - np.cos(theta))) / noisy_gap
        error = setpoint - (noisy_gap / U) * np.sqrt((2 * (noisy_pressure - Pcap)) / ((1
            ↪  + K) * Rho))
```

```
        control_signal = controller.control_signal(error)
        actuator_input = actuation.apply_signal(control_signal)
        plant.update_state(actuator_input, disturbance)



    else:
        control_signal = control_signal_data[-1] # Reuse the previous control signal
        noisy_gap = None
        noisy_pressure = None
        actuator_input = actuation.apply_signal(control_signal)
        plant.update_state(actuator_input, disturbance)
    # Store data for plotting
    actuator.append(actuator_input)
    time_data.append(i * sampling_time * 1E-3)
    thickness_data.append(thickness)
    pressure_real_data.append(pressure)
    if noisy_pressure is not None:
        pressure_sampled_data.append(noisy_pressure*1E-3)
    else:
        pressure_sampled_data.append(noisy_pressure)
    if noisy_gap is not None:
        gap_sampled_data.append(noisy_gap*1E6)
    else:
        gap_sampled_data.append(noisy_gap)
    gap_real_data.append(gap)
    disturbance_data.append(disturbance)
    setpoint_data.append(setpoint)
    control_signal_data.append(control_signal)
    outflow_data.append(total_outflow)
    wheeltemp_data.append(wheeltemp)

# Plant transfer function
num = [1]
den = [1, 0]
plant_tf = signal.TransferFunction(num, den)

# Control loop transfer function
controller_tf = signal.TransferFunction([kd, kp, ki], [1, 0])
control_loop_tf = signal.convolve(controller_tf.num, plant_tf.num), signal.convolve(
    ↪ controller_tf.den, plant_tf.den)

# Bode plots
w, mag_plant, phase_plant = signal.bode(plant_tf)
w, mag_control_loop, phase_control_loop = signal.bode(control_loop_tf)

# Plotting
plt.figure(1,figsize=(15, 10))

# Plotting the plant behavior
plt.subplot(4, 1, 1)
plt.plot(time_data, np.multiply(thickness_data,1E6), 'b-', label='Ribbon thickness')
plt.plot(time_data, np.multiply(setpoint_data,1E6), label='Setpoint')
#plt.xlabel('Time')
plt.ylabel(r'Ribbon thicknes ($\mu$m)')
```

```
plt.title('System Behavior Uncontrolled - Ribbon thickness - Pressure - Gapsize -
    ↪ Control signal')
plt.legend()
plt.grid(True)

plt.subplot(4, 1, 2)
plt.plot(time_data, np.multiply(pressure_real_data,1E-3), 'b-', label='Real Pressure')
plt.plot(time_data, pressure_sampled_data, 'ro', ms=0.8, label='Sampled Pressure')
#plt.xlabel('Time')
plt.ylabel('Pressure (kPa)')
#plt.title('Plant Behavior - Pressure')
plt.legend()
plt.grid(True)

# Plotting the control loop
plt.subplot(4, 1, 3)
plt.plot(time_data, np.multiply(gap_real_data,1E6), 'b-', label='Gap')
plt.plot(time_data, gap_sampled_data, 'ro', ms=0.8, label='Sampled gap')
#plt.xlabel('Time')
plt.ylabel(r'Gap size ($\mu$m)')
#plt.title('Control Loop')
plt.legend()
plt.grid(True)

# Plotting the control loop
plt.subplot(4, 1, 4)
#plt.plot(time_data, disturbance_data, label='Disturbance')
plt.plot(time_data, control_signal_data, label='Control Signal')
plt.plot(time_data, actuator, label='Actuator input')
#plt.plot(time_data, wheeltemp_data, label='WheelTemp')

plt.xlabel('Time (s)')
plt.ylabel('Pressure change (Pa)')
#plt.title('Control Loop')
plt.legend()
plt.ylim(-200,500)
plt.grid(True)

# plt.subplot(5, 1, 5)
# plt.plot(time_data, outflow_data, label='Total Outflow')
# plt.xlabel('Time (S)')
# plt.ylabel('Total Outflow')
# plt.title('Total Outflow')
# plt.legend()
# plt.grid(True)

# Plotting the Bode plots
plt.figure(figsize=(10, 8))

plt.subplot(2, 1, 1)
plt.semilogx(w, mag_plant)
plt.xlabel('Frequency')
plt.ylabel('Magnitude')
plt.title('Bode Plot - Plant Transfer Function')

plt.subplot(2, 1, 2)
```

```
plt.semilogx(w, mag_control_loop)
plt.xlabel('Frequency')
plt.ylabel('Magnitude')
plt.title('Bode Plot - Control Loop Transfer Function')

plt.tight_layout()
plt.show()
```

C

Material model Python code

Listing C.1: Material model Python code

```
import csv
import numpy as np
import matplotlib.pyplot as plt
from scipy.interpolate import CubicSpline
import os
from PIL import Image
plt.close('all')



def kinetic_k(k_e, V):
    a0 = 0.5e-9
    D = 4.3E-9
    k_V = (k_e + a0 * V/D)/(1 + a0 * V/D)
    return k_V

def kineticPhase(L, S, T0, k_v):
    z = (L - T0) / (S - T0)
    L_k = (T0 * (-z + 1)) / (1 - z * k_v)
    S_k = L_k * k_v
    return L_k, S_k

def read_csv_data(csv_file):
    x_coordinates = []
    y_coordinates = []

    try:
        with open(csv_file, 'r') as csvfile:
            csv_reader = csv.reader(csvfile)

            # Skip the header row if it exists
            next(csv_reader, None)

            for row in csv_reader:
                if len(row) >= 2:
                    x_coordinates.append(float(row[0]))
                    y_coordinates.append(float(row[1]))

        return x_coordinates, y_coordinates
```

```
    except FileNotFoundError:
        print(f"Error: File '{csv_file}' not found.")
        return None, None
    except ValueError:
        print(f"Error: Invalid data in '{csv_file}'. Check if the columns contain
            ↪ numeric values.")
        return None, None

# Replace 'your_folder_path' with the actual path to the folder containing your CSV
    ↪ files
folder_path = r'C:\Users\roald\Documents\TU Delft\Afstuderen\Python\PhaseDiagram'
csv_files = [f for f in os.listdir(folder_path) if f.endswith('.csv')]
Vs = 0.5 # m/s

def process_data(csv_file):
        # Read data from file
        csv_file_path = os.path.join(folder_path, csv_file)
        x_values, y_values = read_csv_data(csv_file_path)

        return x_values, y_values

def common_range(y_values_L, y_values_S, y_values_T0):
    y_common_min = max(min(y_values_L), min(y_values_S), min(y_values_T0))
    y_common_max = min(max(y_values_L), max(y_values_S), max(y_values_T0))
    y_common_range = np.linspace(0, 1400, 1000)#y_common_min, y_common_max, 1000)
    return y_common_range

def interpolate(x_values, y_values, y_common_range):
    if x_values is not None and y_values is not None:
        if x_values[0] < x_values[1] and y_values[0] < y_values[1]:
            print('yes')
            #print(y_values)
            x_values = 100 - np.array(x_values)
            cs = CubicSpline(y_values, x_values)
        else:
            cs = CubicSpline(y_values[::-1], x_values[::-1])
    x_interp_common = cs(y_common_range)
    return x_interp_common


def kinetic_calc(x_interp_1_common, x_interp_2_common, x_interp_3_common):
    # Calculate the k, partition between the curves from the two files for the common
        ↪ range
    partition = x_interp_2_common / x_interp_1_common

    # Calculate kinetic partition
    k_V = kinetic_k(partition, Vs)

    # Calculate kinetic phase
    L_Vs, S_Vs = kineticPhase(x_interp_1_common, x_interp_2_common, x_interp_3_common,
        ↪ k_V)
    return L_Vs, S_Vs, k_V

def kinetic_diagram(L_data, S_data, T0_data):
    x_values_L, y_values_L = process_data(L_data)
    x_values_S, y_values_S = process_data(S_data)
```

```
    x_values_T0, y_values_T0 = process_data(T0_data)

    y_common_range = common_range(y_values_L, y_values_S, y_values_T0)
    x_values_L_interp = interpolate(x_values_L, y_values_L, y_common_range)
    x_values_S_interp = interpolate(x_values_S, y_values_S, y_common_range)
    x_values_T0_interp = interpolate(x_values_T0, y_values_T0, y_common_range)
    L_Vs, S_Vs, k_V = kinetic_calc(x_values_L_interp, x_values_S_interp,
        ↪ x_values_T0_interp)
    return L_Vs, S_Vs, y_common_range, k_V

def intersect(value, function):
    diff = [1E9,0]
    for i in range(0, len(function)):
        diff[1] = abs(value - function[i])
        if diff[1] < diff[0]:
            diff[0] = diff[1]
            index = i
    return index

#Scheill
def scheill(k, C0, end_fraction):
    fS = np.linspace(0,end_fraction,100)
    Cs = k*C0*(1-fS)**(k-1)
    return Cs, fS


def beam_convolution(concentration, beam):
    convolution = np.convolve(concentration, beam, 'valid')
    # convolution = np.zeros(len(concentration))
    # for i in range(0, len(concentration)-1):
    # if i == 0:
    # convolution[i] = (concentration[i] + concentration[i+1])/2

    # elif i > 0 and i < len(concentration):
    # convolution[i] = (concentration[i-1] + concentration[i+1] + concentration[i])/3
    # else:
    # convolution[i] = (concentration[i-1] + concentration[i])/2
    return convolution



L_Vs_Al, S_Vs_Al, y_common_range_Al, k_V_Al = kinetic_diagram(csv_files[0], csv_files
    ↪ [1], csv_files[2])
L_Vs_Si, S_Vs_Si, y_common_range_Si, k_V_Si = kinetic_diagram(csv_files[3], csv_files
    ↪ [4], csv_files[5])
#kinetic eutectic
idx = np.argwhere(np.diff(np.sign(L_Vs_Al-(100 - L_Vs_Si) ))).flatten()
Eu_c = (L_Vs_Si[idx])/100
#partition at start concentration
C0 = 60
partition_index = intersect(C0, L_Vs_Si)

Cs, fS = scheill(k_V_Si[partition_index], 60, Eu_c)
Cl = Cs/k_V_Si[partition_index]

cl_index = intersect(Eu_c*100, Cl)
```

```
Cs, fS = scheill(k_V_Si[partition_index], 60, fS[cl_index][0])
Cl = Cs/k_V_Si[partition_index]

eut = np.linspace(Eu_c[0]*100, Eu_c[0]*100-2, 500)
eut_c = np.linspace(0.26633, 1, 500)
concentration_profile = np.concatenate([Cs, eut])
concentration_fs = np.concatenate([fS, eut_c])
#np.linspace(1/60, 1/60, 60)
beam = np.concatenate([np.linspace(0, 1/30, 30),np.linspace(1/30, 0, 30)])
concentration_profile_beam = np.array(30*[concentration_profile[0]] + list(
    ↪ concentration_profile) + 29*[concentration_profile[-1]])
concentration_beam = beam_convolution(concentration_profile_beam, beam)

x, y = process_data(r'C:\Users\roald\Desktop\SEM Images\230720-Roald-Lingmont\230720-
    ↪ Roald-Lingmont\AlSi(5).csv')
x_err, y_err = process_data(r'C:\Users\roald\Desktop\SEM Images\230720-Roald-Lingmont
    ↪ \230720-Roald-Lingmont\AlSi(5)error.csv')
def interpolate_vector(input_vector, new_length):
    old_length = len(input_vector)
    x_old = np.linspace(0, 1, old_length)
    x_new = np.linspace(0, 1, new_length)
    interpolated_vector = np.interp(x_new, x_old, input_vector)
    return interpolated_vector

y_100 = interpolate_vector(y, 600)







fig, ax1 = plt.subplots()
#ax1.set_xticklabels(['0.0', '0.25', '0.50','0.75', '1.0','0.75', '0.50','0.25','0.0'])
ax1.set_xticks(np.linspace(0,2,9))
ax1.set_xticklabels([0.0, 0.25, 0.50,0.75, 1.0,0.75, 0.50,0.25,0.0,])

#plt.plot(fS, Cs)
#plt.plot(fS, Cl)

ax1.plot(concentration_fs, 100-concentration_profile, label='Calculated Kinetic
    ↪ composition Si%', color='blue')
ax1.plot(concentration_fs, 100-concentration_beam, label='Convoluted Kinetic
    ↪ composition Si%', color='green')
ax1.plot(2-concentration_fs, 100-concentration_profile)
ax1.plot(2-concentration_fs, 100-concentration_beam)
ax1.plot(np.linspace(0,2,25), y, label='Measured composition Si%', color='red')
ax1.set_ylabel('Si%')
ax1.set_xlabel('Solid fraction / distance')
ax1.set_title("Sample composition Si% / Solid fraction Kinetic and Scheill combined +
    ↪ beam convolution fitted")



#ax1.set_xticks([0.0, 0.25, 0.50,0.75, 1.0,0.75, 0.50,0.25,0.0,])
```

```
ax2 = ax1.twiny()
new_xtick_positions = np.linspace(0,2,9)
new_xtick_labels = np.linspace(0,5,9)

ax2.set_xticks(new_xtick_positions)
ax2.set_xticklabels(new_xtick_labels)
ax2.set_xlim(ax1.get_xlim())
ax2.set_xlabel('X-axis (Secondary)')




plt.figure(2,figsize=(10, 6))



for i in range(0,3):
    x_values, y_values = process_data(csv_files[i])
    print(i)
    plt.plot(x_values, y_values, label=f'Standard AlSi phase diagram ', color='blue')
plt.plot(S_Vs_Al, y_common_range_Al, label=f'Kinetic Al Solidus', color='red')
plt.plot(L_Vs_Al, y_common_range_Al, label=f'Kinetic Al Solidus', color='red')




for i in range(3,6):
    x_values, y_values = process_data(csv_files[i])
    print(i)
    plt.plot(x_values, y_values, label=f'Standard AlSi phase diagram', color='orange')
plt.plot(100-S_Vs_Si, y_common_range_Si, label=f'Kinetic Si Solidus', color='green')
plt.plot(100-L_Vs_Si, y_common_range_Si, label=f'Kinetic Al Solidus', color='green')
plt.plot(100-L_Vs_Si[idx], y_common_range_Si[idx],'r*', label=f'Kinetic Eutetic')
plt.plot(100-L_Vs_Si[partition_index], y_common_range_Si[partition_index],'bo', label=f
    ↪ 'Kinetic solidification temperature')
plt.plot(100-S_Vs_Si[partition_index], y_common_range_Si[partition_index],'go', label=f
    ↪ 'Kinetic Si composition')
#plt.plot(L_Vs_Si[idx], y_common_range_Si[idx],'ro')

# plt.plot(x_values_2, y_values_2, label=f'Interpolated ({csv_file})', color='green')
# plt.scatter(x_values_2, y_values_2, label=f'Data Points ({csv_file})', color='orange
    ↪ ')
# plt.plot(x_values_3, y_values_3, label=f'Interpolated ({csv_file})', color='green')
plt.xlabel('Si%')
plt.ylabel('Temperature')
plt.title('Kinetic phase diagram AlSi')
#plt.title(f'Original Data and Cubic Spline Interpolation for {csv_files[0]} and {
    ↪ csv_file}')
plt.legend()
#plt.grid(True)
plt.show()
plt.xlim([-0, 100])
```

```
plt.ylim([-200, 1500])

plt.savefig('demo.png', transparent=True)
"""
if len(csv_files) < 2:
    print("Error: At least two CSV files required to find the difference.")
else:
    # Read data from the first file

    # csv_file_path_1 = os.path.join(folder_path, csv_files[0])
    # x_values_1, y_values_1 = read_csv_data(csv_file_path_1)

    # if x_values_1 is not None and y_values_1 is not None:
    # # Perform cubic spline interpolation for the first file
    # cs_1 = CubicSpline(x_values_1, y_values_1)

    # # Generate finer x values for smoother plot of the first file's interpolation
    # x_finer_1 = np.linspace(min(x_values_1), max(x_values_1), 1000)

    # # Calculate the interpolated y values for the first file
    # y_interp_1 = cs_1(x_finer_1)







    for csv_file in csv_files[0:4]:
        # Read data from the second file
        csv_file_path_2 = os.path.join(folder_path, csv_files[0])
        x_values_2, y_values_2 = read_csv_data(csv_file_path_2)

        csv_file_path_1 = os.path.join(folder_path, csv_files[1])
        x_values_1, y_values_1 = read_csv_data(csv_file_path_1)

        csv_file_path_1 = os.path.join(folder_path, csv_files[2])
        x_values_3, y_values_3 = read_csv_data(csv_file_path_1)

        csv_file_path_1 = os.path.join(folder_path, csv_files[3])
        x_values_4, y_values_4 = read_csv_data(csv_file_path_1)

        csv_file_path_1 = os.path.join(folder_path, csv_files[4])
        x_values_6, y_values_6 = read_csv_data(csv_file_path_1)

        x_values_5, y_values_5 = np.linspace(99.9, 100, 1000), np.linspace(1400, -200,
            ↪ 1000)

        # Liquidus
        if x_values_1 is not None and y_values_1 is not None:
            # Perform cubic spline interpolation for the first file
            cs_1 = CubicSpline(x_values_1, y_values_1)
            cs_1_inv = CubicSpline(y_values_1[::-1], x_values_1[::-1])
            # Generate finer x values for smoother plot of the first file's interpolation
            x_finer_1 = np.linspace(min(x_values_1), max(x_values_1), 1000)
            # Calculate the interpolated y values for the first file
            y_interp_1 = cs_1(x_finer_1)
```

```
# Solidus
if x_values_2 is not None and y_values_2 is not None:
    # Perform cubic spline interpolation for the second file
    cs_2 = CubicSpline(x_values_2, y_values_2)
    cs_2_inv = CubicSpline(y_values_2[::-1], x_values_2[::-1])
    # Generate finer x values for smoother plot of the first file's interpolation
    # x_finer_2 = np.linspace(min(x_values_2), max(x_values_2), 1000)
    # # Calculate the interpolated y values for the first file
    # y_interp_2 = cs_1(x_finer_2)

# T0
if x_values_3 is not None and y_values_3 is not None:
    # Perform cubic spline interpolation for the third file
    cs_3 = CubicSpline(x_values_3, y_values_3)
    cs_3_inv = CubicSpline(y_values_3[::-1], x_values_3[::-1])
    # Generate finer x values for smoother plot of the first file's interpolation
    # x_finer_3 = np.linspace(min(x_values_3), max(x_values_3), 1000)
    # # Calculate the interpolated y values for the first file
    # y_interp_3 = cs_1(x_finer_3)

# Si
if x_values_4 is not None and y_values_4 is not None:
    cs_4 = CubicSpline(x_values_4, y_values_4)
    x_finer_4 = np.linspace(min(x_values_4), max(x_values_4), 1000)
    y_interp_4 = cs_1(x_finer_4)
if x_values_5 is not None and y_values_5 is not None:
    cs_5 = CubicSpline(x_values_5, y_values_5)
if x_values_6 is not None and y_values_6 is not None:
    cs_6 = CubicSpline(x_values_6, y_values_6)

    # Dit moet Y Range zijn
    # Find common x range between the three datasets
    x_common_min = max(min(x_values_1), min(x_values_2), min(x_values_3))
    x_common_max = min(max(x_values_1), max(x_values_2), max(x_values_3))
    x_common_range = np.linspace(x_common_min, x_common_max, 1000)

    y_common_min = max(min(y_values_1), min(y_values_2), min(y_values_3))
    y_common_max = min(max(y_values_1), max(y_values_2), max(y_values_3))
    y_common_range = np.linspace(y_common_min, y_common_max, 1000)

    # Calculate the interpolated y values for the common range
    y_interp_1_common = cs_1(x_common_range)
    y_interp_2_common = cs_2(x_common_range)
    y_interp_3_common = cs_3(x_common_range)

    # Calculate the interpolated y values for the common range
    x_interp_1_common = cs_1_inv(y_common_range)
    x_interp_2_common = cs_2_inv(y_common_range)
    x_interp_3_common = cs_3_inv(y_common_range)


    # Calculate the difference between the curves from the two files for the
        ↪ common range
    y_diff = y_interp_1_common - y_interp_2_common
    x_diff = x_interp_2_common - x_interp_1_common
```

```
        # Calculate the k, partition between the curves from the two files for the
            ↪ common range
        y_partition = y_interp_2_common / y_interp_1_common
        x_partition = x_interp_2_common / x_interp_1_common
        # Calculate kinetic partition
        k_V = kinetic_k(y_partition, 10*0.5)
        k_V_inv = kinetic_k(x_partition, 10*0.5)
        # Calculate kinetic phase
        L_k_Al, S_k_Al = kineticPhase(y_interp_1_common, y_interp_2_common,
            ↪ y_interp_3_common, k_V)
        L_k_Al_inv, S_k_Al_inv = kineticPhase(x_interp_1_common, x_interp_2_common,
            ↪ x_interp_3_common, k_V_inv)


        # Find common x range between the three datasets
        x_common_min2 = max(min(x_values_4), min(x_values_5), min(x_values_6))
        x_common_max2 = min(max(x_values_4), max(x_values_5), max(x_values_6))
        x_common_range2 = np.linspace(x_common_min2, x_common_max2, 1000)

        # Calculate the interpolated y values for the common range
        y_interp_1_common2 = 100-cs_4(x_common_range2)
        y_interp_2_common2 = 100-(x_common_range2)
        y_interp_3_common2 = 100-cs_6(x_common_range2)

        # Calculate the difference between the curves from the two files for the
            ↪ common range
        y_diff2 = y_interp_1_common2 - y_interp_2_common2

        # Calculate the k, partition between the curves from the two files for the
            ↪ common range
        y_partition2 = y_interp_2_common2 / y_interp_1_common2

        # Calculate kinetic partition
        k_V = kinetic_k(y_partition2, 10*0.5)
        # Calculate kinetic phase
        L_k_Si, S_k_Si = kineticPhase(y_interp_1_common2, y_interp_2_common2,
            ↪ y_interp_3_common2, k_V)









        # Plot the original data and interpolation for the first file

plt.figure(figsize=(10, 6))
plt.plot(x_finer_1, y_interp_1, label=f'Interpolated ({csv_files[0]})', color='blue
    ↪ ')
```

```
plt.scatter(x_values_1, y_values_1, label=f'Data Points ({csv_files[0]})', color='
    ↪ red')
plt.plot(x_values_2, y_values_2, label=f'Interpolated ({csv_file})', color='green')
plt.scatter(x_values_2, y_values_2, label=f'Data Points ({csv_file})', color='orange
    ↪ ')
plt.plot(x_values_3, y_values_3, label=f'Interpolated ({csv_file})', color='green')
plt.xlabel('X Coordinate')
plt.ylabel('Y Coordinate')
plt.title(f'Original Data and Cubic Spline Interpolation for {csv_files[0]} and {
    ↪ csv_file}')
#plt.legend()
#plt.grid(True)
plt.show()

# Plot the difference between the curves from the two files for the common range
plt.plot(x_common_range, y_diff, label=f'Difference ({csv_files[0]} - {csv_file})',
    ↪ color='purple')
#plt.plot(x_common_range, y_partition, label=f'Partition ({csv_files[0]} - {csv_file
    ↪ })', color='yellow')
plt.plot(x_common_range, L_k_Al, label=f'Partition ({csv_files[0]} - {csv_file})',
    ↪ color='red')
plt.plot(x_common_range, S_k_Al, label=f'Partition ({csv_files[0]} - {csv_file})',
    ↪ color='red')
plt.plot(L_k_Al_inv, y_common_range, label=f'Partition ({csv_files[0]} - {csv_file})
    ↪ ', color='blue')
plt.plot(S_k_Al_inv, y_common_range, label=f'Partition ({csv_files[0]} - {csv_file})
    ↪ ', color='blue')
plt.xlabel('X Coordinate')
plt.ylabel('Difference (Interpolated Curve)')
plt.title(f'Difference between Cubic Spline Interpolations for {csv_files[0]} and {
    ↪ csv_file}')
#plt.legend()
plt.grid(True)
plt.show()

plt.plot(x_finer_4, y_interp_4, label=f'Interpolated ({csv_files[0]})', color='blue
    ↪ ')
plt.scatter(x_values_4, y_values_4, label=f'Data Points ({csv_files[0]})', color='
    ↪ red')
plt.plot(x_values_5, y_values_5, label=f'Interpolated ({csv_file})', color='green')
plt.scatter(x_values_5, y_values_5, label=f'Data Points ({csv_file})', color='orange
    ↪ ')
plt.plot(x_values_6, y_values_6, label=f'Interpolated ({csv_file})', color='green')
plt.xlabel('X Coordinate')
plt.ylabel('Y Coordinate')
plt.title(f'Original Data and Cubic Spline Interpolation for {csv_files[0]} and {
    ↪ csv_file}')
#plt.legend()
plt.grid(True)
plt.show()

# Plot the difference between the curves from the two files for the common range
plt.plot(x_common_range2, y_diff2, label=f'Difference ({csv_files[0]} - {csv_file})
    ↪ ', color='purple')
#plt.plot(x_common_range, y_partition, label=f'Partition ({csv_files[0]} - {csv_file
    ↪ })', color='yellow')
```

```
    plt.plot(x_common_range2, L_k_Si, label='L_k_Si', color='yellow')
    plt.plot(x_common_range2, S_k_Si, label='L_k_Si', color='yellow')
    plt.xlabel('X Coordinate')
    plt.ylabel('Difference (Interpolated Curve)')
    plt.title(f'Difference between Cubic Spline Interpolations for {csv_files[0]} and {
        ↪ csv_file}')
    plt.legend()
    plt.grid(True)
    plt.show()

    plt.xlim([-0, 100])
    plt.ylim([-200, 1500])
"""
```